Ab initio thermodynamic study of defective strontium titanate

Von der Fakultät Chemie der Universität Stuttgart
zur Erlangung der Würde
eines Doktors der Naturwissenschaften (Dr. rer. nat.)
genehmigte Abhandlung

Vorgelegt von

Evgeny Blokhin

aus Sankt Petersburg, Russland

Hauptberichter: Prof. Dr. J. Maier

Mitberichter: Jun.-Prof. Dr. J. Kästner

Vorsitzender des Prüfungsausschusses: Prof. Dr. E. Mittemeijer

Tag der mündlichen Prüfung: 14.06.2013

Max-Planck-Institut für Festkörperforschung
Universität Stuttgart
2013

This work has no epigraph.

Kurt Gödel

Contents

Formalia

Erklärung

Die vorliegende Doktorarbeit wurde vom Autor selbst in der Abteilung von Prof. Maier am Max-Planck-Institut für Festkörperforschung, im Zeitraum von September 2009 bis März 2013 angefertigt. Der Inhalt ist die eigene Arbeit des Autors, Ausnahmen sind gekennzeichnet, und wurden noch nicht zur Erlangung einer Qualifizierung oder eines Titels an einer akademischen Institution eingereicht.

Stuttgart, den 21 März 2013

Declaration

The work described in this thesis was carried out by the author in the Department of Prof. Maier at the Max Planck Institute for Solid State Research from September 2009 to March 2013. The contents are the original work of the author except where indicated otherwise and have not been previously submitted for any other degree or qualification at any academic institution.

Stuttgart, 21st of March 2013

Acknowledgements

Zusammenfassung

In der vorliegenden Doktorarbeit werden $SrTiO_3$-Kristalle und ihre Oberflächen ohne und mit Punktfehlern auf *ab initio* Ebene untersucht. $SrTiO_3$ mit Perowskitstruktur ist eine ausgezeichnete Modellverbindung für die Untersuchung gemischtleitender Materialien. Da die experimentellen Untersuchungen an komplexen Materialien vergleichsweise aufwendig sind und die Rechnerleistung in den letzten Jahren sehr stark zunahm, hat sich die *ab initio* Modellierung zu einem sehr effizienten Werkzeug in diesem Bereich entwickelt. Zusätzlich gibt es ein signifikantes industrielles Interesse, elektrochemische Anwendungen wie z.B. Festoxidbrennstoffzellen zu verbessern, die zum Teil auf Perowskiten als Funktionsmaterialien beruhen. Ausserdem besteht Bedarf an methodischen Arbeiten zur Fehlstellenthermodynamik dotierter Perowskit-Kristalle und deren Oberflächen.

Sauerstoffleerstellen und Eisendotierung auf Titan-Plätzen sowie deren Assoziate sind charakteristische Defekte in $SrTiO_3$. Das Verständnis der grundlegenden Eigenschaften der Defekte und defektinduzierter Phänomene unter realistischen äußeren Bedingungen (Temperatur, Sauerstoffpartialdruck) erfordert die Berechnungen der thermodynamischen Größen (Entropie und Gibbssche Freie Energie). Daher liegt der Schwerpunkt dieser Studie auf atomaren Schwingungen (Phononen), die notwendig sind, um über die Standard-Null-Kelvin-Näherung hinauszugehen und eine Verbindung zu den thermodynamischen Eigenschaften bei endlichen Temperaturen herzustellen. Das *ab initio* Modellierungsschema wurde so gewählt, dass es gleichzeitig eine genaue Beschreibung der strukturellen, elektronischen und Schwingungseigenschaften des perfekten $SrTiO_3$ liefert. Es wurde eine sehr kleine Aufspaltung der Phononenfrequenzen aufgrund des antiferrodistortiven Phasenübergangs bei 105°K vorhergesagt (2–12 cm^{-1}). Die experimentelle Temperaturabhängigkeit der Wärmekapazität von $SrTiO_3$ wurde korrekt reproduziert. Das verwendete Modellierungsschema wurde dann für die thermodynamische Untersuchung von Sauerstoffleerstellen und Eisendotierung in $SrTiO_3$ bei endlichen Temperaturen angewandt. Die berechneten Phononen-Zustandsdichten und die gruppentheoretische Analyse der defektinduzierten Phononenfrequenzen dienten zur Interpretation gemessener Infrarot- und Raman-Spektren. Mehrere defektinduzierte lokale Phononenmoden konnten identifiziert werden. Es wurde gezeigt, dass die Jahn-Teller-Gitterverzerrungen rund um Eisendotierung und Sauerstoffleerstellen zu Raman- und infrarotaktiven Phononen führen. Insbesondere wurde gezeigt, dass die experimentell beobachtete Raman-Frequenz nahe 700 cm^{-1} durch eine lokalisierte Metall-Sauerstoff-Streckschwingung in der Nähe eines Defekts mit Jahn-Teller-Verzerrung verursacht wird. Die Gibbssche Freie

Bildungsenergie für Sauerstoffleerstellen in Volumen von $SrTiO_3$ wurde berechnet und stimmt unter Berücksichtigung des Phononen-Beitrags gut mit experimentellen Werten überein. Der Phononen-Beitrag steigt oberhalb 1000°K auf mehr als 5% der Leerstellen-Bildungsenergie. Die vorhergesagte relative Stabilität verschiedener Assoziate von Sauerstoffleerstellen und Eisen-Dotieratomen in $SrTiO_3$ entspricht den experimentellen Befunden. Mehrere strukturelle Modelle dieser Komplexe werden durch XANES und EXAFS Daten bestätigt. Bei 0°K treten Effekte durch eine endliche Probengröße erst bei sehr kleinen Abmessungen auf. Ähnlich werden diese Effekte bei erhöhten Temperaturen durch den Phononen-Beitrag geringfügig.

Die Arbeitsschritte, die in dieser Studie entwickelt wurden, sollten für eine breite Klasse von Defekten in nichtmetallischen Feststoffen anwendbar sein. Mehrere zusätzliche Computer-Werkzeuge wurden entwickelt, um solche Untersuchungen zu vereinfachen.

Abstract

In the presented thesis the perfect and defective $SrTiO_3$ bulk crystals and their (001) surfaces are considered on *ab initio* level. Since the experimental study of the complex defective systems is comparatively expensive and difficult, and the computer performance has been greatly increased in the last years, the *ab initio* modeling became very efficient tool to be applied in this field. Additionally, there is a significant industrial demand for the investigation and improvements of the performance of the perovskite-based electrochemical devices, *e.g.* solid oxide fuel cells and permeation membranes. Finally, there is a lack of methodological studies on defect thermodynamics.

The oxygen vacancies and iron impurities, as well as their complexes, are the characteristic defects in $SrTiO_3$ perovskite material. The understanding of basic defect properties and defect-induced phenomena under realistic external conditions requires calculation of thermodynamic properties (the free energy and entropy effects). Thus, thesis is focused on atomic vibrations, *i.e.* phonons, which are necessary to go beyond standard 0°K approximation and to provide a link to the thermodynamic properties at finite temperatures. This is necessary for a realistic treatment of electrochemical devices.

The chosen *ab initio* modeling scheme is found to ensure the most accurate description simultaneously for the structural, electron and phonon properties of the perfect $SrTiO_3$. Namely, the splitting of the phonon frequencies due to the antiferrodistortive phase transition at 105°K is confirmed to be very small (2–12 cm^{-1}). The experimental temperature dependence of the $SrTiO_3$ heat capacity is also successfully reproduced. Further, the modeling scheme is applied for thermodynamic treatment of oxygen vacancies and iron impurities in $SrTiO_3$ at finite temperatures.

The calculated phonon densities of states and group-theoretical study of the defect-induced phonon frequencies are used for the experiment analysis. Several defect-induced local phonon modes are identified, and the experimental Raman- and IR-spectroscopy data are interpreted. The Jahn-Teller-type local lattice distortion around both Fe^{4+} impurity and oxygen vacancy V_O is shown to result in Raman- and IR-active phonons. In particular, the experimentally observed Raman frequency near 700 cm^{-1} is shown to arise for both defects due to a local O ion stretching vibration nearby the Jahn-Teller defect. However, an absence of such a frequency in an experimental phonon spectrum is found to be a manifestation of formation of $Fe^{3+}-V_O$ complexes with oxygen vacancies in the first coordination sphere of iron impurities.

The Gibbs formation energy calculated for the neutral oxygen vacancies in bulk $SrTiO_3$ taking into account the phonon contribution is found to be in excellent agreement with the

experiment. The phonon contribution to the formation energy is shown to increase with temperature, to about 5% above 1000°K. The predicted relative stability of several structural complexes of oxygen vacancy and iron impurity in $SrTiO_3$ is confirmed by known experimental measurements. Several structural models of such $Fe^{3+}-V_O$ complexes in $SrTiO_3$ are discriminated according to the XANES and EXAFS experiments. On an example of SrO-terminated $SrTiO_3$ ultrathin films, the one-dimensional confinement effect on the vacancy formation energy is found to be inconsiderable at 0°K. The phonon contribution to the Gibbs free energy of V_O formation in such ultrathin films at finite temperatures is shown to be minor. This suggests the further account of anharmonic effects is required.

The workflow developed in thesis is proposed for the modeling of wide class of defects in non-metallic solids. Several auxiliary computer tools were designed in order to simplify such possible studies.

List of abbreviations

SOFC: solid oxide fuel cell (Chapter 1)

HF: Hartree-Fock [*theory*] (Chapter 2.1)

DFT: Density Functional Theory (Chapter 2.1)

LCAO: Local Combination of Atomic Orbitals [*approximation*] (Chapter 2.1)

BS: Basis Set(s) (Chapter 2.1)

BZ: Brillouin Zone (Chapter 2.1)

PP: Pseudopotential (Chapter 2.1)

LDA: Local Density Approximation (Chapter 2.1)

GGA: Generalized Gradient Approximation (Chapter 2.1)

HFR: Hartree-Fock-Roothaan [*equations*] (Chapter 2.1)

KS: Kohn-Sham [*theorems*] (Chapter 2.1)

PW: Plane Waves [*basis set*] (Chapter 2.1)

SCF: Self-Consistent Field [*iterative technique*] (Chapter 2.1)

FP: Frozen Phonon [*method*] (Chapter 2.2)

LR: Linear Response [*method*] (Chapter 2.2)

AFD: Antiferrodistortive [*phase*] (Chapter 3.1, 3.3)

FE: Ferroelectric [*phase*] (Chapter 3.1, 3.3)

IR: Infrared [*spectroscopy*] (Chapter 3.1)

TO: Transverse Optical [*phonon mode*] (Chapter 3.2)

LO: Longitudinal Optical [*phonon mode*] (Chapter 3.2)

SPP: Stuttgart Pseudopotential and Basis Set (Chapter 3.2)

PPP: Piskunov Pseudopotential and Basis Set (Chapter 3.2)

DOS: Density of States (Chapter 3.2)

SG: Space Group (Chapter 3.2)

NM: Non-Magnetic [*state*] (Chapter 4.3)

FM: Ferromagnetic [*state*] (Chapter 4.3)

AFM: Antiferromagnetic [*state*] (Chapter 4.3)

XANES: X-ray Adsorption Near Edge Structure [*technique*] (Chapter 4.4)

EXAFS: Extended X-ray Absorption Fine Structure [*technique*] (Chapter 4.4)

2D or 3D: two- or three-dimensional [*unit cell*] (Chapter 5.2)

1. Introduction and objectives

The subject of this thesis lies in a junction of four directions in material science: *perovskite*-type compounds study, *ab initio modeling* of the materials, physical chemistry of *defects*, and *lattice dynamics* (the part of statistical thermodynamics). Only by combining the knowledge in all these directions it is possible to tackle the main problem of this thesis: finite-temperature phenomena in defective ABO_3-type perovskites, used as cathode materials of solid oxide fuel cells (SOFCs).

SOFCs are a class of fuel cells characterized by the use of a solid oxide material as electrolyte. High operating temperatures (600 – 1000°C) are needed to maintain a high ionic conductivity (in addition, the usage of expensive catalyst materials is avoided). A typical scheme of a tubular SOFC is shown in Fig. 1. One of the key challenges is to predict theoretically the cathode performance in order to optimize its composition and reduce the operating temperature.
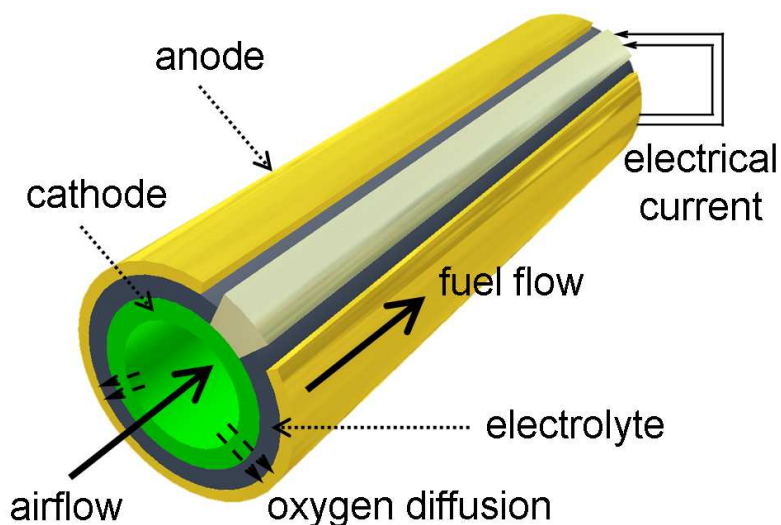
FIG. 1. Typical tubular SOFC (original image is provided by Siemens AG, according to GNU Free Documentation License, http://commons.wikimedia.org/wiki/File:Tubular_sofc_de_edit.png)

At the cathode site an oxygen reduction takes place: $\frac{1}{2}O_2 + 2e + V_O^{\cdot\cdot} \rightarrow O_O^x$ (Kröger-Vink notation [1]). The suitable cathode materials are mixed ionic-electronic conductors of *perovskite* type, *e.g.* $(Ba,Sr)(Co,Fe)O_{3-\delta}$. Among such compounds $SrTiO_3$ is historically considered as an archetype and excellent model material. It is hard to overestimate the number of theoretical concepts in material science, developed in the last fifty years, which are in many aspects based on $SrTiO_3$ research: *e.g.* soft-mode induced phase transitions and anharmonic phenomena, phase transition suppression by means of quantum fluctuations, transport through grain boundaries, quantum

paraelectricity *etc.* (see Chapter 3). In addition to fundamental scientific importance, $SrTiO_3$ has a rich spectrum of technological applications, *e.g.* in high-voltage capacitors [2], gas sensing and photocatalytic devices [3], resistive-switching memory [4] *etc.* The research on $SrTiO_3$ provides a crucial link to the understanding of the properties of more complex related materials with perovskite structure (*e.g.* $La_{0.8}Sr_{0.2}MnO_{3-\delta}$ solid solutions [5]), industrially used as the SOFC cathodes and permeation membranes.

The *ab initio modeling* (Chapter 2) is the most powerful and rigorous approach among predictive methods. In principle, no empirical knowledge about the subject of interest is required to build a valid model. Since the 1990s *ab initio* calculations started to contribute significantly to the understanding of material properties. With the development of new computer simulation methods, the predictive power of theoretical modeling steadily increased and thus a deeper insight into the $SrTiO_3$ properties became possible (Chapter 3). In particular, calculation of the entropy and free energy via phonon contribution is the recent breakthrough that permits calculation of material properties under realistic operational conditions.

Nothing is ideal in the real world; so is the crystalline atomic structure. *Defects* are crucial for electrochemical applications. The most important types of the point defects in $SrTiO_3$ are oxygen vacancies V_O (also called in oxides the color F centers) and substitutional iron impurities, as well as their complexes (Chapter 4). V_O defects (acting as the donors or traps of electrons or holes) are considered to be responsible for the electrical breakdown, current leakage, performance and degradation of the wide range of microelectronic devices [6−9]. On the other hand, oxygen vacancies control the transport properties. Understanding of mobile ionic carrier properties is crucial for SOFCs, oxygen gas sensors, permeation membranes *etc.* [10]. Lastly, iron impurities and Fe−V_O complexes in $SrTiO_3$ play a key role in electrooptical applications [11], reducing current leakage and causing resistance switching [12, 13]. All these types of bulk defects are considered in this thesis. Additionally, attention is paid to surfaces and one-dimensional defect confinement in ultrathin films. The role of confinement on the electron and phonon properties of $SrTiO_3$ ultrathin films (either perfect or containing oxygen vacancies) is of great interest as well [2, 14].

The phonons are the subject of *lattice dynamics*. These quasiparticles represent a quantum mechanical description of lattice vibrational motion and define the fundamental thermodynamic properties of crystals (internal and free energy, entropy, heat capacity). Thus, the predictive power of *ab initio* modeling could be extended beyond 0 K limit and linked to the thermodynamic treatment. The vibrational contribution to the Gibbs free energy is traditionally neglected in the first principles computational studies of point defects and often erroneously assumed to be insignificant.

An accurate account of high temperature effects requires the calculation of phonon spectra for low-symmetry systems, which was extremely time-consuming task, even nowadays. However, the current abilities of the parallel high-performance computing allow performing such calculations. Recent papers [15, 16] serve as a good example, how the phonon calculations and thus account of entropy effects at high temperatures allow one to determine the correct defect charge state and thermodynamic stability.

With all above, it is the general aim of this thesis to focus on phonon properties of both perfect and defective $SrTiO_3$, bulk crystals and surfaces. Concerning these objects, the specific aims are:

(i). To establish a robust *ab initio* computational scheme which is capable to yield the vibrational properties of the materials in a quantitative agreement with infrared, Raman and inelastic neutron scattering experiments: this is done in Chapters 2–3. First, the theoretical background is given for obtaining phonon frequencies and thermodynamic functions from *ab initio* without any empirical knowledge. Second, on example of a defect-free $SrTiO_3$ crystal (which properties are relatively well known) the computational set is chosen and tested. Most of the technical computational details are moved into Appendix.

(ii). To perform a consequent, methodological study of the phase transitions in $SrTiO_3$ from a point of view of lattice dynamics. This is done for a perfect bulk crystal in Chapter 3 and for ultrathin films in Chapter 5, where the concepts of the soft modes and group-theoretical analysis are widely adopted.

(iii). To analyze and interpret the defect-induced behavior, *i.e.* the changes in the structural, electron and vibrational properties of $SrTiO_3$, comparing the results of simulations with available experimental measurements. A full representing of all the main features of simple bulk $SrTiO_3$ with the selected method supports a reliability of the results for the derived systems, the properties of which are less known (Chapters 4–5: defective bulk, perfect surface and defective surface).

(iv). To obtain *ab initio* thermodynamic functions and defect formation energies as a first step for application of macro-scale models in physical chemistry, *e.g.* chemical diffusion, boundary and size effects, ion mobility and conductivity. This is done in Chapters 3–5, describing the results for perfect and defective bulk crystal and surface.

(v). To estimate the efficiency of the known techniques, suitable in the computational scheme compilation and assessment: computational basis set optimization for perfect bulk $SrTiO_3$, soft phonon mode scanning and group-theoretical analysis, phonon spectrum representations and visualizations for defective crystals *etc.* This is covered in Chapters 2.1, 2.2, 3.3, 4.2–4.4 and in Appendix.

(vi). To collect a systematized knowledge base of predicted properties of $SrTiO_3$ and derived perovskite-type materials in relation to existing modeling methods and their implementations. This is done throughout the entire thesis, and the obtained data repository is briefly discussed in Appendix. Such information is of high importance for simulation code testers and the wide user audience, possible further study extensions of any kind, and the development of new cutting-edge material science approaches [17, 18].

2. Theoretical framework

2.1. Computational scheme

This Chapter briefly summarizes the key points of *ab initio* quantum chemical simulation models used within this study. Details of the methods can be found through the references provided in this Chapter (an alternative way is to follow documentation of the computer codes CRYSTAL09 [19] and VASP 5.2 [20], which are adopted in this thesis). Technical information on the computational setup (which is required to reproduce calculation results) is given in the Appendix.

The primary computational tool in the present study is the coupling of Hartree-Fock (HF) and density-functional theory (DFT) approaches within the framework of the linear combination of atomic orbitals (LCAO) basis sets (BS). The core idea of the LCAO method is that the molecular orbitals (*i.e.* the functions of electrons in the many-electron system) can be expanded linearly in terms of atomic orbitals centered on the positions of nuclei [21]. The single-determinant approximation implies a many-electron wavefunction to be represented as an antisymmetrized product of spin-orbitals (*i.e.* Slater determinant). The spin-orbitals are expanded over atomic-like basis functions in order to minimize the averaged ground state energy, leading to the set of so called Hartree-Fock-Roothaan (HFR) equations [22]. Group theory provides the way to exploit symmetry properties of a system through the construction of symmetry-adapted BS, which transform according to the irreducible representations (irreps) of a given symmetry group. Thus, the HFR equations are split into several sets of the equations of the smaller dimensionality, each belonging to the different irreps. Such a factorization permits to reduce the computational cost drastically.

Here periodic boundary conditions are implied. The translational symmetry of a crystal is used to represent the expansion of one-electron eigenfunctions (*i.e.* crystalline orbitals) as a linear combination of Bloch functions [23], depending on the wave vector k in the first Brillouin zone (BZ). In turn, the Bloch functions can be represented in form of analytical Gaussian-type orbitals [24]. The point symmetry of the crystal is used to greatly reduce the number of k vectors, in which calculations are performed, and to make sparser the one-electron Hamiltonian matrix by factorizing each k block into sub-blocks [25]. To sample the BZ, a grid of special points (*i.e.* sampling) is defined to consider a reasonable finite amount of k points [26].

The BS of the free atom has to be modified for crystal LCAO calculations as the diffuse atomic functions cause numerical problems in solids because of the large overlap with the basis functions of the neighboring atoms in a dense-packed crystal [21, 27]. Thus, in the calculations of crystals the diffuse Gaussian exponents are removed or optimized. According to the variational

principle the BS with the optimal exponent should render the lowest value of the total energy per unit cell. For example, detailed BS optimization for the perovskites of $ATiO_3$ type (A=Sr, Ba, Pb) was made in HF and DFT LCAO calculations [28], which allowed reproducing very well the available experimental data (the lattice parameters, the bulk modulus, the optical band gaps). In our calculations we applied the utility code of Ref. [29] which can be used for BS optimization with CRYSTAL09 code. The advantages of the optimized BS over non-optimized BS are illustrated in Chapter 3.

With an increase of the number of electrons on the atoms the computational cost becomes very high. Since the energy levels of core electrons of such atoms are deep and atomic orbitals do not contribute significantly to the chemical bonding, the core electrons can be replaced with effective core pseudopotential (PP). Several such schemes exist, such as Hay-Wadt [30] and Stuttgart-Dresden [31] pseudopotentials. They might have the corresponding predefined BS, in this case such a combination of PP and BS is retained without unpairing.

In practical computations, the Hartree-Fock (HF) and Kohn-Sham (KS, *i.e.* DFT) approaches differ in the way how electron exchange is treated: either as an exact exchange operator (HF theory), or as exchange functional (DFT theory). Additionally, an electron correlation is included in functional form in DFT approach. Note that the kinetic energy contribution, electron-nuclear attraction and electron-electron Coulomb exchange are identical in both approaches. The exact KS exchange-correlation functional can be parametrized with the different forms: *e.g.* local density approximation (LDA) [32] and generalized gradient approximation (GGA) [33]. Unfortunately, there are no plain guidelines given from the KS theorems [34] how to construct it. Furthermore, strictly speaking, the KS eigenvalues and eigenvectors do not reflect the physical meaning of one-electron energies and wavefunctions as in the HF theory. The single-determinant many-electron wavefunction constructed out of the KS orbitals is merely a wavefunction of the fictitious system with non-interacting electrons. Therefore, one should be careful with the KS eigenvalues of the unoccupied states, as the band gap between the uppermost valence and the lowermost conduction bands is strongly underestimated within DFT theory.

Note however that the band gap is always overestimated in HF theory. The two main sources of error are orbital relaxation (changes in orbitals with changing the number of electrons) and electron correlation. An admixing of exact HF exchange to a KS functional is a possible solution of this problem. Combined (hybrid) HF-DFT approximation [21] yields particularly successful results for the electron properties of a wide range of materials. However, the question arises whether such a mixing procedure can still be considered as *ab initio*. Note that nowadays dozens of hybrid

functionals exist [35], obtained mostly in a semi-empirical way by means of fitting to the data sets of measured cohesive energies (such as B3LYP [36] and B3PW [37], applied at the preliminary stage of calculations). Notwithstanding, the strict theoretical rationale was given [38] only for the PBE0 hybrid functional:

$$E_{xc}^{hyb} = E_{xc}^{GGA} + \frac{1}{n}\left(E_x^{HF} - E_x^{GGA}\right) \tag{1}$$

where E_x and E_{xc} are exchange and exchange-correlation energies respectively and parameter $n = 4$ represents the lowest (fourth) order of Møller-Plesset perturbation theory, which provides a realistic description of the shape of E_{xc}. A strict theoretical formulation of PBE0 serves for us as a strong argument in Chapter 3 while choosing the most suitable hybrid functional for the description of more complex systems (where no comparison within a reasonable time limit is possible).

According to the preceding considerations, the main steps of the LCAO-based code may be summarized as follows (Fig. 2a). Once the BS is given, a simple trial expansion of the orbitals can be guessed and then used to find the electron density and the total energy. The effective potential is derived afterwards. As soon as the KS and HFR equations are *ad hoc* solved for this potential, the orbitals are refined (at this step being different from the initial guess). This procedure is reiterated until the desired total energy value is converged and its precision achieves the predefined criteria. Such a scheme is implemented in CRYSTAL09 [19] code, which is used in the present study.

| **(a)** | **(b)** |
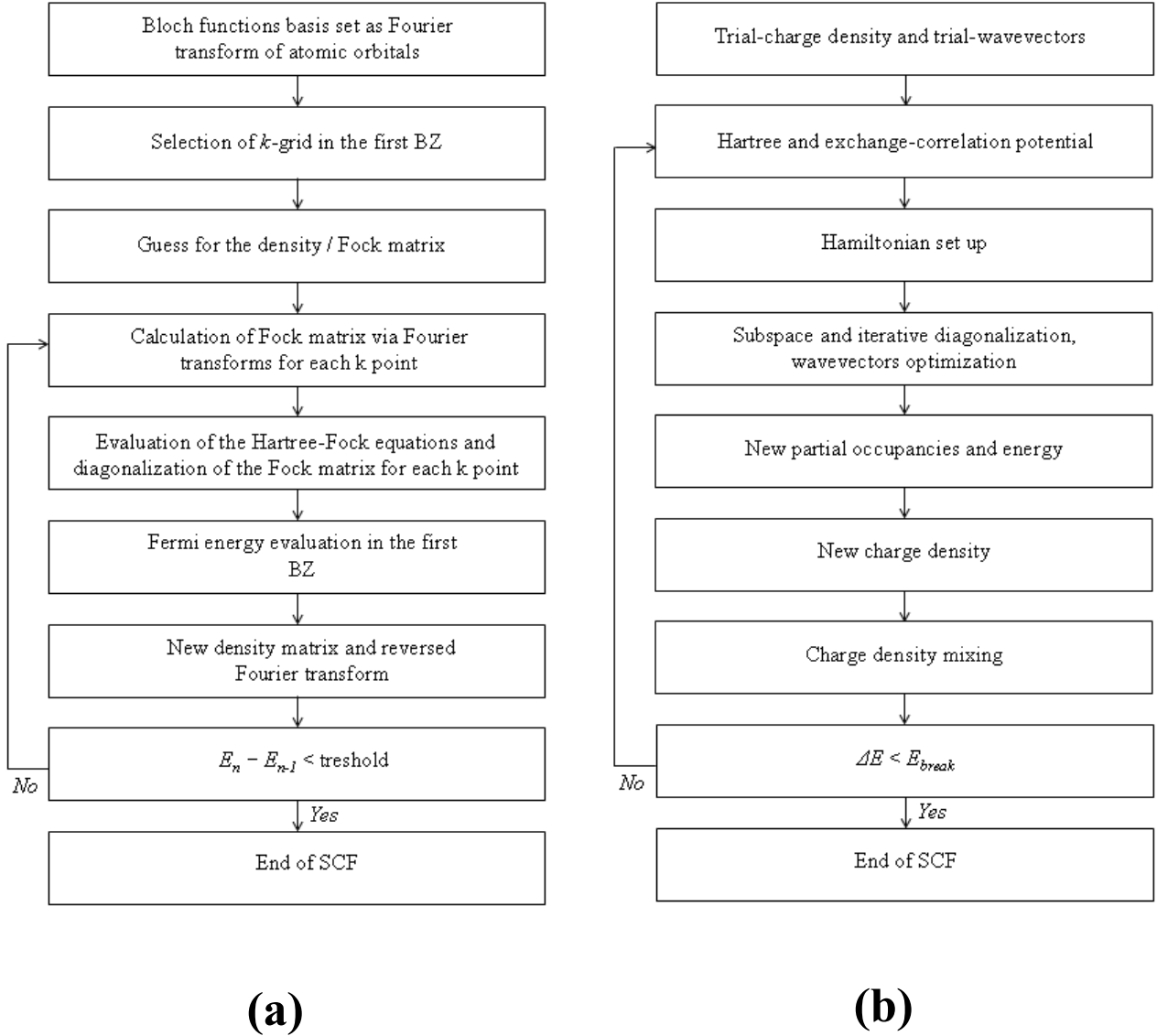
FIG. 2. A schematic workflow of LCAO-based CRYSTAL09 code (a) and PW-based VASP 5.2 code (b)

In addition, plane wave (PW) BSs were applied for a comparison on a preliminary stage of the work. For periodic systems, a spin-orbital is represented as a combination of PWs (an alternative approach to the LCAO expansion). This method has been proved to be efficient in solid state physics since the 1970s due to a number of advantages mainly related to the simplicity of operations with exponents. First, PWs are independent of atomic positions and the atomic forces can be calculated much more easily. Second, the calculation of matrix elements can be performed either in the reciprocal or direct space (efficiently reducing the scaling of the computation with respect to the number of used PWs). Third, the only parameter of the cut-off energy (determining the largest k

vector in PW expansion) is required to manage the quality of the BS. The PW formalism can be enhanced with the projected augmented-wave method [39], which provides the way of exact partitioning the electron wavefunctions. That is, the all-electron solutions are obtained and the fast pseudopotential technique [40] is applied. One of the main disadvantages of PWs is that a huge number of PWs is needed to describe atomic core regions correctly, which leads to the computational difficulties in the small core potentials construction. The use of plane wave BS is preferable for metallic systems, where no considerable electron localization occurs. Additionally, it is challenging to combine HF and PW formalisms within a single code. For example, the hybrid functionals were implemented only recently in VASP PW code [20, 41]. Their performance still is seriously limited at the moment [42], which was a serious argument to avoid their usage for the complex defective systems (see Chapter 3). The workflow of a typical PW code can be illustrated in Fig. 2b. Such a scheme is implemented in VASP code, used in the present study.

As mentioned above, the quantum-mechanical simulation within the discussed models can be carried out for a given nuclei configurations (*e.g.* taken from an experimental crystalline structure determination). Furthermore, one calculates the energy derivatives with respect to the positions of nuclei and lattice constants, in order to inspect the total energy hyper-surface in the space of these parameters. The energy derivatives permit the application of possible optimization algorithms to find the local minimum. Such a procedure is called structure relaxation. Thus, the fully optimized energy serves as approximation of the ground state configuration at zero pressure and temperature conditions. Moreover, simulating the unit cell volume with various constrains leads to the dependence of the total energy per unit cell on the cell volume, permitting the derivation of the elastic properties and the bulk modulus. Note that this represents one of the possible ways to treat finite-temperature properties at *ab initio* level (*e.g.* through the Birch-Murnaghan equation of state). Other ways are *e.g.* via symmetry constrains [43], configurational disorder entropy [44] or vibrational entropy. The primary interest of this thesis refers to the last point, which is discussed in the next Chapter.

Defect treatment is done within a periodic supercell approach, assuming an extended unit cell (or supercell) is defined by a linear transformation, which connects its basic translation vectors with those of the primitive cell. The defect is therefore enclosed in the supercell and periodically repeated in space, representing a particular content within a perfect host. Obviously, the determinant of the linear transformation matrix determines the concentration of single point defect (*e.g.* 2x2x2 = 8 extension of a cubic unit cell stands for 12.5%). It is worth anticipating that the supercell must be chosen sufficiently large for the modeling of the point defect to avoid fictitious interactions between

periodic defect replicas. The quantitative measure of such interaction is the dispersion of the one-electron defect level in a band gap throughout the BZ in the calculated band structure. This dispersion should vanish for the completely isolated defect corresponding to the infinitely large supercell.

2.2. *Ab initio* lattice dynamics

A phonon is a quantum mechanical quasi-particle description of a collective vibrational motion (known as a normal mode in classical mechanics) in which a lattice uniformly oscillates at the same frequency. It is convenient to expand the ground state energy of a crystal into a Taylor series with respect to the infinitesimal atomic displacements δ_i:

$$E = \sum_{n=0}^{\infty} \frac{\partial^{(n)} E(\delta_i)}{n!} (R_i - \delta_i)^n \tag{2}$$

where n is the expansion order and R represents atomic coordinates. In a harmonic approximation, vibrational motions can be described in terms of independent normal modes, each of which is governed by a simple one-dimensional harmonic potential. Within the harmonic approximation only the terms up to quadratic order in (2) are retained, whereas the first-order terms equal zero at the equilibrium. Almost all the calculations in this thesis imply the harmonic approximation (if not explicitly stated otherwise).

In general form, Eq. 2 leads to a set of equations for the lattice motion, the existence of solution of which is given by the condition, that the dynamical matrix (Hessian), scaled by nuclear masses M equals to zero:

$$\det \left| \frac{1}{\sqrt{M_i M_j}} \frac{\partial^2 E(R)}{\partial R_i \partial R_j} - \omega^2 \right| = 0 \tag{3}$$

From Eq. 3 the vibrational frequencies ω are determined as eigenvalues.

The two main techniques for *ab initio* phonon calculations are the linear-response (LR) [45] and the frozen-phonon (FP) [46] methods.

The LR method brings the dynamical matrices formalism into the scope of perturbation theory, stating that the calculation of the Hessian (Eq. 3) requires the calculation of the ground-state electron charge density along with its linear response to the nuclear geometry distortion. Therefore, the main idea is to show that a linear variation in the electron density upon application of a perturbation to the crystal is responsible for a variation in the energy up to third order of the perturbation (so called $2n + 1$ theorem). If the perturbation represents a phonon wave with wave-vector k, calculation of the density change to linear order in the perturbation can be used to determine the dynamical matrix at k. Once an elaborate Fourier interpolation can be used, an arbitrary wave-vector throughout the BZ can be considered, so that only few dynamical matrices need to be computed directly; others will be computed by interpolation. The possibility to decouple

the responses to perturbations of different wavelengths is the great advantage of this scheme. Thus, the workload is essentially independent of the phonon wavelength. The practical disadvantage of this scheme is that it requires a special (quite complicated) implementation and is only supported by few available computer codes.

The FP method assumes an alternative, where a perturbation is frozen in with finite amplitude in a system, which is described by a supercell, having k as a reciprocal lattice vector. The Fourier transforms of the force constants at k are calculated from the finite differences of the forces induced on all the atoms of supercell by perturbation. The FP calculation for lattice vibrations at a generic k vector requires a supercell having k as a reciprocal-lattice vector and whose linear dimensions must be therefore at least of the order of $2\pi / |k|$. In practice, the size of the supercell that one can afford to deal with is limited (see Chapter 2.3 and 4.3).

At higher temperatures, the anharmonic effects have sizeable contributions. This issue is however only indirectly touched in this thesis (Chapter 3.2 and 3.3). The results of the phonon calculations can sometimes result in normal modes with negative eigenvalues. This corresponds to an imaginary frequency value, a normal mode which decreases energy along its displacement vector, and an unstable atomic structure (see Chapter 3). That is, the mode is actually unstable and reveals not just a numerical instability. To explicitly check if a mode is imaginary, one can perform static calculations along a trajectory of the phonon displacement vector. If the mode is physically unstable, then the energy of this displacement should decrease along the trajectory. If the mode is only numerically unstable, then the energy should increase along the trajectory. Scanning of geometry along selected normal modes can be invoked by the special technique in CRYSTAL09 code. Preliminary frequency calculation is required to single out the selected mode. Note that the imaginary values of the frequencies, associated with the structural instabilities, are experimentally revealed as so called soft modes. These modes have a low frequency in the high temperature phases and are essentially *soft* against certain displacements of the atoms. The important influence of the soft modes on the thermodynamic functions is discussed in Chapter 2.4.

2.3. Frozen-phonon method

In this thesis, the FP method was chosen for the phonon calculations as it can be used in conjunction with any external code (only the computation of forces on atoms is required). For our purposes it was crucial to apply LCAO-based CRYSTAL09 code (see Chapter 2.1 and 3.2), which, in addition, has already the FP method routines internally implemented [47]. We give here only a brief survey emphasizing a computational workflow and some points of specific interest; the detailed method description based on the supercell model can be found *e.g.* in [48].

As the first step, the full structure optimization is performed in order to find the equilibrium geometry of the crystal. It is given by the condition that the forces acting on all individual nuclei equal to zero. Then the finite, periodic displacements inducing Hellmann-Feynman forces are created inside a supercell of otherwise perfect crystal. One should notice that not every wave vector k is commensurate with every supercell size, but the general rule is the larger the supercell size, the denser the mapping of the BZ. For a cubic $SrTiO_3$ a supercell consisting of 2x2x2 primitive cells (40 atoms) suffices since it is small enough to be calculated in a reasonable time, but large enough to be commensurate with all the high-symmetry k-vectors of the corresponding BZ (Γ, X, M and R points, see Chapter 3).

Thus, the second step is the construction of the appropriate supercell and displacement of symmetrically non-equivalent atoms. At the moment, two computer codes are known to fully support this procedure: CRYSTAL (version 09) and Phonopy [49]. They were both tested and, mainly due to usage simplicity, the former was adopted. Unlike others, they allow one to reduce the number of independent displacements to a minimum without dependence on the supercell size, taking into account full SG of the supercell including inner translations (see details in [48]). In practice, the weak point of the FP method is the fact that the atomic displacement magnitude is an arbitrary parameter, and the computer codes implementing this method could produce inconsistent results depending on this magnitude. Generally the displacements should not be too large, so as to preserve the linear relation between forces and displacements. They also should not be too small, so as to avoid numerical noise. Usually a good compromise is obtained with a displacement size of the order of 0.003 – 0.01 Å. The default value of the displacement also varies depending on computer codes, for example, 0.003 Å in CRYSTAL09, 0.01 Å in Phonopy and VASP, *etc*.

The third step is the calculation of forces induced by displaced atoms. Obviously this should be done using the same code and method as in the first step, otherwise the criterion of equilibrium would not be fulfilled and excess forces would arise. This is the most time-consuming step, as the

number of displacements needed by symmetry can be huge in the complex low-symmetry defective systems.

Lastly, the fourth step is to calculate symmetrized force constants and solve the dynamical matrix (*i.e.* to symmetrize and diagonalize it). After solving for different k-vectors in the BZ, the eigenvalues (squared phonon frequencies) and eigenvectors (phonon modes) are found. The thermodynamic functions (the free energy and heat capacity) require summations over the phonon eigenvectors in the BZ. At this stage the temperature is finally introduced. One should note the general drawback, that the mean-field calculations by definition neglect anharmonic effects, and this is why the calculated temperature dependencies of the free energy and heat capacity are only qualitatively correct (see Chapters describing results).

The workflow described above can be summarized in Fig.3.
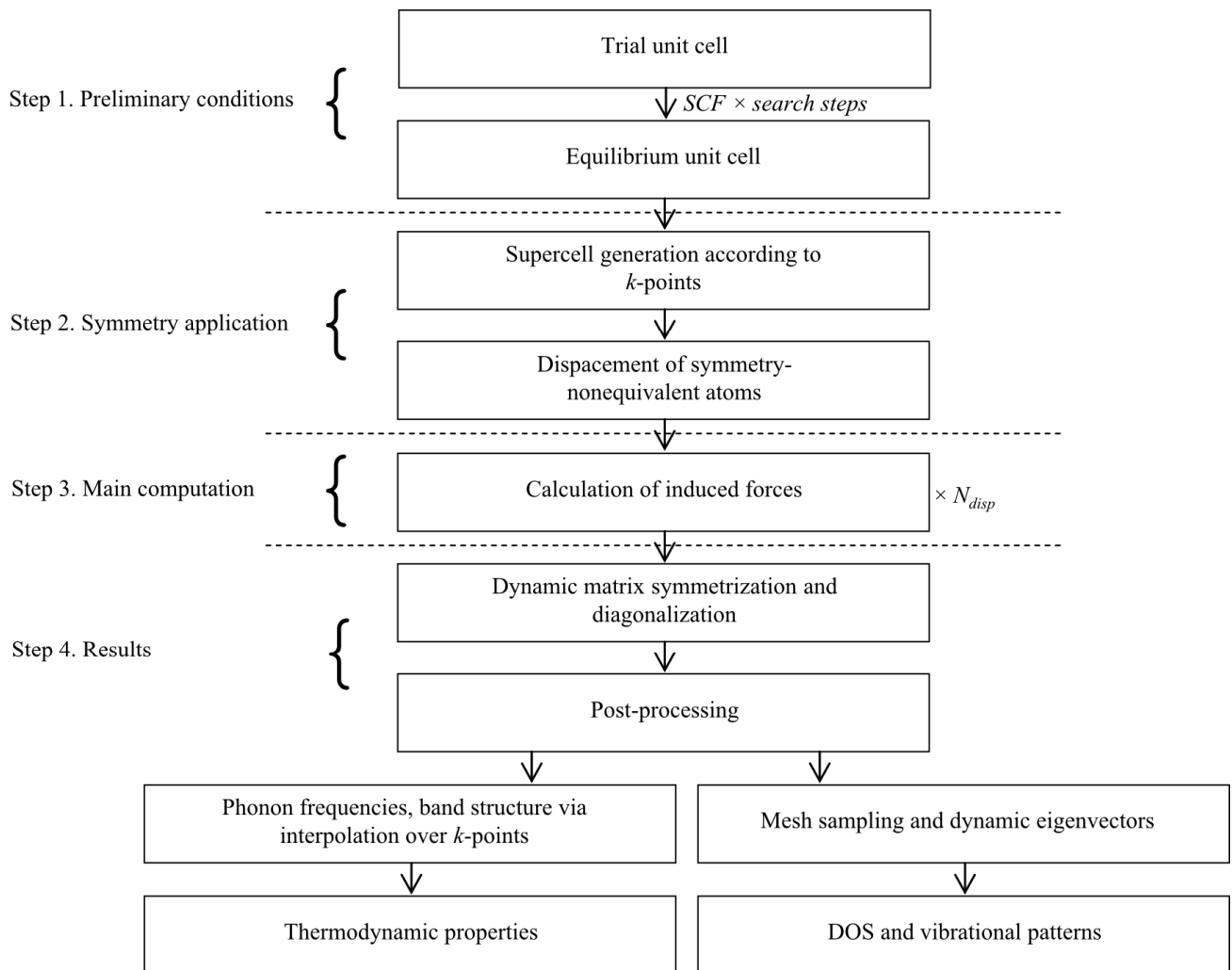
FIG. 3. A workflow of the FP method

One needs to distinguish the FP supercell approach (which is described here) and the defect treatment supercell approach (Chapter 2.1). The purpose of the former is to represent the k-vectors over the BZ within a phonon task, whereas the purpose of the latter is to allow the finite defect content in a perfect host matrix. It should not be confusing to combine these with the aim to investigate non zone-center phonons of the crystal with a certain defect concentration. This is however an extremely tough computational task (the FP supercell over defective supercell expansion) and is omitted within this thesis.

2.4. Thermodynamic models

The principal thermodynamic potentials of interest for this study are the Helmholtz and Gibbs free energies, F and G. The former, derived from the equations of lattice motion, is utilized to compare different crystalline phases (Chapter 3), whereas the latter is utilized in the analysis of chemical reactions to describe the defective systems (Chapters 4 and 5). Note that the equations in this Chapter are defined per primitive crystalline unit cell (or supercell) of $SrTiO_3$.

The free energy for a solid can be usually decomposed into three contributions [50], $E_{st} + F_{vib} + E_{el}$, namely, the static lattice energy E_{st}, the vibrational part F_{vib} due to the lattice dynamics and the term arising from the presence of free electrons E_{el}. Note, that the configurational contribution is omitted in our considerations. As our subject of interest, strontium titanate, is insulator, the E_{el} term can also be ignored. The static lattice energy is identified with the total energy of the compound calculated *ab initio* within adiabatic approximation. The standard expression for F_{vib} is discussed in many reviews (*e.g.*, [51]). In order to obtain the temperature dependence of the Helmholtz free energy F_{vib} and heat capacity C_v, the integration over the phonon density of states is performed according to the equations [51]:

$$F_{vib} = 3nNk_BT \int_0^{\omega_{max}} \ln\left\{2\sinh\frac{\hbar\omega}{2k_BT}\right\}g(\omega)d\omega \tag{4}$$

$$C_v = 3nNk_B \int_0^{\omega_{max}} \left(\frac{\hbar\omega}{2k_BT}\right)^2 \csc h^2\left(\frac{\hbar\omega}{2k_BT}\right)g(\omega)d\omega \tag{5}$$

where n is the number of atoms per unit cell, N is the number of unit cells, ω_L is the maximum phonon frequency, and $g(\omega)\,d\omega$ is defined to be the fractional number of phonon frequencies in the range between ω and $\omega + d\omega$. Note that within the harmonic approximation the heat capacities taken at constant pressure and constant volume are equal ($C_v = C_p = C_{har}$) [52]. In our calculations integration over the whole phonon spectrum is replaced by summation over a finite number of frequencies defined by the size of the supercell used. As one can see, the phonon frequencies enter F_{vib} and C_{har} through hyperbolic functions, meaning the lower the frequency, the greater its contribution. That is why one has to calculate the low frequency (soft) phonon modes as accurate as possible, in order to obtain the reasonable thermodynamic properties. Note that our FP calculations neglect anharmonic effects and this is why the obtained soft mode frequencies and temperature dependencies of the Helmholtz free energy and heat capacity are not fully correct.

For most applications of the *ab initio* calculations, one cares about total electronic energy ($E_{tot.el}$) as a function of the atomic coordinates. This determines most of the properties of interest about a crystal (bond lengths, vibrational frequencies, transition-state barriers, etc.). To evaluate our models of the perfect and defective crystals, the cohesive energy (E_{coh}) and the defect formation energy (E_{form}) can be introduced. The cohesive energy is the difference between atomic and crystalline total energies:

$$E_{coh} = E_{tot.el} \text{ (bulk compound)} - \sum E_{tot.el} \text{ (free atoms)} \tag{6}$$

The cohesive energy represents also an important value for the quality control of the solid-state calculation. Comparing the values obtained experimentally (*e.g.* spectroscopic data of atomic energy levels) and computed *ab initio*, one can estimate, *e.g.* how a certain LCAO BS is suitable for periodical calculations. Such comparison is made in Chapter 3.2. Additionally, various defective models are discriminated basing on E_{coh} in Chapter 4.3.

The defect formation energy serves as crucial quantitative measure for defect-driven chemical processes. The equation for the formation energy of substitution- and vacancy-type defects (namely, iron impurity and oxygen vacancy, see Chapter 4) reads (per supercell):

$$E_{form} = E_{tot.el} \text{ (SrTi}_{1-x}\text{Fe}_x\text{O}_{3-\delta}) - n\, E_{tot.el} \text{ (Fe atom)} + n\, E_{tot.el} \text{ (Ti atom)} + m\, E_{tot.el} \text{ (O atom)} - \\ - N\, E_{tot.el} \text{ (SrTiO}_3) \tag{7}$$

where *n* and *m* are the numbers of considered iron impurities and oxygen vacancies in a supercell, *N* is the number of primitive bulk unit cells in the supercell, *x* is n/N, δ is m/N. The second and third terms in Eq. 7 represent substitution defect, the fourth – vacancy defect. Eq. 7 is defined at 0 K level, which is however very rough approximation for the real processes. One of the possible extensions for real conditions is to use the standard chemical potential, *e.g.* the oxygen molecule chemical potential, $\mu_{O_2}^0(T)$, Eq. 8. To compute it, we used the free energy of a gas-phase O_2 molecule calculated using the LCAO method within an ideal gas model [53].

$$\mu_{O_2}^0(T) = E_{tot}^{O_2} + E_{vib}^{O_2} + E_{rot}^{O_2} + E_{tr}^{O_2} - TS_{vib}^{O_2} - TS_{rot}^{O_2} - TS_{tr}^{O_2} + kT \tag{8}$$

In Eq. 8 the terms marked by "vib", "rot", and "tr" subscripts are the vibrational, rotational and translation components, correspondingly, *E* is the internal energy (its vibration component includes zero-point vibrations), *S* is the entropy, *T* is the temperature and *k* is the Boltzmann's constant. All these terms were calculated using the CRYSTAL09 code (see Chapter 4 and Appendix). Note, that the accuracy of calculated properties of O_2 for the defect formation energies is often overlooked in the literature. As known, the binding energy of O_2 usually is significantly overestimated using the

standard DFT functional [54, 55] which produces errors in the V_O formation energy of the order of 0.7 eV per oxygen atom. In contrast, the LCAO method and the hybrid PBE0 functional used here allow us to reproduce very accurately the vibrational properties of O_2 as well as the equilibrium bond length and the binding energy. As seen from Appendix, the properties of O_2 as calculated in the present study are in good agreement with the experimental findings and previous HSE LCAO calculations. Such high accuracy LCAO calculations allow us to avoid any experimental data for defect formation energies. Therefore, the sole inclusion of chemical potential of the defect species in an equation of type of Eq. 7 permits finite-temperature analysis (in Chapter 4.3 we call this "without-phonon" contribution assuming the phonons of the host crystal are still not included). Extending the model with the phonons of perfect and defective medium, the standard Gibbs free energy of oxygen vacancy formation, ΔG_F^0, as a function of temperature at constant pressure (oxygen-rich conditions) reads:

$$\Delta G_F^0 (T) = \left[E_{tot}^{V_O} + \frac{1}{n} \left(E_{vib}^{V_O}(T) - TS_{vib}^{V_O}(T) \right) + pV^{V_O} \right] - \left[E_{tot}^{p} + \frac{1}{m} \left(E_{vib}^{p}(T) - TS_{vib}^{p}(T) \right) + pV^{p} \right] + \frac{1}{2} \mu_{O_2}^0 (T) \quad (9)$$

where superscripts p, V_O indicate perfect and defective (one V_O per supercell) crystals, E_{tot} – total electron energies, V – the supercell volume, p – the standard pressure. All the energies are given per supercell. The prefactors $1/n$ and $1/m$ in Eq. 9 are the ratios of the number of atoms in a primitive unit cell to that in the supercell for the defective (one V_O per supercell) and perfect $SrTiO_3$, respectively.

Note, that the ratios $1/n$ and $1/m$ mean the phonon contribution is scaled on a primitive cubic bulk unit cell. Such a scaling is concerned, first, with a suppressing of anharmonic errors (see Chapter 2.2), second, with the problem of supercell convergence (finite-size effects) in a phonon task. Generally, the scaled and non-scaled cases must coincide for an idealized harmonic case at the infinite supercell size, where no interactions of phonons with their replicas in the neighboring cells are present.

3. Perfect SrTiO₃ bulk

3.1. Literature overview

SrTiO₃ crystal can be metaphorically called a guinea pig of material science, *i.e.* a very common subject of scientific experimentation. There are several reasons of that, *e.g.* coexistence of covalent and ionic bonding types, mixed electronic-ionic conductivity of doped material, very large dielectric constant at room temperature, *etc.*

The scientific interest in SrTiO₃ could be formally subdivided into two periods. The first wave of interest started in the 1960s when antiferrodistortive (AFD) phase transition near 105 K attracted great attention [56]. It was shown that the soft phonon mode at the *R*-point of the BZ of a cubic structure associated with a TiO₆-octahedral antiphase rotation along the *c* axis is condensed below 105 K resulting in a tetragonal lattice distortion with a slight unit cell stretching (*c/a* > 1) [57]. It should be noted that such lattice instabilities of cubic SrTiO₃ in zero Kelvin calculations have to result in the appearance of imaginary phonon frequencies (see below). The second surge of interest emerged in the 1990s when a quantum-stabilized paraelectric regime near 0 K was discovered and an incipient ferroelectric behavior below 37 K was suggested [58]. An incipient character means that SrTiO₃ has a very large static dielectric response and is only barely stabilized against the condensation of the *Γ*-point FE soft mode, probably by means of quantum fluctuations [59]. This hypothesis was discussed in details in Refs. [60, 61]. Despite SrTiO₃ reveals anomalous dielectric properties at low temperatures, it still remains paraelectric down to 0°K, due to the both above-mentioned AFD phase transition and quantum effects [62]. By this reason SrTiO₃ is called also a quantum paraelectric.

Since the 1990s *ab initio* calculations started to contribute significantly to the understanding of SrTiO₃ properties, including phonons ([59, 64] and references therein). The two main adopted techniques for *ab initio* phonon calculations are the FP and LR methods (see Chapter 2.2). Both are independent on any experimental data and fitting parameters. The literature analysis of the applications of these methods to a cubic SrTiO₃ reveals rather inconsistent results concerning the presence of the soft modes at the different BZ points (and, if present, whether the corresponding frequencies are real or imaginary). First, the calculations by Sai and Vanderbilt [59] based on the DFT-LDA approximation combined with plane waves (PW) within the FP method have shown the concurrent character of AFD and ferroelectric instabilities, *i.e.* hardening of the AFD *R*-phonon and softening of the ferroelectric *Γ*-phonon with the volume increase with respect to theoretical equilibrium. Second, the series of the LDA, GGA-PBE and hybrid HSE06 exchange-correlation

calculations performed by Wahl and Vogtenhuber [63] via the PW formalism within the FP method revealed the soft mode at the Γ-point as real for LDA and imaginary for the GGA-PBE and hybrid HSE06 methods. Third, the linear augmented PW-LDA calculations within the LR method performed by LaSota [64] and Lebedev [65] detected imaginary soft modes at the M-, R- and Γ-points of the BZ. More details on the lattice dynamics of the cubic SrTiO$_3$ can be found in [66−69]. Concerning the low-temperature AFD phase, there is only one PW-LDA study [59] dealing with phonons. However, the AFD phase geometry obtained in this study is quite far from experimental one. In fact, there is the only hybrid B3PW study [70] within the linear combination of atomic orbitals (LCAO) formalism where the correct geometry of the AFD phase and its energetic preference with respect to the cubic phase was predicted. It was shown therein that the doubling of the unit cell, despite the tiny tetragonal distortion, changes the indirect band gap to a direct one, which is well observed in photoconductivity studies.

Such a contradictory situation with respect to the phonons of the cubic phase and the lack of the studies of phonons of the tetragonal phase is certainly discomforting. This is why it is necessary to apply more accurate LCAO-based hybrid DFT calculations to this problem (to the best of our knowledge, there have been no such attempts so far) [107]. Furthermore, a thermodynamic comparison of different SrTiO$_3$ phases has also never been considered. Thus, Chapter 3 is aimed to consider these deficiencies. The accurate representation of known physical properties of SrTiO$_3$ via phonon calculations is necessary before the acquired techniques can be applied to more complex systems. It is important to note that all SrTiO$_3$ structural transformation effects mentioned above are very tiny and this is why their reproduction could be considered as a sensitive test for the new simulation techniques. Understanding the relation between observed AFD phase transition and phonon symmetry (*e.g.* which modes are expected to soften) needs a careful group theoretical analysis, which is performed in this thesis. Such an analysis is also important for the classification of calculated phonon frequencies (Raman, infrared (IR) or silent) and comparison with experimental frequencies (*e.g.* neutron scattering measurements suggest phonon symmetry).

3.2. Cubic phase

The $SrTiO_3$ cubic phase (space group (SG) $Pm\overline{3}m$ O_h^1) represents an example of the perfect perovskite-type cubic ABO_3 structure. We set the octahedrally coordinated B cation at the Wyckoff position 1a (0, 0, 0), the A cation at 1b (1/2, 1/2, 1/2), and the anion at 3d (1/2, 0, 0) (Table 5 and Fig. 6a). To analyze the symmetry of phonon states, the method of induced representations (hereafter reps) of SGs can be used [71, 72]. The total dimension n of the induced rep (called the mechanical rep) equals $3N$ (N is the number of atoms in the primitive cell and equals 5 for perfect perovskite) [107].

The knowledge of soft phonon mode symmetry of the initial structure allows the prediction of the possible symmetry of the derivative structure (*e.g.,* using Stokes and Hatch tables [73]). In particular, the soft phonon at the *R*-point of the BZ of a cubic (*Pm-3m*) structure in the case of $SrTiO_3$ induces the tetragonal AFD (*I4/mcm*) structure (this was proved by experiments, see Chapter 3.1), whereas the soft phonon at the *Γ*-point could induce the tetragonal FE (*P4mm*) structure [106].

We focus here on phonon properties of cubic and tetragonal AFD $SrTiO_3$. However, since the phonons are computed for the equilibrium structures (Chapter 2.3), the structural and electronic properties are obtained at this stage per addendum and considered for important preliminary comparison.

In the beginning of our work, there were several computational schemes suitable for $SrTiO_3$. They were, *firstly*, LCAO and PW formalisms, *secondly*, two PPs (with corresponding BS) for LCAO from the works [74, 75] (hereafter called SPP) and from the work [28] (hereafter called PPP), *thirdly*, three hybrid HF-DFT functionals (B3PW, B3LYP and PBE0, see Chapter 2.1). Therefore, nearly dozen combinations (depending on availability of the scheme in a particular simulation code) were considered. Additionally, we illustrate here the importance of BS optimization (Chapter 2.1) and mentioned the results for pure DFT-GGA PBE functional (used in conjunction with SPP). We choose the computational scheme, better representing the structural, electron and phonon properties simultaneously in comparison with experimental data [68, 77−88].

TABLE 1. Comparison of different combinations of hybrid functional and PP

Comp. set	$a_{cub.}$, Å	Dir. band gap (cub.), eV	Γ soft mode, cm^{-1}	R soft mode, cm^{-1}
PBE0 + SPP	3.91	4.2	72	70
PBE0 + PPP	3.90	4.5	*77i*	51
B3PW + SPP	3.92	3.7	17	55
B3PW + PPP	3.91	4.0	*93i*	*35i*
B3LYP + SPP	3.95	3.8	*104i*	*28i*
B3LYP + PPP	3.94	3.9	*153i*	*72i*
Expt.	3.91 (298*K*)	3.8	42 [82], 91 [83] (298*K*)	52 [83] (298*K*)

Table 1 contains the results for six combinations of hybrid functional and PP. One should note that the hybrid functionals give very good results for most of the properties, with no considerable dependence on a particular PP. A similar comparison is made for the tetragonal AFD phase (see Chapter 3.3). Almost all the combinations reproduce the total energy gain of the tetragonal AFD and hypothetical FE phases (see Chapter 3.3) with respect to the cubic phase (though the energy difference is extremely small, in the range of meV).

Whereas the lattice constant and the band gap of cubic crystal are pretty well reproduced, a deviation arises in phonon properties, namely, in soft modes, which are the most delicate part. Obviously, the imaginary values should not be included in a summation during the evaluation of thermodynamic properties and thus lead to non-acceptable results in the Helmholtz free energy and heat capacity (Chapter 3.4). Therefore, only the results for two combinations (PBE0 + SPP and B3PW + SPP) pass the initial selection and are adopted for further comparison. We found their results to be fairly close (Tables 1, 2). Further, in addition, we keep mentioning the results of B3PW + PPP set as a consistent example of imaginary values for soft modes even in other low-symmetry phases.

In Table 2 the more detailed results on bulk SrTiO$_3$ for the PBE0+ SPP, B3PW+ SPP (LCAO formalism) and HSE06 [63] (PW formalism, the range-separated variant [76] of the PBE0) are summarized. As can be seen, a very good agreement with experiment is kept (though the rotational angle of the AFD phase is slightly off), confirming the fact that hybrid DFT functionals treat crystalline bulk properties accurately [28, 70]. Interestingly, the smaller the calculated band gap of the cubic phase, the larger the calculated octahedral rotational angle of the tetragonal AFD phase

(see Chapter 3.3, this effect was also noted in [70]). As one can see, the pure DFT-GGA PBE functional in both the LCAO and PW calculations considerably underestimates the band gap and overestimates the lattice constant. In general, this is well-known [28, 70] trend in GGA calculations (it was shortly discussed in Chapter 2.3).

TABLE 2. Cubic $SrTiO_3$ basic properties [107]

	L C A O (SPP)					P W		Expt.
	PBE	PBE0			B3PW	PBE	PBE0	
		non-opt. BS	opt. BS	opt. BS + Sr_d				
Lattice constant a_0, Å	3.96	3.89	3.91	3.90	3.92	3.94	3.90	3.91 [77]
Direct (and indirect) band gap, eV	2.1 (1.8)	4.3 (4.0)	4.2 (3.9)	4.2 (3.8)	3.7 (3.4)	2.1 (1.8)	4.4 (4.0)	3.8 (3.3) [78]
Cohesive energy, eV	31.6	28.5	29.3	30.0	29.1	32.8	32.2	31.7 [79]
Bulk modulus, GPa	171	220	195	201	190	169	193	179 [80]

The importance of the proper choice of BS is confirmed by a comparison of the LCAO results for the PBE0 functional with optimized and non-optimized BS (all the other combinations were reported in an optimized form; see Table A1 in Appendix). The optimization improves the agreement with the experiment not only for the band gap (electron properties), but also for crystal cohesive energy and bulk modulus (thermochemical and mechanical properties). On the other hand, the results of PBE0 PW calculations are also close to the experimental data. However, PW VASP calculations with the hybrid functionals are much more time consuming than similar CRYSTAL09 calculations [107].

The calculated transverse optical (TO) and longitudinal optical (LO) phonon frequencies for the cubic phase at the Γ and R points of the BZ are summarized in Tables 3 and 4. To calculate phonons in R point, the primitive unit cell should be doubled with the transformation

matrix $\begin{pmatrix} 110 \\ 101 \\ 011 \end{pmatrix}$ of the lattice translation vectors [21]. The upper and lower parts of the Table 3 present

results for the Γ and R-point calculations, respectively. One obtains four t_{1u} modes and one t_{2u} mode at the Γ point of the BZ (one t_{1u} mode is acoustic). Three phonon modes of the t_{1u} symmetry are IR active and one mode of the t_{2u} symmetry is neither IR nor Raman active (silent mode). The latter mode is connected with the displacements of O atoms only. Three modes 1^+, 3^+ and 4^+ at the R-point of the BZ (with the degeneracy 1, 2 and 3, respectively) are displacement modes of O atom only. The 3-fold degenerated R_{4-} and R_{5+} modes are Ti and Sr-O modes, respectively.

All the methods used predict the t_{1u} TO1 mode to be soft, in agreement with experiments [56, 81]. Its frequency is either imaginary or very low, depending on the particular functional. Moreover, in all the PW calculations it is imaginary. (It is important to recall that our calculations are performed in the harmonic approximation and thus unable to obtain correctly the soft mode frequencies.)

TABLE 3. TO phonon frequencies (cm^{-1}) in cubic SrTiO$_3$ phase [107]

		LCAO (SPP)				P W this work		P W [63]		Expt. (298K) [82][a], [83][b], [84][b]
		PBE	PBE0 non-opt.	PBE0 opt.	B3PW	PBE	PBE0	PBE	HSE06	
Γ	t_{1u} (TO1)	71i	63	72	17	133i	100i	115i	74i	42 [82], 91 [83]
	t_{1u} (TO2)	166	203	180	175	146	161	147	162	175 [82], 170 [83]
	t_{2u}	247	302	271	267	226	252	234	250	265 [83]
	t_{1u} (TO3)	522	594	547	540	508	536	512	533	545 [82], 547 [83]
R	R_{4+}	16i	92	70	55	86i	54i	~90i	~80i	52 [83]
	R_{5+}	144	177	153	149	128	138	[63]	[63]	145 [83]
	R_{4-}	432	481	460	454	413	442			446 [83]
	R_{5+}	437	493	465	461	419	449			450 [83]
	R_{3+}	440	533	478	466	433	475			474 [83]
	R_{1+}	804	906	861	848	798	857			~800 [84]

[a] IR measurements

[b] inelastic neutron scattering measurements

In agreement with the group-theoretical analysis (Chapter 3.3, Table 5) and inelastic neutron scattering experiments [83], we observe instability for the calculated R_{4+} soft mode. The BS optimization in the LCAO approach greatly improves the results and reduces the relative errors by a factor of 2–5 with respect to the experimental data [83] (as compared with the non-optimized BS). The PW calculations with the PBE0 functional also suggest high quality results. Our results for the PW PBE0 calculations are very similar to those recently published for the HSE06 hybrid functional with screened Coulomb interactions [63].

Depending on the inclusion of the *d*-polarization orbital on Sr ion in our optimized LCAO BS, soft-mode frequency is either (relatively small) real or imaginary. Thus, this property is very sensitive to the choice of the LCAO BS [107].

TABLE 4. LO phonon frequencies (cm^{-1}) in cubic SrTiO$_3$ phase [107]

		LCAO			PW	Expt.
	PBE	PBE0		B3PW	LDA [59]	[82]
		non-opt. BS	opt. BS			
t_{1u} (LO1)	165	203	180	174	158	171
t_{1u} (LO2)	458	530	480	477	454	474
t_{1u} (LO3)	833	810	809	809	829	795

The BS optimization in the LCAO approach greatly improves the results, in general, and reduces the relative errors for calculated frequencies by a factor of 2–5 with respect to the experimental data [49] (as compared with the nonoptimized BS). The PW calculations with the PBE0 functional also suggest high-quality results. Our results for the PW PBE0 calculations are very similar to those recently published for the HSE hybrid functional with screened Coulomb interactions [14]. The results for high-frequency calculations are less sensitive to the use of the particular functional than those for low frequencies.

There is a general trend for the hybrid functionals within the LCAO approach, that the calculated phonon frequencies at the Γ and R points are slightly overestimated as compared with the experimental values (~10 cm^{-1} on the average, except for the T01 soft mode). Contrary, the PW approach with PBE0 functional slightly underestimates (~7 cm^{-1}) phonon frequencies. Again, the GGA functional within both the LCAO and PW approaches underestimates frequencies (by ~25 cm^{-1}, see [107]).

The agreement with the experiment for three LO frequencies (Table 4) is also very good, as well as magnitude of the LO-TO splitting. The earlier PW calculations within the standard LDA approximation [59] gave worse results than our hybrid-functional calculations.
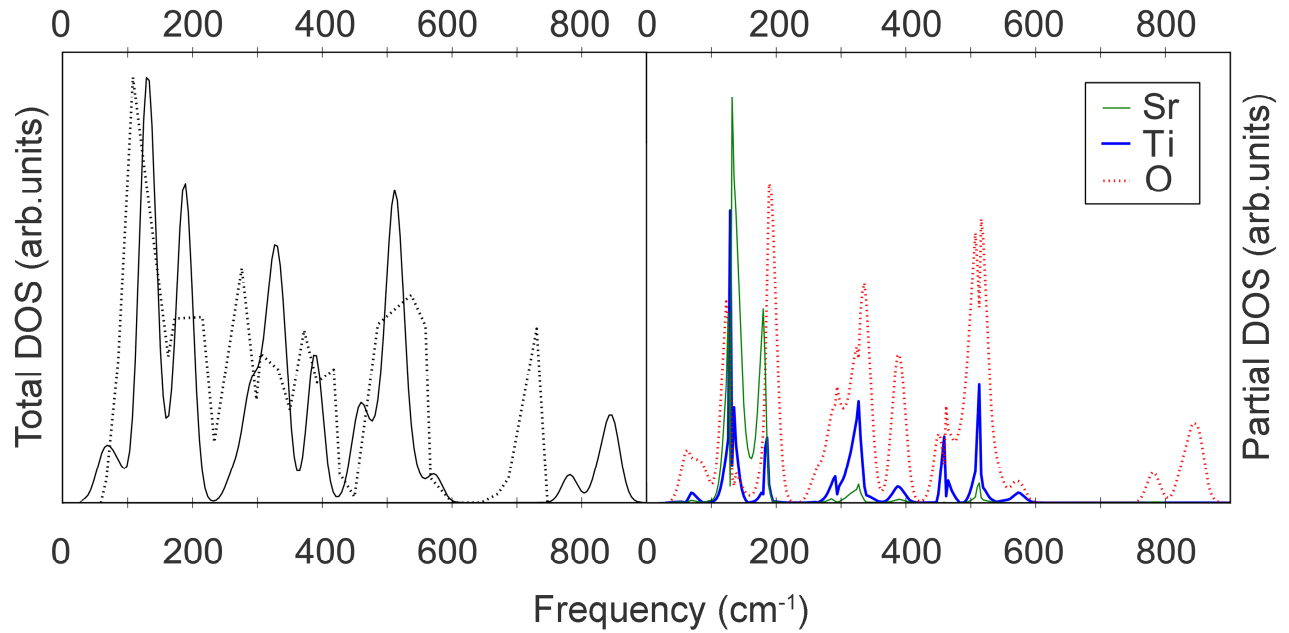
FIG. 4. The calculated total (left) and atom-projected (right) phonon DOS for perfect cubic $SrTiO_3$ [107] [the dotted line at the left is an experimentally extracted total DOS (Ref. 83)]

The phonon frequencies were smeared out according to a normal distribution [107], in order to obtain the total and atom-projected phonon density of states (DOS) for a perfect crystal (Fig. 4). It is generally in a good agreement with the experimentally extracted data [83]. The discrepancy occurs only at the peak ~700 cm^{-1}, however we tend not to fully trust the DOS data [83], as it was estimated using fitting procedures.

The dependence of the soft mode frequencies at the Γ and R points are plotted in Fig. 5 as a function of the lattice constant (which mimics thermal expansion of the lattice). This is the first step beyond the harmonic approximation (quasi-harmonic approach), when the harmonic frequencies are renormalised by a some change in the crystal volume. As one can see, the soft mode at the R point increases very slowly, whereas that at the Γ point decreases considerably, supporting the idea [59] about their concurrent character. The recent similar simulations using the ABINIT code with the GGA-PW91 functional [68] and HSE hybrid functional [63] have shown the same trend, but with an imaginary frequency at the R point at all the lattice parameters considered.

Following the theoretical considerations (Chapter 2.1), taking into account the novelty of SPP, average time requirements for LCAO / PW calculation and usage simplicity, we made a decision to adopt PBE0 + SPP set (LCAO framework) for all the further calculations.
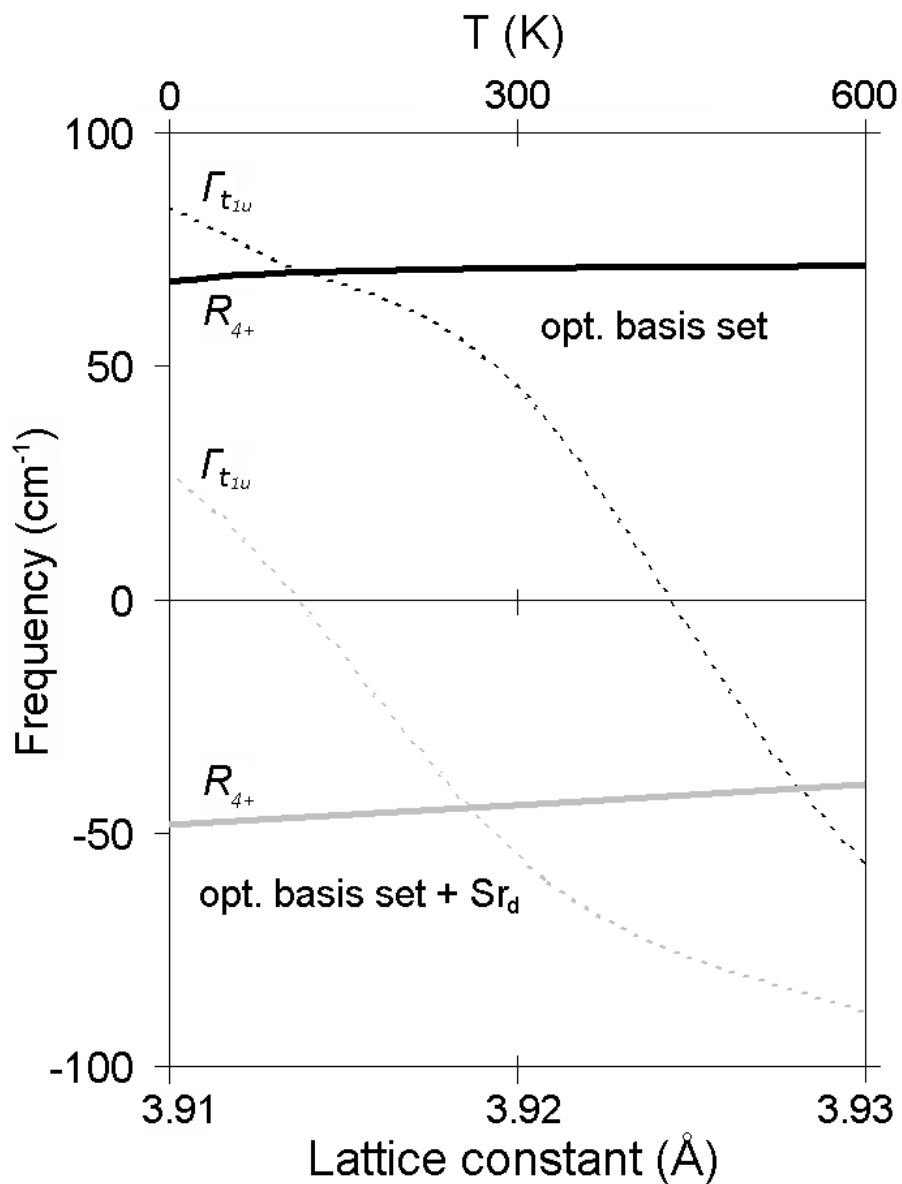
FIG. 5. Γ and R soft phonon modes vs. lattice constant (*i.e.* thermal expansion) calculated via PBE0 (upper and lower parts correspond to the LCAO BS with and without the Sr d-polarization orbital). Imaginary frequencies are represented by negative values [107].

3.3. Tetragonal phase

The second-order structural phase transition at 105°K reduces the symmetry of $SrTiO_3$ from a cubic (O_h^1) to tetragonal (SG $I4/mcm$-D_{4h}^{18}). The primitive unit cell of the body-centered tetragonal lattice consists now of 10 atoms (the cubic unit cell is doubled). Fig. 6b shows the crystallographic (quadruple) unit cell of body-centered tetragonal lattice and the occupations of Wyckoff positions by atoms.

SG 221: Pm3m, $T_{exp.}>105K$

$a_0 = 3.905$ Å

SG 140: I4/mcm, $T_{exp.}<105K$

$\sqrt{2}a_0 \approx a = 5.507$ Å, $2a_0 \approx c = 7.796$ Å

oxygen distortion in 8h, u=0.241

vertical cell stretching, $c/(\sqrt{2}a)$=1.001

Sr 0.5 0.5 0.5 (1b)

Ti 0.0 0.0 0.0 (1a)

O 0.5 0.0 0.0 (3d)

(a)

Sr 0.00 0.50 0.25 (4b)

Ti 0.00 0.00 0.00 (4c)

O 0.00 0.00 0.25 (4a)

O u u+0.50 0.00 (8h)

(b)
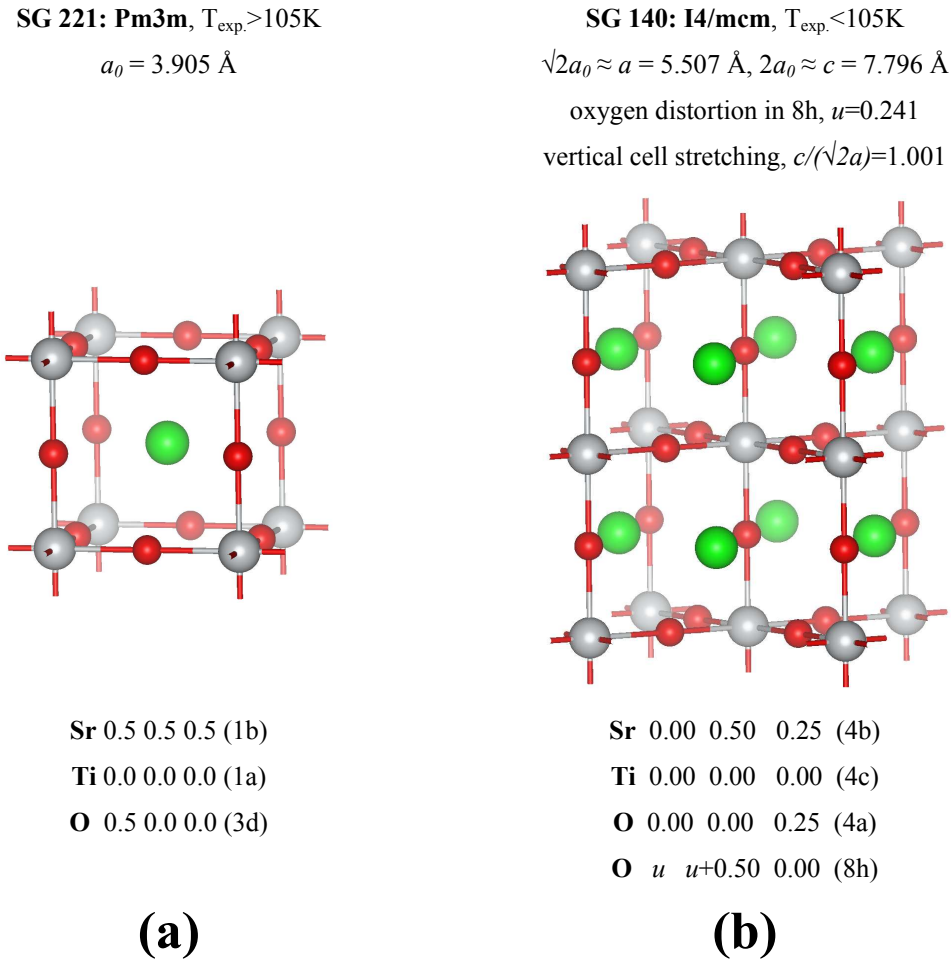
FIG. 6. Cubic (a) and tetragonal AFD (b) $SrTiO_3$ [107]. Sr atoms – green balls, Ti atoms – grey balls, O atoms – red balls. Atomic radii are not taken into account.

It is seen that O atoms are separated in two nonequivalent orbits: 4a (two atoms) and 8h (four atoms). The quadruple unit cell parameters in the undistorted pseudo-cubic structure are $a = b = a_0\sqrt{2}$, $c = 2a_0$, where a_0 is the lattice constant of the cubic phase. The structural parameter $u = 0.25$ defines the oxygen 8h position in the undistorted pseudo-cubic structure. Thus the

experimental cubic lattice parameter $a_0 = 3.905$ Å (at room temperature) gives the undistorted pseudo-cubic structure with $a = b = 5.522$ Å, $c = 2a_0 = 7.810$ Å which are close to the experimental $a = 5.507$ Å, $c = 7.796$ Å [85] for a real distorted tetragonal structure. The experimental value $u = 0.241$ [86] is close to $u = 0.25$ for the undistorted pseudo-cubic structure. Thereby the cubic-to-tetragonal phase transition can be considered as the tetragonal supercell generation with the transformation matrix $\begin{bmatrix} 110 \\ -110 \\ 002 \end{bmatrix}$ and the further small structural distortion.

The BO_6 octahedra distortions are considered often in terms of tilting (see [87] and references therein). By this one means the tilting around one or more of the BO_6 symmetry axes allowing greater flexibility in the coordination of the A cation while leaving the environment of the B cation essentially unchanged. The tilt of one octahedron around one of these axes determines (via the corner connections) the tilts of all the octahedra in the plane perpendicular to this axis. The successive octahedra along the axis can be tilted in either the same or the opposite sense (in-phase and out-of-phase tilts). The group-theoretical analysis of octahedral tilting is described in detail in Ref. [87] where was shown that the irrep associated with the out-of -phase tilts is R_{4+}

Table 5 shows the phonon symmetry in the $SrTiO_3$ crystal for Γ (0, 0, 0) and R (1/2, 1/2, 1/2) symmetry points of the BZ for a simple cubic lattice. The SG O_h^1 irreps (irreducible representations) are labeled according to Ref. [72]. The SG irreps are induced from those site symmetry group irreps, which correspond to transformations of the atomic displacements (x, y, z): t_{1u} of the site symmetry group O_h (Ti and Sr atoms); a_{2u}, e_u of the site symmetry group D_{4h} (O atom).

The symmetry of phonons in the AFD $SrTiO_3$ phase at the Γ point of the BZ is shown at Table 5 along with the splitting of the phonon frequencies due to lowering of the symmetry. The symmetry of acoustic phonons is $(a_{2u} + e_u)$, 8 modes are IR-active (3 a_{2u} + 5 e_u), 7 modes are Raman active (a_{1g}, b_{1g}, 2 b_{2g}, 3 e_g). The silent modes have the symmetry a_{1u} and b_{1u} in IR spectra and 2 a_{2g} in Raman spectra.

TABLE 5. Wyckoff positions and phonon symmetry in cubic and tetragonal AFD SrTiO$_3$ [107]

$Pm\bar{3}m$ O$_h^1$ (SG 221)			$I4/mcm$ D$_{4h}^{18}$ (SG 140)	
	Γ	R		Γ
Ti			Ti	
1a (0, 0, 0)			2c (0 0 0)	
O$_h$ t_{1u} (x, y, z)	4^- (t_{1u})	4^-	C$_{4h}$ a_u (z)	a_{1u} a_{2u}
			e_u' (x, y), e_u'' (x, y)	$2e_u$
				$t_{1u} \rightarrow a_{2u}$ e_u
Sr			Sr	
1b (0.5, 0.5, 0.5)			2b (0 0.5 0.25)	
O$_h$ t_{1u} (x, y, z)	4^- (t_{1u})	5^+	D$_{2d}$ b_2 (z)	a_{2u} b_{2g}
				$R_5^+ \rightarrow b_{2g}$ e_g
			e (x, y)	e_g e_u
				$t_{1u} \rightarrow a_{2u}$ e_u
O			O	
3d (0.5 0 0)			2a (0 0 0.25)	
D$_{4h}$ a_{2u} (z)	4^- (t_{1u})	1^+3^+	D$_4$ a_2 (z)	a_{2g} a_{2u}
			e (x, y)	e_g e_u
e_u (x, y)	4^- (t_{1u})	4^+5^+		$R_1^+ \rightarrow a_{2g}$
	5^- (t_{2u})			$R_3^+ \rightarrow e_g$
				$t_{1u} \rightarrow a_{2u}$ e_u
			O	
			4h ($-u$+0.5, u, 0)	
			C$_{2v}$ a_1 (z)	a_{1g} b_{2g} e_u
			b_1 (x)	b_{1g} a_{2g} e_u
			b_2 (y)	a_{2u} b_{1u} e_g
				$R_4^+ \rightarrow b_{1g}$ e_g
				$R_5^+ \rightarrow b_{2g}$ e_g
				$t_{1u} \rightarrow a_{2u}$ e_u
				$t_{2u} \rightarrow b_{1u}$ e_u

As it is seen from Table 5, a_{1g} and b_{1g} Raman active phonons arise due to the displacements of the O atoms only. The Raman active modes with the symmetry b_{2g} and e_g are Sr-O vibrational modes. The vibrations connected with Ti atom displacements are active only in IR spectra (a_{2u}, 5 e_u phonons). The information about the connection of the active vibrational modes with the displacements of concrete atoms makes the interpretation of the experimental IR and Raman spectra easier (*e.g.* see Chapter 4).

The calculations of phonon frequencies in a cubic high temperature phase (presented below) clearly demonstrates that the soft phonon mode symmetry is R_{4+} and in this way confirms the results of the group-theoretical analysis. Here we discuss our present phonon calculations and compare them with the data found in the experimental and other theoretical studies.

TABLE 6. Comparison of different combinations of hybrid functional and PP

Comp. set	$\Delta E_{cub.\text{-}tetr.}$, meV per u.c.	Cub.-tetr. distortion c/($\sqrt{2}$a)	TiO$_6$ rotation angle, °
PBE0 + SPP	−2.9	1.0011	0.9
PBE0 + PPP	1.6	1.0011	1.1
B3PW + SPP	−1.8	1.0014	1.1
B3PW + PPP	−1.3	1.0013	1.1
B3LYP + SPP	−3.0	1.0012	1.1
B3LYP + PPP	−3.4	1.0013	1.2
Expt.	(< 0)	1.0010 (*50K* [85])	2.1 (*4K* [56])
		1.0006	2.0 (*50K* [85])
		(*65−110K* [86])	1.4 (*77K* [56])

Table 6 contains comparative information on six combinations of hybrid functional and PP. Similarly to a comparison made on cubic phase (Table 1), no considerable difference can be seen (except we did not succeed to represent a total energy preference of the tetragonal AFD phase over cubic one in case of PBE0 + PPP though). Therefore the arguments of a comparison of the computational sets in Chapter 3.2 remain valid, and we continue using PBE0 + SPP set for the further calculations of phonons and thermodynamic comparison.

TABLE 7. AFD SrTiO$_3$ structural properties [107]

		LCAO (SPP)			PW	Expt.
		PBE	PBE0	B3PW	PBE	
Lattice constants, Å	a	5.594	5.532	5.545	5.566	5.507 (*50K* [85])
	c	7.922	7.831	7.854	7.908	7.796 (*50K* [85])
Cub.-tetr. distortion $c/(\sqrt{2}a)$		1.0014	1.0011	1.0014	1.0046	1.0010 (*50K* [85]) 1.0006 (*65−110K* [86])
O atom position, u, frac.		0.245	0.246	0.245	0.228	0.240 (*4K* [56]) 0.241 (*50K* [85]) 0.244 (*77K* [56])
TiO$_6$ rotation angle *arctg(1−4u)*, °		1.1	0.9	1.1	4.9	2.1 (*4K* [56]) 2.0 (*50K* [85]) 1.4 (*77K* [56])

The basic structural properties for the tetragonal AFD phase are presented in Table 7 for the LCAO with three different functionals and for the PW with PBE functional (we were unable to perform PW calculations with hybrid functionals as they are extremely time-demanding). Along with the two lattice constants a $(= b)$ and c, O-ion position parameter u and the relevant TiO$_6$ octahedra rotation angle are compared. Firstly, the LCAO calculations with the hybrid PBE0 functional and optimized BS give the best agreement with the experiment. Secondly, despite the results for PBE functional with different pseudopotentials and BSs (CRYSTAL09 and VASP 5.2 codes) for a cubic phase are quite similar (Table 3), they *differ* for the AFD phase (Table 7). In other words, the tetragonal distortion is well reproduced for the LCAO and overestimated for the PW. Obviously, this is not an effect of different pseudopotentials, but of different BSs. We attribute this to the problems of reproducing tiny structure modifications using the PW BS (*cf.* [59, 63, 106, 107]).

We analyzed cubic and tetragonal phase energies in details in Table 8. Two hybrid functionals, B3PW and PBE0, give moderate total electronic energy gain ΔE for the tetragonal AFD phase with respect to the cubic one, whereas for the PBE this gain is only 0.6 meV. It is also necessary to take also into account the zero-point vibration energies ΔE_{ZP} (second row) which results in a small AFD final energy gain (not exceeding 20 meV) for all the functionals used within the LCAO scheme. Calculating the zero-point energies, we compared the values for the cubic and

tetragonal AFD supercells with the *same* number of atoms. The temperature dependence of the Helmholtz free energies based on frequencies will be discussed below.

TABLE 8. Total electronic energy difference ΔE and zero-point energy difference ΔE_{ZP} (meV per unit cell) of cubic and tetragonal AFD SrTiO$_3$ phases with respect to the cubic phase, calculated via LCAO method (SPP) [107]

	PBE	PBE0	B3PW
ΔE	−0.6	−2.9	−1.8
ΔE_{ZP}	−12.4	−16.7	−14.5
Sum.	−12.8	−19.6	−16.3

Lastly, the phonon frequencies for the AFD phase are presented in Table 9 where the theoretical predictions for Raman, IR and silent modes are compared with the experimental data and theoretical PW-LDA [59] calculations (performed only for the IR phonons). As before, the hybrid functionals within the LCAO approach tend to overestimate the phonon frequencies compared with the experimental values whereas the GGA functional (combined within both the LCAO and PW approaches) tends to underestimate frequencies. The important observations are the following. (i) The PBE0 functional with optimized BS gives the best agreement with the experimental data (when available). (ii) The splitting of three IR cubic t_{1u} modes (denoted by curved brackets in Table 9) is predicted to be small, 2, 4 and 12 cm^{-1}. (iii) Several soft modes are found indicating a possible instability of tetragonal AFD phase at the temperatures close to 0°K as discussed in Ref. [59]. They are FE e_u and a_{2u} modes, which are found [106] to be imaginary for the set B3PW + PPP (confirming the results by Sai and Vanderbilt [59]) but real for the PBE0 + SPP.

44

TABLE 9. Phonon frequencies (cm^{-1}) in AFD $SrTiO_3$ phase (SPP) [107]

|	Mode	LCAO (SPP)				PW	PW	Expt.
		PBE	PBE0		B3PW	PBE	LDA [59]	(15°K)
			non-opt. BS	opt. BS				
Raman	a_{1g}	29	78	63	61	98	−	48 [84]
	e_g	48	99	79	76	17i		15 [84]
	e_g	137	168	146	144	183		143 [84]
	b_{2g}	152	181	158	157	140		(235 [84])
	b_{2g}	441	534	466	462	421		
	e_g	444	537	468	465	425		460 [84]
	b_{1g}	438	501	479	469	437		
	a_{2g}	440	502	480	470	434		
	a_{2g}	806	908	862	850	793		
Silent	b_{1u}	252	308	275	271	245		
	a_{1u}	430	478	458	452	410		
Infrared	a_{2u}	2	101	68	28	4i	90i	
	e_u	1	103	72	45	28i	96i	
	e_u	163	199	177	174	183		
	a_{2u}	180	211	189	187	158	157	185 [88]
	e_u	252	306	273	270	239	240	
	e_u	433	481	460	455	411	419	450 [88]
	e_u	523	597	549	542	504	515	
	a_{2u}	526	599	551	544	510		
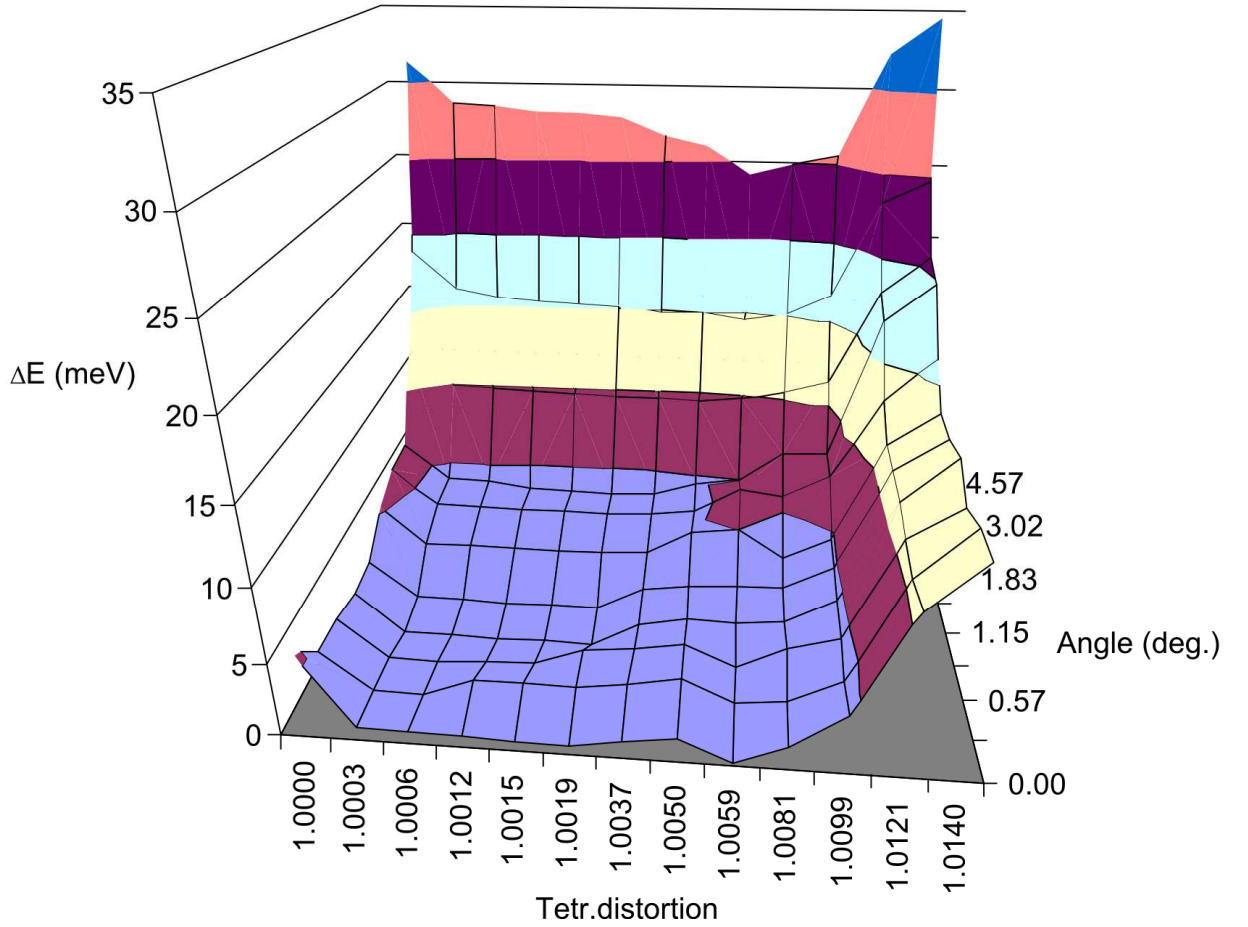
FIG.7. Tetragonal AFD SrTiO$_3$ total energy surface (dependence of $\Delta E_{tot.}$ on cub.-tetr. distortion c/√2a and TiO$_6$ octahedron rotation angle)

Fig. 7 shows a total energy surface of SrTiO$_3$ crystal per unit cell obtained with the PBE0 + SPP set with two released symmetry constrains in. These are TiO$_6$ octahedral rotation angle and tetragonal lattice stretch (cubic-tetragonal distortion c/√2a). The point of coordinate origin corresponds to a cubic crystal, the lowest area – to the found minimum of tetragonal phase. The energy difference between them is ~3 meV (Table 8). The complexity of the energy surface is seen, *i.e.* other local minima are present and the area around the global minimum is extremely flat. The surface character is even more complex for other computational sets, moreover it strongly depends on computational conditions, such as precision of bielectronic integrals evaluation and *k*-point sampling (see Appendix). Due to these features, a straightforward finding of tetragonal phase minimum is very difficult and requires noticeable efforts, which may explain that only a few computational works dealt correctly with the tetragonal crystal so far.

Note the remarkable form of the symmetric double-well potential obtained for ΔE on rotational angle dependence (only its right part is plotted in Fig. 7). According to [89] it is a classical example of anharmonic effect occurring in a soft mode displacive phase transition, governed by Landau theory. We met an attempt [90] in literature to estimate thermodynamic functions taking into account the effect of imaginary soft mode by means of approximation of double-well potential with a 4th degree polynomial. However, since our adopted computational set produces the soft mode phonons as real values (Tables 1, 3, 9), our task is somehow simplified. Finally, a proper account of anharmonic effects is beyond the subject of this thesis.

The soft phonon at the Γ-point of the cubic crystal induces the tetragonal ferroelectric (FE) (*P4mm*) structure. Note that in real crystals this phase would condense from the tetragonal AFD phase by means of splitting the FE soft mode of the cubic structure into E_u and A_{2u} phonon modes. This structure however was never observed in experiments and is considered to be suppressed by quantum fluctuations. Therefore it was studied here only for the aim of comparison. Moreover, its model is simplified since the TiO_6-octahedra rotation therein is neglected. Significantly, in such a case one should expect an occurrence of the AFD rotational soft mode. Indeed, it is obtained soft (imaginary for the B3PW+PPP and real for the PBE0+SPP), being split into a_2 and e modes (depending on which particular oxygen atoms in the TiO_6-octahedron are involved in the rotational motion).

3.4. Thermodynamic comparison of two phases

In temperature-induced phase transitions the anharmonicity effects play a fundamental role: the harmonic approximation generally yields imaginary frequencies for the soft modes at 0 K whereas at higher temperatures anharmonicity effects stabilize the soft modes to small but real frequencies. This is why the comparison of the calculated soft mode frequencies with experiments can be problematic. For example, it is seen (Table 1) that the PBE0 + SPP and B3PW + PPP sets treat the soft modes in $SrTiO_3$ differently, predicting real and imaginary frequencies respectively. By contrast, hard modes remain similar, and the harder the mode, the better its agreement with experiment. The same situation in general persists for the soft and hard modes of the tetragonal AFD phase, suggesting that our detailed comparison of computational sets was justified. As a consequence of this, the thermodynamic functions for the PBE0 + SPP and B3PW + PPP sets (Figs. 8 and 9) differ because imaginary modes in the latter case are neglected and do not contribute to the summation (Eqs. 4−5). Apparently, this affects the results when comparing the calculated thermodynamic functions to experiment (see the details also in [106]).

The temperature dependence of heat capacity has been calculated using Eq. 5 for both $SrTiO_3$ phases using all the above-mentioned computational sets in LCAO framework. The agreement with calorimetric experiment [91] is expectedly very good for those cases, where no imaginary modes were obtained, *i.e.* in a wide temperature range the calculated curves lie very close to the experimental line. In Fig. 8 we illustrate this by an example of PBE0 + SPP and B3PW + PPP sets. The former agrees much better with the experiment at $90 - 180$ K. To the best of our knowledge, the only heat capacity calculations [69] were performed so far for $SrTiO_3$ cubic phase using the all-electron linear augmented plane wave method (Wien2k code), the results are very close to our calculations.

Using CRYSTAL09 code, we calculated also the Helmholtz free energy for all the above-mentioned computational sets (Fig. 9) in LCAO framework as the function of the temperature according to Eq. 4 and present here the results for the PBE0 + SPP and B3PW + PPP sets. The imaginary frequencies observed in the case of the B3PW + PPP set confirm the presence of the AFD phase transition, but they also complicate correct calculations of the Helmholtz free energy. Note, that the results of the LDA [59] and HSE06 [63] calculations (PW framework) agree concerning the presence of imaginary frequencies (Table 3 and 9).
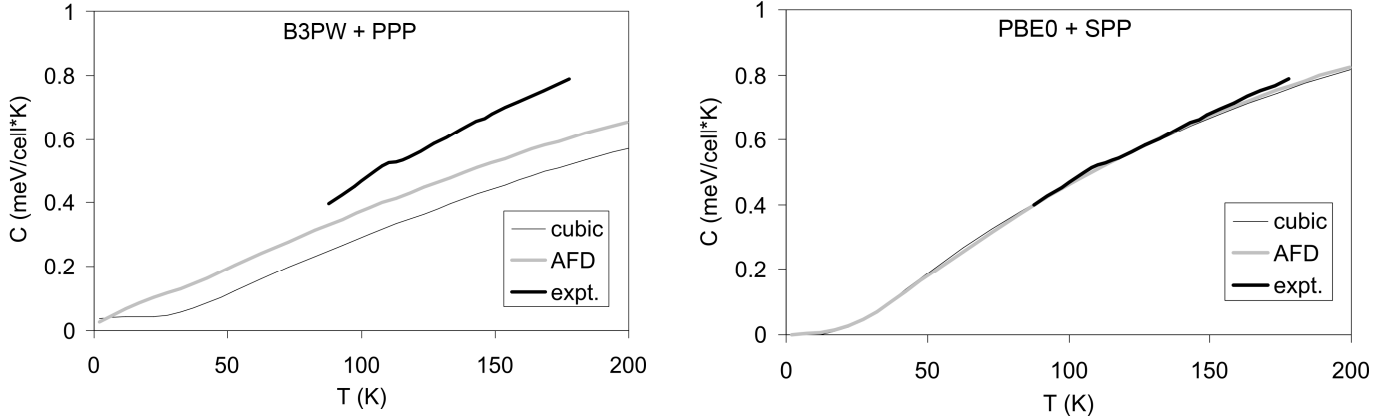
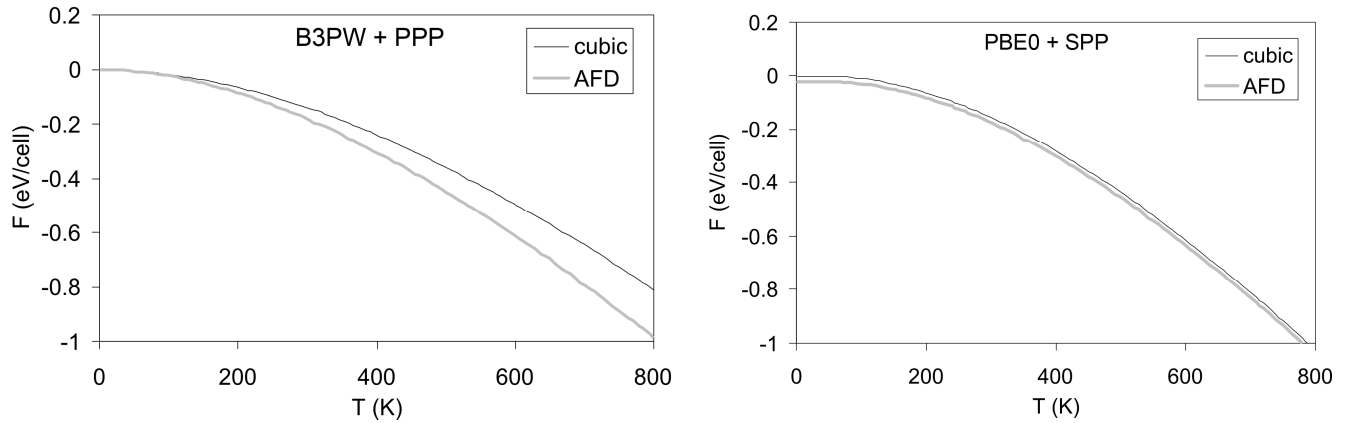FIG. 8. The calculated and experimental ([91]) heat capacity of SrTiO₃

FIG. 9. The calculated Helmholtz free energy of SrTiO₃

Above 150 K the B3PW + PPP set shows a noticeable energetic preference for the AFD phase over cubic one, which tends to rapidly increase with the temperature (Fig. 9). This contradicts the experimental fact, that the cubic phase is preferred at high temperatures. For the PBE0 + SPP, as temperature rises from zero to 300°K, the free energies for both phases decrease by ~0.2 eV per cell. The energy curve for the AFD phase slowly approaches that of the cubic phase (being below at ~20 meV near 0 K) and finally crosses it near 1000 K. However, experimentally these curves intersect at the phase transition temperature. We assume that this contradiction occurs due to the use of the harmonic approximation and the discrete phonon spectrum used in Eq. 4. As a result, our calculation accuracy becomes comparable with the aforementioned energy differences for the two phases.

3.5. Conclusions

(1) The group-theoretical analysis of the phonon symmetry indicates that in a defect-free $SrTiO_3$ the observed AFD phase transition is caused by a softening of the R_4^+ phonon mode, no other modes are necessary. This is in complete agreement with our calculations. We performed also classification of the calculated frequencies into the Raman, IR and silent modes.

(2) Detailed calculations of phonon frequencies in the tetragonal phase have been performed. The splitting of the phonon frequencies $t_{1u} \rightarrow a_{2u} + e_u$ due to AFD phase transition is predicted to be rather small, $2-12$ cm^{-1}. Experimentally known low temperature Γ- and R-phonon instabilities are reproduced in the cubic $SrTiO_3$. Our calculations confirm the co-existence of the soft phonon modes for the cubic phase at the Γ and R points of the BZ which was discussed earlier [59, 64, 65]. In the tetragonal AFD phase the FE soft mode, split into e_u and a_{2u} modes, is detected. In turn, in the tetragonal FE phase the AFD soft mode, split into a_2 and e modes, is detected.

(3) A comparison of the heat capacities and free energies vs. temperature is performed *ab initio* for the first time for cubic and tetragonal AFD $SrTiO_3$ phases. The experimentally measured heat capacity between 90 and 180 K is successfully reproduced. The gain in free energy of the tetragonal AFD phase with respect to the cubic phase is obtained though the experimental temperature dependence is not exactly reproduced.

(4) The hybrid HF-DFT functionals with both types of BS (LCAO and PW) are all shown to accurately reproduce the electron and phonon properties of $SrTiO_3$. However, they differ in predicting soft phonon modes, resulting in either small real or imaginary frequencies respectively, thus contributing differently to the thermodynamic functions.

(5) The use of the hybrid HF-DFT functionals gives better phonon frequencies compared to the GGA-type functionals. Another advantage of the hybrid functionals is the accurate band gap reproduction, in contrast to its strong underestimation while using the GGA functionals, which in particular can be important for defect calculations. Furthermore, with the use of hybrid functionals, no explicit preference to the LCAO or PW approach in phonon calculations could be given. One should note that the LCAO hybrid DFT calculations in CRYSTAL09 are much faster compared with (extremely time consuming) PW hybrid DFT calculations in the VASP 5.2 code. On the other hand,

a comparison of the phonon frequencies and atomic structure of the cubic and tetragonal AFD SrTiO$_3$ phases calculated within the LCAO approach using optimized and non-optimized BS clearly demonstrates that the BS optimization gives much better results.

(6) Based on this experience for defect-free SrTiO$_3$, a combination of PBE0 and SPP within LCAO framework is chosen for further treatment of more complex systems. We use the selected computational scheme for further thermodynamic studies of defective perovskites under finite temperatures. This is important for the prediction of the material properties and device performance (*e.g.* sensors and solid oxide fuel cells) under realistic operational conditions.

4. Defective SrTiO₃ bulk

4.1. Literature overview

This Chapter deals with substitutional iron impurity Fe^{4+} and oxygen vacancy V_O (neutral charge state) as the characteristic point defects in ABO_3-type perovskites. For both types of defects particular attention is paid to the Jahn-Teller effect and its consequences, with respect to defect-induced energy levels in the band gap and defect-induced localized modes in the phonon spectra. We estimate phonon contributions to the oxygen vacancy formation energy as a function of temperature and compare them with the available experimental data. Defect complexes are also discussed.
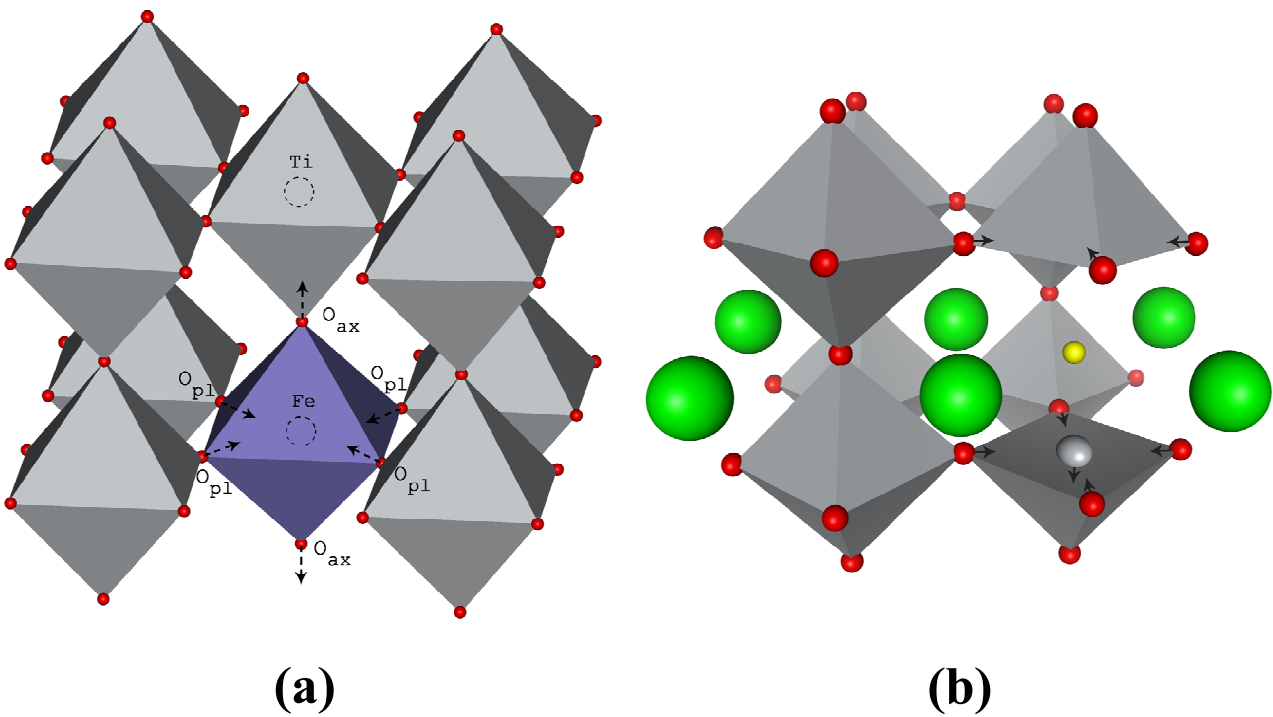

(a) **(b)**

FIG. 10. The atomic structure of SrTiO₃ with iron impurity (a) and oxygen vacancy (b). The arrows show the relaxation pattern around the defect. The (a) is taken from [119].

The Fe-doped SrTiO₃ crystal is of special interest since iron impurity substituting Ti^{4+} can exhibit both the 3+ and 4+ oxidation states and therefore acts as a redox center. The Fe^{4+} impurity substituting a regular Ti^{4+} ion in SrTiO₃ crystal serves as a reference model for many similar systems and is important for several technological applications, *e.g.* electro- and magneto-optics [11]. The defective $Sr(Fe_xTi_{1-x})O_3$ solid solutions are relatively well studied both experimentally (*e.g.* [9]) and computationally (*e.g.* [92, 93]). However, the number of studies on vibrational properties of these

systems is very limited. Only two Raman [94, 95] and one IR [94] measurements on $Sr(Fe_xTi_{1-x})O_3$ solid solution powders were performed so far, whereas no attempts were undertaken to investigate vibrational spectra theoretically from the first principles. In this context, phonon studies of other defective crystals may be mentioned, *e.g.* of iron-doped CoO [96].

As mentioned above, the oxygen vacancy is a very common defect in ABO_3-type perovskites, controlling mass transport in permeation membranes and solid oxide fuel cell cathodes [9, 97−99]. There are more than 25 papers dealing with *ab initio* calculations of the atomic and electronic structure for V_O in $SrTiO_3$ (follow references in [100]). However, the common problem of these calculations is the use of the standard DFT exchange-correlation functionals (LDA/GGA) or parameter-dependent functionals like hybrid HSE or DFT+*U*. As is well known (see Chapter 2.1), the LDA/GGA approaches strongly underestimate the band gap of $SrTiO_3$ with the result that the energy level of the vacancy (which is a shallow donor) falls into the conduction band, instead of lying in the band gap. On the other hand, the DFT+U functional suggested several scenarios for the position of the defect level, depending on the on-site Coulomb interaction (Hubbard *U*-parameter) [101, 102]. Its choice affects not only the band gap value but also the preference of the oxygen vacancy in different charge states by total energy. Moreover, the optimized fraction of the exact exchange then varies from material to material. Another common feature of the standard DFT calculations combined, as a rule, with the PW BS, is the negligible electron density concentration in the oxygen vacancy, in contrast to the considerable electron density in the vacancy obtained using more flexible calculations based on the atomic (LCAO) BS [100, 103]. This could considerably affect the optimized atomic and electronic structure of the point defects, even in the calculations of neutral supercells.

A few calculations only used the *hybrid* exchange-correlation functionals for point defect calculations in perovskites [100, 102−105]. These functionals yield accurate description of the structural, electron and phonon properties of the perfect $SrTiO_3$ [107]. Here we calculate the defect-induced phonon spectrum, which is necessary for the interpretation of Raman experiments [94, 108] for both types of defects and the prediction of the temperature dependence of the defect formation energy.

Complexes of oxygen vacancies and iron impurities in $SrTiO_3$ play a key role in electrooptical applications and non-volatile resistive random access switching memories [11]. For example, the understanding of the relative spatial distribution of Fe ions and V_O is important to explain the formation of the conductive filaments [4]. An association of these defects (Fe–V_O) has been addressed by a number of approaches [94, 109−114]. It has been shown by electron

paramagnetic resonance, that there is a perceptible attraction between iron impurity and V_O yielding $Fe^{3+}-V_O$ complexes even at dopant concentration below 0.1 at.%, while such defect pairs are dissociated at temperatures above 300°C [109]. We study below the effect of iron impurity and V_O interactions in the first and more distant coordination shells in $SrTiO_3$, in order to interpret the recent x-ray absorption near edge structure (XANES) experiments on resistive switching structures [112, 113] and predict the relevant phonon spectra.

4.2. Fe^{4+} impurity

Three different concentrations of the Fe^{4+} impurity (12.5%, 6.25% and 3.13%) were modeled using 80- and 160-atom supercells. To model 6.25% and 12.5% iron contents, we used the same 80 atom supercell containing one and two iron atoms, respectively. Very high precision settings are required for phonon calculations in CRYSTAL09 code (see Appendix and [119]). That is why a treatment of even the moderate-size supercells at the moment is quite a demanding task. Thus, in this study only the phonons for 6.25% iron content are reported, which, however, falls into range of defect concentrations studied experimentally [94].

As is well known [92], the Fe^{4+} substituting host Ti^{4+} ions in $SrTiO_3$ exhibits the high-spin d^4 state with $S = 2$, *i.e.* the e_g energy level is occupied by a single α-(spin-up) electron, whereas three other α-electrons occupy t_{2g} states. This results in Jahn-Teller $E \otimes e$ effect and asymmetrical relaxation of six nearest oxygen atoms surrounding iron impurity (Fig. 11). The geometry optimization in our calculations resulted in tetragonal symmetry D_{4h}. Confirming both general theoretical considerations [115, 116] and the results of the earlier computer modeling [93], the Jahn-Teller displacement pattern of the oxygen atoms around the Fe^{4+} impurity was reproduced (four planar oxygen atoms are displaced towards and two axial – outwards the defect). Along this, an opposite pattern was also obtained (Fig. 11). Being not forbidden by the Jahn-Teller theorem, it was however found to be slightly unpreferable (< 0.1 eV for all the defect concentrations), and such a small difference may suggest a coexistence of these two isomeric configurations though.
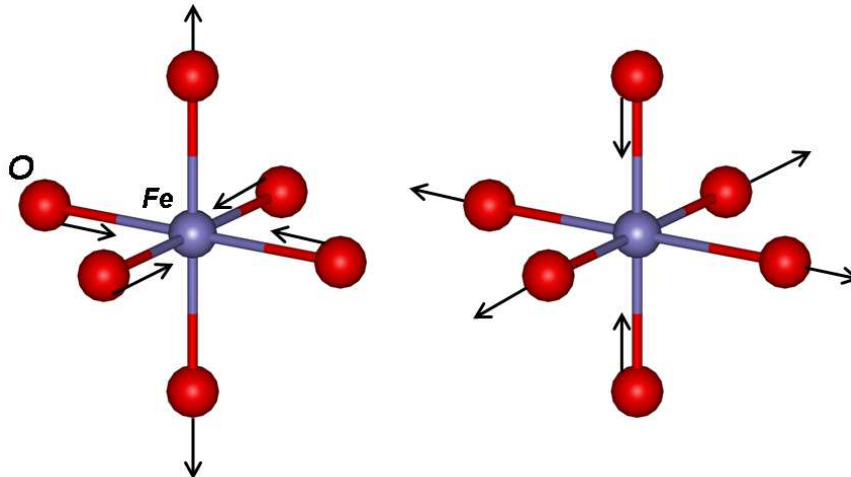

FIG. 11. Two possible Jahn-Teller relaxation patterns in Fe^{4+}-doped $SrTiO_3$. Left one is found to be preferable on ~0.04 eV at 12.5% Fe.

Both lattice parameters and internal atomic coordinates were optimized to obtain the fully relaxed structures. As a result, the defective crystal structure (started at the cubic symmetry) was reduced to a *tetragonal* symmetry (point group D_{4h}, SG *P4/mmm* for 12.5% iron and *I4/mmm* for 6.25%). Despite the small additional total energy gain (< 0.03 eV per supercell) resulting from the tetragonal lattice distortion, the difference in tetragonal lattice parameters c and $a = b$ reaches 0.07 Å, with the trend to decrease for a very small (3.125%) iron content.

Additional attempt to model the even lower, monoclinic symmetry (SG *Cm-C_s^3*) was performed, but no energy difference with a tetragonal symmetry was found.

TABLE 10. Calculated structure relaxation around single Fe^{4+} impurity in $SrTiO_3$ [119]

Supercell	Iron content (%)	d_{Fe-Fe} (Å)	Distances (Å), displacements in brackets		E_{relax} (eV)
			Fe – 4 × O planar	Fe – 2 × O axial	
80-atom	12.5	7.80	1.90 (−0.06)	2.03 (+0.07)	0.24
80-atom	6.25	11.08	1.88 (−0.08)	2.07 (+0.11)	0.37
160-atom	3.13	13.57	1.88 (−0.08)	2.07 (+0.11)	0.39

The results concerning structural optimization are presented in Table 10. It is seen that the defect concentration decrease leads to an increase of the oxygen ion displacements (Fig. 11), confirming both the theoretical [93] and experimental [94] findings. The increase of a distance between periodically distributed Fe impurities (*i.e.* smaller defect concentrations in the supercell model) results in larger lattice relaxation energies, which, however, saturate at a concentration of 6.25%. That is, a 80 atom supercell is sufficiently large [119] for defect modeling.

In agreement with previous calculations of the Jahn-Teller distortion [92], four (planar) O atoms were displaced by 0.08 Å inwards whereas two (axial) O atoms by 0.11 Å outwards Fe ion (given for 3.125% Fe, the changes between 6.25% and 12.5% Fe are insignificant). The lattice energy gain due to Jahn-Teller-type optimization is quite considerable, 0.39 eV per supercell. The dispersion of the Fe-impurity band (within $SrTiO_3$ band gap) strongly decreases, from 1.6 eV for 12.5% to 0.16 eV for 6.25% and 0.1 eV for 3.125% of Fe content. Thus, one can conclude that the Fe concentrations not exceeding 6.25% are necessary to model single Fe^{4+} defects in $SrTiO_3$.

The Mulliken atomic charges indicate a considerable covalency of the Ti-O bonding (2.33 e (Ti), -1.46 e (O), 1.95 e (Sr)). The calculated Fe charge (2.2 e) is close to the Ti charge and indicates a considerable Fe−O bond covalence. The Fe magnetic moment 3.6 μ_B is close to that expected for a pure ionic model (4 μ_B).

The phonon calculations were performed for the distorted structures with a fixed spin S=2 (which corresponds to the insulating state), using the 80- and 160-atom supercells with a tetragonal symmetry. According to the tetragonal symmetry D_{4h}^{17}, three types of phonon modes are allowed: Raman-active (e_g, a_{1g}, b_{1g} and b_{2g}-type), IR-active (e_u and a_{2u}) and silent (a_{1u}, a_{2g}, b_{1u} and b_{2u}) modes. Two acoustic modes (e_u and a_{2u}-type) with frequencies close to zero were also obtained. It should be noted that the phonons of the defective system were calculated at the BZ center of such large supercell. Notice that the calculations on Fe^{4+} in $SrTiO_3$ in point symmetry group D_{4h} give practically the same total energy per unit cell and phonon frequencies as those assuming the point symmetry group C_{4v} with an inversion center lacking.

TABLE 11. A comparison of calculated and experimentally observed TO phonon frequencies (cm^{-1}) in $SrTiO_3$ with Fe^{4+} impurity [119]

Expt. [94] 10% iron	Modelling in C_{4v} symmetry 6.25% iron	Modelling in D_{4h} symmetry 6.25% iron
Raman		
170	170 (a_1)	162 (b_{1g}), 178 (a_{1g})
250	242 (b_1), 243 (a_1)	239 (b_{2g})
475	469 (e), 478 (e)	475 (b_{2g})
545	539 (e), 546 (a_1)	547 (a_{1g})
690	754 (a_1)	752 (a_{1g})
IR		
408	421 (e)	422 (e_u)
445	442 (a_1), 459 (e)	442 (a_{2u})
645	615 (a_1)	624 (a_{2u})

Based on the selection rules, a possible assignment of the experimentally observed Raman and IR frequencies was suggested (Table 11). For defect-free cubic $SrTiO_3$ no first-order Raman-active frequencies are allowed according to the selection rules (Chapter 3). Such frequencies arise however upon material doping [120].

The total and partial phonon densities of states (DOS) were calculated according to Ref. [96]. The theoretical DOS is plotted in Fig. 12 and 13 and can be compared with the results of IR and Raman measurements [94] on oxidized $Sr(Fe_{0.1}Ti_{0.9})O_3$ powders containing only Fe^{4+} impurities. It should be noted, that the phonons of the defective systems were calculated only at the BZ center of a supercell. The inclusion of the Fe^{4+} impurity into the otherwise perfect crystal does not change the DOS considerably compared with the perfect crystal. Note also the experimentally extracted phonon DOS [83] for a perfect crystal (Fig. 4). First, the calculated and experimentally extracted DOS for a perfect crystal reasonably agree, except for the experimental peak at 700 cm^{-1} which is shifted in the calculations to 800 cm^{-1} (Figs. 4, 12, 13). In general, a perfect phonon DOS changes inconsiderably upon iron doping since Fe and Ti vibrations fall within the same frequency range (see the partial DOS in Fig. 13). One can recognize the formation of three groups of Fe-related modes around 150, 300 and 500 cm^{-1}. The phonons involving iron atom movements are always of e_u or a_{2u}-type for D_{4h} symmetry. Indeed, the double degenerate e-type vibrations correspond to the mutually perpendicular Fe movements in a plane of four planar O atoms, whereas the a-type vibrations are out-of-plane Fe motions in the directions of two axial oxygen atoms surrounding an impurity. The highest Raman frequency (690 cm^{-1}) is due to a *localized* O stretching vibration mode without Ti and Fe ion motions whereas the other modes arise due to different types of (Ti, Fe)-O vibrations (see the partial DOS in Fig. 13).

We omit here an analysis of the phonon contribution into iron impurity formation energy. Currently, no reliable experimental data exist for the Fe impurity formation energy in perovskites, which could be compared with the theoretical Gibbs free energies. This however is done for oxygen vacancy formation energy (see Chapter 4.3).
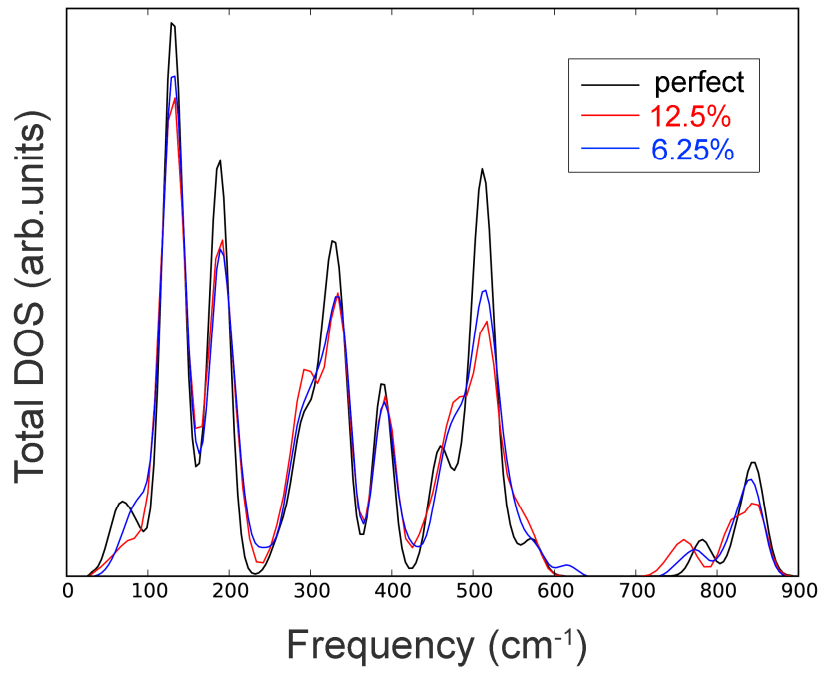
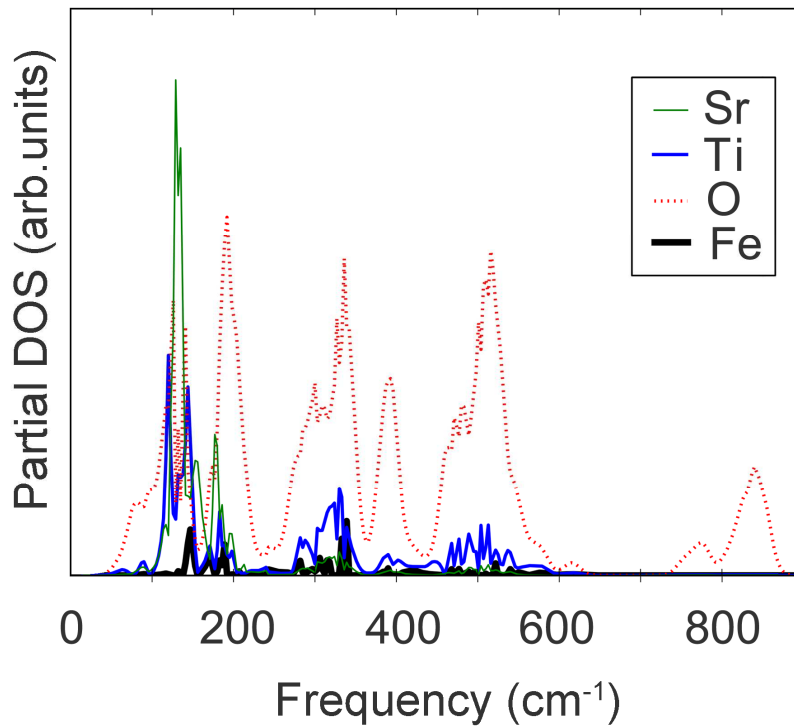FIG. 12. The calculated total phonon DOS for perfect and Fe^{4+}-doped (12.5% and 6.25%) $SrTiO_3$

FIG. 13. The calculated atom-projected phonon DOS for Fe^{4+}-doped $SrTiO_3$. The concentration of Fe^{4+} defect is 6.25%. Fe contribution in partial densities is multiplied by a factor of 5 [120].

4.3. Oxygen vacancy

In the calculations of oxygen vacancies V_O we consider a neutral supercell. However, the electron density of the two electrons (remaining from the missing O atom) is re-distributed between the vacancy and the nearest Ti ions to minimize the total energy of a system. We kept the basis functions from the missing oxygen in the vacancy site (so-called ghost atom basis) which considerably improves the agreement of calculated defect formation energy with the experiment (see below). According to the experimental data extrapolated to 0°K [117], the V_O formation enthalpy (with respect to an O atom in a free O_2 molecule) is ~6.1 eV. Its energy level ($V_o/V_o^\bullet$ redox level) lies very close (< 0.1 eV) to the conduction band bottom whereas the $V_o^{\bullet\bullet}/V_o^\bullet$ redox level lies deeper, *i.e.* ~0.3 eV.

Our vacancy calculations suggest the supercell symmetry D_{2h} with the resulting effective charge of the vacancy close to $V_o^\bullet$ and the triplet magnetic state lower in energy than singlet (~0.2 eV per supercell), in agreement with a recent study [102]. The defect energy level at the Γ point of the Brillouin zone (BZ) lies ~0.4 eV below the conduction band but overlaps with it at the other points of the BZ (Fig. 15). The additional energy reduction responsible for the lifting of double degeneracy of the highest occupied energy level (the Jahn-Teller effect) is 70 meV per supercell for 12.5% V_O (symmetry lowers from D_{4h}^1 to D_{2h}^1) and 30 meV per supercell for 6.25% V_O (symmetry lowers from D_{4h}^{17} to D_{2h}^{23}). Note, that the Jahn-Teller effect was experimentally observed for Ti^{3+} ions after photoexcitation of a pure crystal [118].
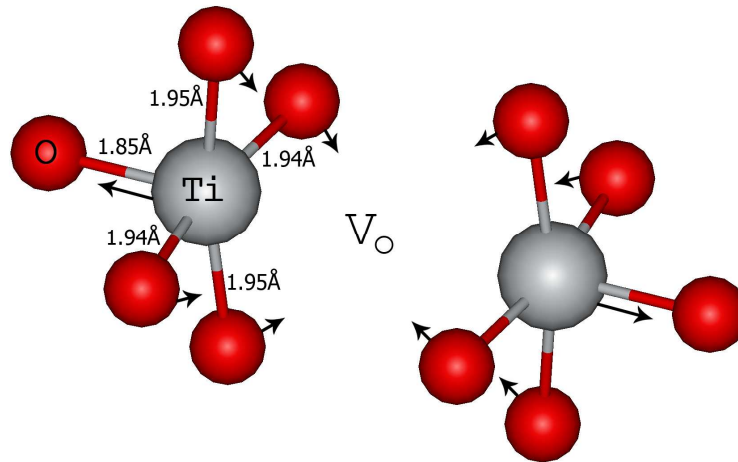

FIG. 14. The equilibrium atomic structure with the Jahn-Teller distortion around Ti^{3+} ions [120] near the oxygen vacancy. Atomic radii are not taken into account.

Four O ions in the plane perpendicular to the $Ti - V_O$ axis are divided into two nonequivalent pairs and displaced slightly towards the V_O (Fig. 14). This results in a local lattice distortion which manifests the Jahn-Teller effect. It is interesting to note, that the distortion pattern here (axial Ti-O bond shortened relative to planar Ti-O, as expected from a simple ligand-field model for the case of one electron in otherwise degenerate t_{2g} orbitals) is opposite to the preferable Fe^{4+} case (axial bonds elongated, decisive Jahn-Teller contribution arising from the single electron in the e_g orbitals). With the decrease of the defect concentration from 12.5% to 6.25% the dispersion of the defect band throughout the BZ decreases drastically (from ~1.0 eV down to ~0.2 eV), although the displacement pattern and the charge redistribution around the V_O does not change considerably.

As a result, the charge and spin density of electrons remaining from a removed O atom are quite delocalized in the vicinity of the defect. Two Ti ions are strongly displaced outwards the V_O by 0.11 Å along the (100) axis in the direction of two (axial) O ions which move slightly towards them.

TABLE 12. Calculated properties for V_O in $SrTiO_3$ (concentration 6.25%): d_{v-v} is the distance between V_O, z_{Mull} / μ are the Mulliken atomic charges / the spin magnetic moments, ΔG_F^0 is the standard Gibbs free formation energy at 0°K (the zero-point vibrations of the solid phase and the oxygen molecule are included in parenthesis). Positive and negative sign for the displacements denote outward and inward displacement of the ions with respect to the V_O site. FM and NM stand for ferromagnetic and non-magnetic solution, respectively.

d_{V-V} (Å)	Magnetic configuration	Distances (Å), displacements in parenthesis			z_{Mull} (e) / μ (μ_B)		ΔG_F^0 (eV)
		$V_O - 2 \times Ti$	$Ti - 4 \times O_{pl}$	$Ti - O_{ax}$	V_O	$2 \times Ti$	
11.08	FM	2.04 (+0.08)	2 x 1.94 (−0.02) 2 x 1.95 (−0.01)	1.85 (−0.11)	0.5 / 0.4	2.2 2.2 / 0.2 0.2	6.26 (6.24)
	NM	1.89 (−0.07)	1.94 (−0.02)	2.04 (+0.08)	0.7	2.2 2.2	6.59

Table 12 shows the distances between V_O and two nearest Ti ions ($V_O - 2 \times Ti$) for $SrTiO_3$. The five remaining O ions around these Ti ions are classified as four planar ($Ti - 4 \times O_{pl}$) and one axial ion ($Ti - O_{ax}$). As pointed out above, V_O in $SrTiO_3$ has two electrons of missing oxygen being partly localized on nearest Ti neighboring ions. In such a case the open $3d$-electron shells of Ti ions suggest a spin-restricted solution for $SrTiO_3$ with V_O. We considered a triplet (ferromagnetic FM) spin state with parallel spin alignment for the two Ti ions, a singlet (anti-ferromagnetic AFM) spin state with anti-paralell spin alignment for the two Ti ions and a non-magnetic (NM) solution. Interestingly, there is a considerable electronic charge in the vacancy due to the use of the ghost basis functions (Table 12). Moreover, the magnetic moment of V_O is 0.4 μ_B larger than that of the Ti ions (0.2 μ_B). Note that our results for the local magnetic moment of Ti ions and the energy difference above are similar to those by Hou and Terakura [102]. The FM case is energetically more favorable than the NM and AFM ones by ~0.32 and 0.27 eV per supercell, respectively. Further, the FM case with the ghost basis functions is energetically preferable by almost 0.30 eV per supercell over the case without ghost basis functions. This is why we used the triplet spin state and ghost basis functions in our calculations of the phonon contribution to the Gibbs free formation energy of V_O in $SrTiO_3$.
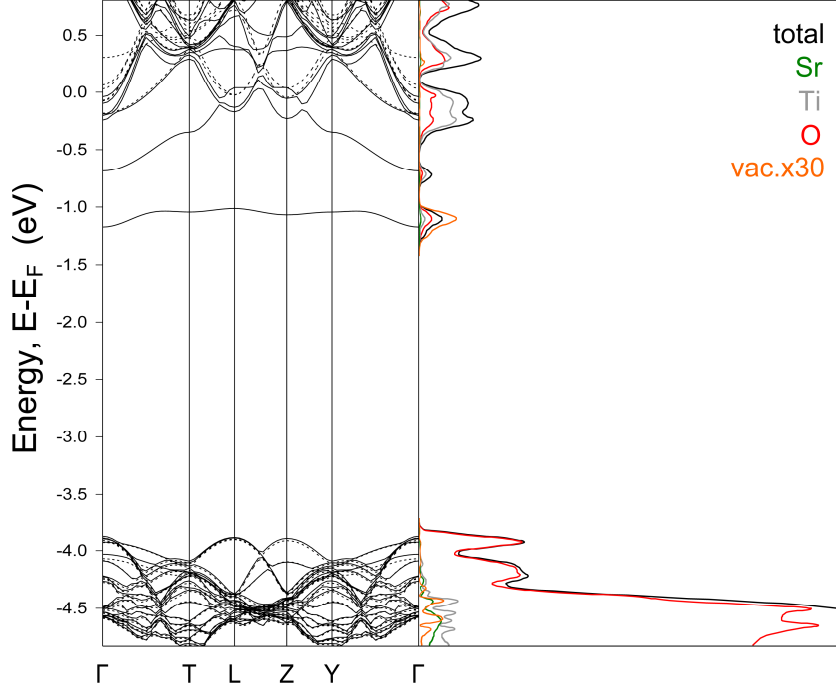
FIG. 15. The band structure and density of states of reduced $SrTiO_3$ (FM solution). The concentration of V_O is 6.25%. The impact of V_O in projected DOS is multiplied by a factor of 30. Solid and dashed lines denote α and β electrons, respectively. The zero of energy scale corresponds to the theoretical Fermi level E_F.

The analysis of band structure for defective $SrTiO_3$ (Fig. 15) reveals that, since the FM solution and Pauli principle formally prohibit the two electrons of a missing oxygen atom to occupy the same energy level, the Jahn-Teller effect occurs with the splitting of NM defect level into two new energy levels. Fig. 15 shows that one defect level at the Γ-point of the BZ lies ~0.6 eV, whereas the other one ~1.2 eV below the conduction band bottom, thus suggesting a strong electron density delocalization. A qualitatively similar pattern at the Γ-point has been discussed by Hou and Terakura [102]. Note, however, that the upper defect energy band shows large dispersion and falls into the bottom of the conduction band at the boundary of the BZ. They also pointed out that the NM solution leads to the pattern with two electrons occupying the same defect level in the band gap which is in agreement with the recent results [103]. In addition to their findings, our calculations suggest supercell symmetry reduction to D_{2h} (due to the Jahn-Teller effect) with almost singly ionized oxygen vacancy [120]. The four planar O atoms around each of the two Ti-centers near V_O, being equivalent in the NM solution, split into two pairs in the FM solution and are displaced differently, by −0.01 and −0.02 Å (Table 12). The calculated defect formation energy

$\Delta G_F^0 = 6.26$ eV in $SrTiO_3$ is very close to what can be extrapolated at 0°K (~6.1 eV) from the experimental temperature dependence [120]. Thus, the the 80-atoms supercell is needed to converge the formation energy at 0°K due to a strong electron density delocalization around V_O in $SrTiO_3$. Interestingly to note, that the contribution of zero-point vibrations to the formation energy in $SrTiO_3$ is very small, 0.02 eV (Table 12).

TABLE 13. Comparison of calculated and experimentally observed transverse optical Raman phonon frequencies (cm^{-1}) for reduced $SrTiO_3$ (SG 69, D_{2h}^{23}) [120]. Frequencies marked by ~ were estimated from the experimental spectrum, those marked by asterisks were observed in defect-free tetragonal $SrTiO_3$ below 105 K

Expt. [108]	Modeling 6.25% V_O
~135	135 (a_g)
144*	146 (b_{2g})
~175	174 (b_{2g})
445*	446 (b_{3g})
505	505 (b_{2g})
~555*	561 (a_g)
630	643 (a_g)
700	753 (a_g)

Analyzing the calculated phonon eigenvectors, one can suggest an assignment of the observed Raman spectra (Table 13). In agreement with Ref. [108], the mode with frequency ~135 cm^{-1} is not related to the vacancy but to Sr ion motion, the frequencies of 505 and 630 cm^{-1} correspond to the relative motion of Ti and O ions near the vacancy, whereas the highest frequency around 700 cm^{-1} mainly refers Ti-O stretching vibrations nearby the vacancy. One can see the last modes in Table 13 are absent in the perfect crystal and are caused by the particular vibrations of oxygen atoms around the V_O (*i.e.* localized defect-induced phonon modes, see Fig. 16).
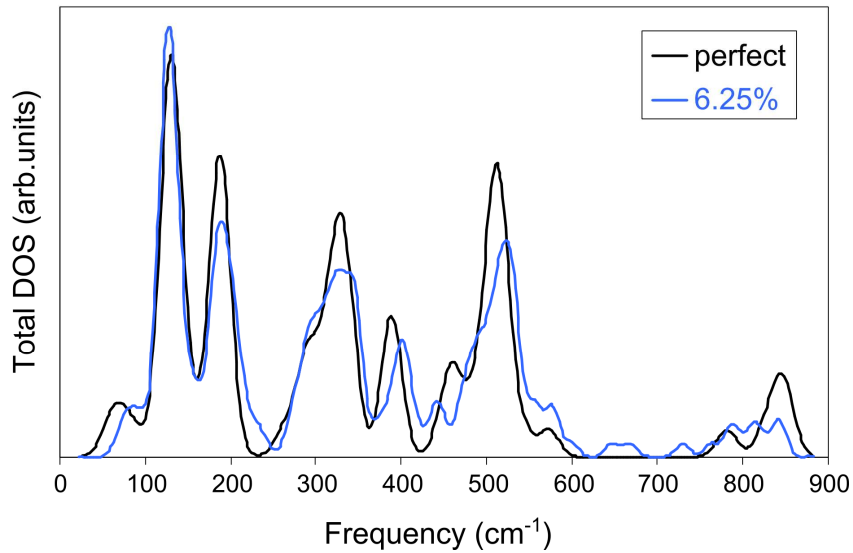
FIG. 16. The calculated total phonon DOS for perfect and reduced (6.25%) SrTiO$_3$

According to Eq. 9, the calculated ΔG_F^0 and its temperature dependence is presented in Fig. 17 with and without taking into account the phonon contribution in the crystalline phase, which is typically neglected in the literature (see Chapter 2.4). The agreement of the calculations for 6.25% of oxygen vacancies with experiments is very good (see details in [120]). A larger defect concentration of 12.5% (usually used in the literature) overestimates the defect formation energy at 0 K by ~0.3 eV. Neglecting the ghost BS would lead to an additional total energy overestimate of ~0.5 eV per unit cell. As expected, the phonon contribution is more significant (~0.1 eV) at higher temperatures. When comparing theory and experiments, one has to keep in mind that the point defect concentrations (defining the extracted mass action constants) in Ref. [117] were considered at high temperatures (1300-1700°K). Thus, small deviations in the slope of measured temperature dependence may affect the reliability of the extrapolated experimental data at low temperatures.
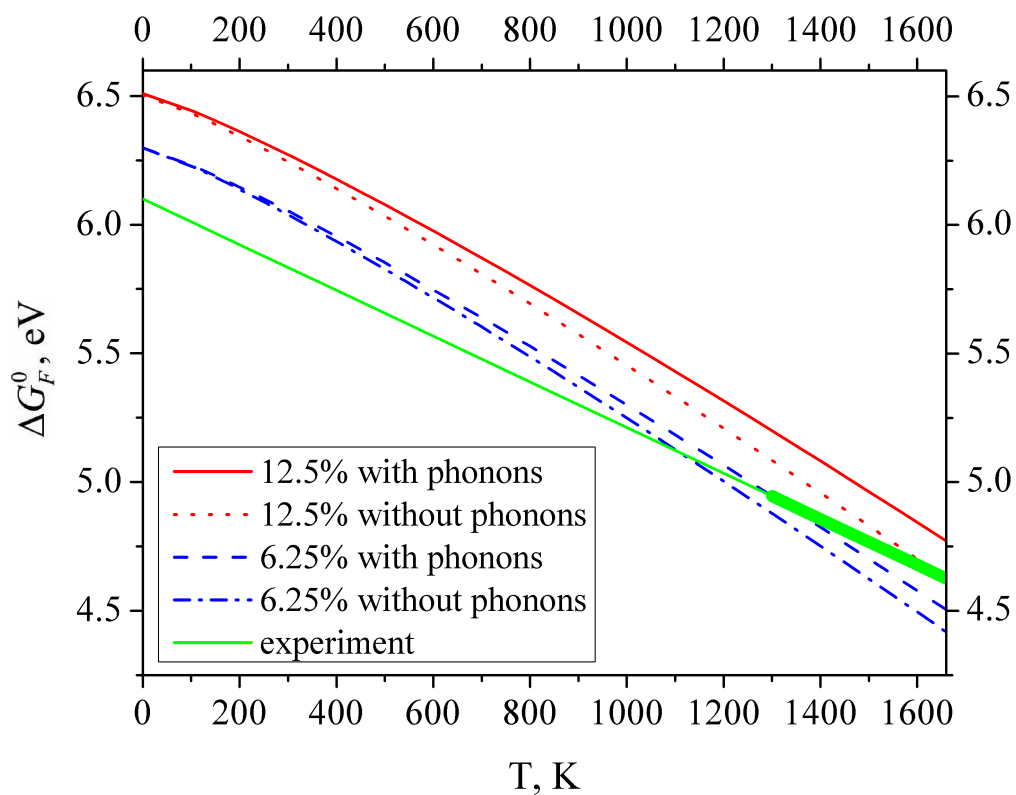
FIG. 17. The calculated Gibbs formation energy ΔG_F^0 for V_O as a function of temperature and its comparison to the experiment [117]. Bold (green) part of the experimental line corresponds to the temperature range of the actual experiments whereas the rest of the line is an interpolation to low temperatures [120].

4.4. $Fe^{3+}-V_O$ defect complexes

Four structural models schematically shown in Fig. 18 were studied. The first, containing the isolated iron impurity, was considered in Chapter 4.2 and appears here for the purpose of comparison. The rest of models contain one V_O and two Fe atoms per supercell, thus forming a neutral defect complex (following the formal ionic charges Sr^{2+}, Ti^{4+}, O^{2-}, Fe^{3+}). Calculated magnetic moments of iron impurity (3.6 μ_B for Fe^{4+} in model 1 and 4.3 μ_B for Fe^{3+} in the rest of models) follow the Hund's rule of high spin on Fe ions and confirm partial covalency of the chemical bonding in $SrTiO_3$. Experimentally it is not known how the iron impurities and oxygen vacancies are distributed across the $SrTiO_3$ matrix, because the extended x-ray absorption fine structure (EXAFS) technique [112] can only distinguish the atomic coordination shells of Fe ions. Therefore, the following cases were considered: model 2 with V_O in the first coordinaton shell of two Fe ions, model 3 with V_O in different coordination shells of two (thus nonequivalent) Fe ions, and model 4 with V_O and Fe maximally separated from each other within a supercell. After the relaxation the oxygen atoms near each iron impurity are grouped into *planar* (four O_{pl} belonging to the same plane) and *axial* (remaining two or one O_{ax}, depending on V_O presence nearby Fe), according to Ref. [126].
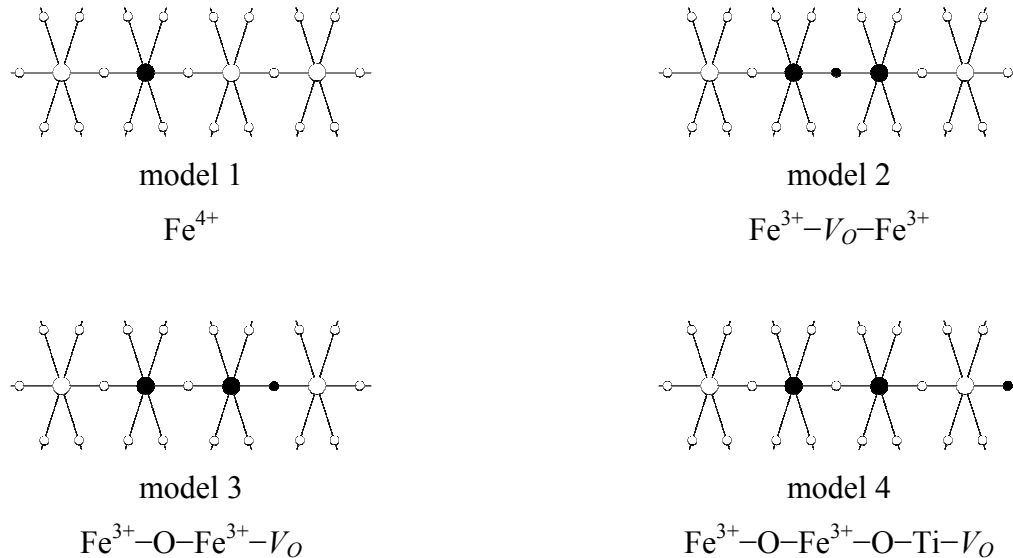

model 1

Fe^{4+}

model 2

$Fe^{3+}-V_O-Fe^{3+}$

model 3

$Fe^{3+}-O-Fe^{3+}-V_O$

model 4

$Fe^{3+}-O-Fe^{3+}-O-Ti-V_O$

FIG. 18. Schematic view of the four structural models (Ti — o, O — ○, Fe — ●, V_O — •).

X-ray absorption spectroscopy is a local structural tool perfectly suited for investigation of relaxation effects around impurity atoms in crystalline and disordered compounds [121]. However, the analysis of the XANES data is a complicated task due to the contribution of high-order multiple-scattering processes [122, 123], which reflect many-atom distribution functions or the 3D atomic structure. The XANES spectrum of a crystalline compound is usually calculated for a static equilibrium atomic structure, typically known from a diffraction experiment, while a configurational average is required to achieve good agreement between theoretical and experimental XANES signals [123].

In the case of impurity atoms, the relaxation of their local environment must be taken into account in the XANES calculations. Since the effect of relaxation is usually not known a priori and cannot be determined experimentally by other techniques with the required accuracy (about 0.01 Å or better), one needs to search for an alternative solution. The answer can be found in the combined use of *ab initio* quantum mechanical and XANES methods. Such an approach allows one to couple the results of two theoretical methods by computing XANES spectrum for the *ab initio* calculated ground-state atomic structure. The agreement between theoretical and experimental XANES spectra can be used as an estimate of the accuracy of the structure relaxation determined by the *ab initio* calculation.

In this study self-consistent, real-space full-multiple-scattering XANES calculations of the Fe K-edge in Fe-doped $SrTiO_3$ were performed by the FDMNES code [124, 125] for the four structural models shown in Fig. 18. The details on calculating XANES are beyond the subject of this thesis and can be found by Ref. [126].

The experimental Fe K-edge XANES spectrum for the cathodic region of the electrocolored Fe^{3+}-doped $SrTiO_3$ single crystal has been discussed in Ref. [112]. Four distinctive features (A, B, C, D) can be observed in the experimental XANES spectrum below the main absorption edge E (Fig. 19). In the dipole approximation, the $1s$ (Fe) core-electron is excited into unoccupied final-states with p-character. Such transitions are the origin of all the peaks above A. The transition of the $1s$ (Fe) electron to the conduction band of Fe-doped $SrTiO_3$ (peak A in Fig. 19) is forbidden in the dipole approximation, since the band is composed mainly of the $3d$-metal ion (Ti/Fe) states. However, such a transition can become allowed either (i) within the quadrupole approximation or (ii) due to the lowering of local symmetry, caused by the Jahn-Teller distortion [92, 93] or by the presence of the V_O in the first coordination shell of the iron atom.
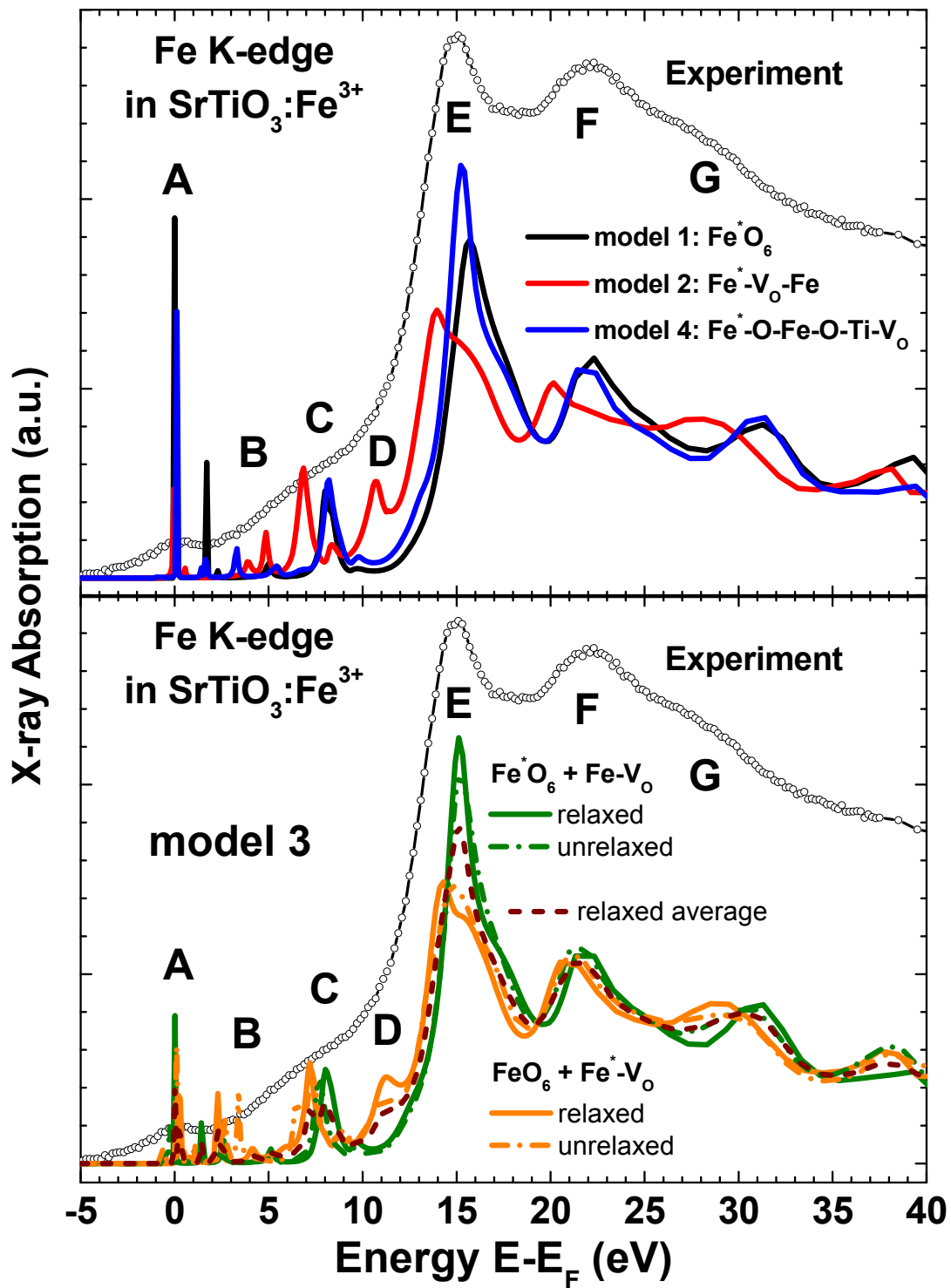
FIG. 19. Comparison of the experimental [112] and calculated (models 1 − 4) Fe K-edge XANES spectra [126]. For the model 3 the XANES spectra for the two relaxed (unrelaxed) Fe sites are shown by solid (dash-dotted) lines, and the average XANES spectrum for relaxed structure is shown by dashed line. The zero of energy scale corresponds to the theoretical Fermi level E_F.

TABLE 14. Comparison of the models by the total electronic energy and structural distortions, obtained from *ab initio* simulations (Ti–O distance in a pure $SrTiO_3$ is 1.96 Å)

Model	Cohesive energy resp. to undoped crystal, E_{coh}, eV	Defects formation energy, E_{form}, eV	Interatomic distances, Å			
				ab initio Fe–$O_{pl.}$ Fe–$O_{ax.}$	*ab initio* Fe–O averaged	EXAFS [112] Fe–O averaged
1. Fe^{4+}	−0.14	2.22	Fe_1	4 × 1.88 2 × 2.07	1.94	1.93
2. $Fe^{3+}-V_O-Fe^{3+}$	−0.57	9.13	$Fe_{1,2}$	4 × 1.98 1 × 1.85	1.95	1.96
3. $Fe^{3+}-O-Fe^{3+}-V_O$	−0.58	9.35	Fe_1	4 × 2.01 1 × 1.93, 1 × 2.00	2.00	1.97
			Fe_2	4 × 1.98 1 × 1.83	1.95	1.96
4. $Fe^{3+}-O-Fe^{3+}-$ $-O-Ti-V_O$	−0.59	9.50	$Fe_{1,2}$	4 × 2.01 1 × 1.90, 1 × 2.05	2.00	1.97
$LaFeO_3$	—	—		2 × 2.00 4 × 2.01	2.01	2.01[a]

[a]Neutron diffraction experiments [127] below 298°K

In the first model, four short Fe−O distances of about 1.88 Å and two long Fe−O distances of about 2.07 Å (Table 14) were obtained from *ab initio* calculations as a result of the Jahn-Teller distortion. Such a structural model is able to reproduce the main peaks observed in the experimental Fe K-edge XANES, but fails to predict the absorption in the region of the peaks D and G.

In the model 2, a single oxygen vacancy is placed between two iron atoms, so that they become five-fold coordinated. The mutual Coulomb repulsion causes the shifts of the two iron ions in opposite directions (by 0.14 Å each). The planar oxygen atoms move by 0.11 Å towards the V_O and by 0.02 Å away the iron ions: thus, four Fe−O distances becomes 1.98 Å, in good agreement with the EXAFS results [112] (Table 14). The peculiar aspect of this model is the appearance of the

peak D in the Fe K-edge XANES signal, the decrease of the peak E intensity, and a shift of all peak positions to smaller energies. This model also predicts a shift of the peak G at 31 eV down to ~28 eV, which explains the origin of the shoulder in the experimental data. To conclude, this model gives good overall agreement with the experimental XANES spectrum.

In the model 4, a single oxygen vacancy is placed in the third coordinaton shell of Fe^{3+} ions. In this case, two Ti atoms near V_O are repelled in opposite directions (by 0.18 Å each). Six oxygen atoms around the iron ions also relax considerably (Table 14). The average Fe−O distance (2.00 Å) is larger than for models 1 and 2, following the EXAFS results [112]. Note that in $LaFeO_3$ (which can be considered as a reference system for a Fe^{3+} state) we have obtained an average distance Fe–O as 2.01 Å (orthorhombic phase), exactly corresponding to the experimental value [127]. The Fe K-edge XANES signal for the model 4 has the least agreement with the experiment: the peak D is completely absent and the main peak E becomes more intense.

Lastly, the special feature of the model 3 is that the two Fe^{3+} ions occupy nonequivalent sites, which represent an intermediate situation between models 2 and 4. Therefore the total Fe K-edge XANES signal for the model 3 is computed as the average of those for the two iron sites. In Fig. 19 we show the XANES signals for both the five-fold and six-fold coordinated Fe in unrelaxed and relaxed environments as well as the average XANES signal for the relaxed structure. Note that the average XANES signal gives the *best* agreement with the experiment: the shoulder D is present, the peak G resides near 30 eV, and the shape of peak E agrees with the experimental one.

The model 3 shows also that the *ab initio* lattice relaxation produces a small effect on the shape of the XANES signal. The impact of relaxation is similar for other models. A comparison of the averaged atomic distortions around each of the two nonequivalent Fe^{3+} ions (Table 14) shows a less pronounced relaxation near V_O and a more pronounced away from V_O. This difference agrees with the EXAFS results [112] and is mainly due to planar oxygen atoms.

Note that the presence of V_O in the nearest shell of Fe^{3+} determines the relaxation pattern. In all the models 2 − 4, the Fe ion near V_O moves outward by ~0.10 Å, while the Fe ion far from V_O experiences practically no displacement (this can be seen in the change of the distance Fe–O_{ax}). The redistribution of the electron density from V_O to the nearest d-metal cations leads to the competition of Coulomb attraction and repulsion effects, resulting in the residual repulsion between iron impurities and planar O atoms. This long-range effect is traced in the EXAFS experiment.

A comparison of the defect formation energies for the models 2 and 4 allows us to estimate the binding energy between Fe^{3+} and V_O in the first coordination shell to be ~0.4 eV (in good

agreement with the experimental estimate of 0.3 eV [109] and the results of atomistic simulations [128]), *i.e.* the $Fe^{3+}-V_O$ pairs are stable at around room temperature.
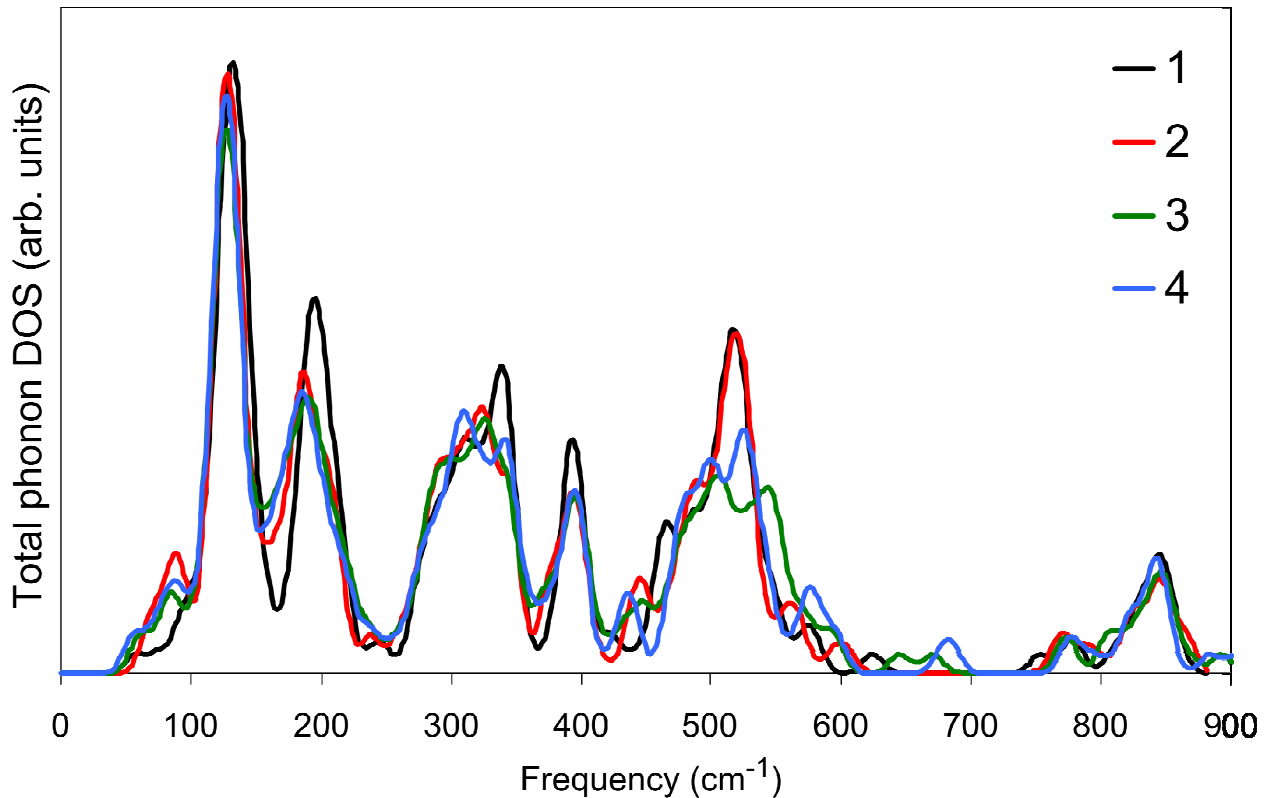

FIG. 20. The calculated total phonon DOS for the models 1−4. The phonon frequencies were smeared according to a normal distribution. Note the range 620–760 cm^{-1} [126].

The phonon DOS for a perfect $SrTiO_3$ as well as for single Fe^{4+} and V_O point defects have been reported in Chapter 3 and 4.2−4.3. Our calculations have shown there that both the defects are responsible for the new phonon modes in the range 620–760 cm^{-1}. Fig. 20 shows the phonon DOS for considered models. One can see that formation of the $Fe^{3+}-V_O$ complex (model 2) leads to the disappearance of the phonon modes in the range of 620–760 cm^{-1} while for all other models this range is non-empty. This agrees with the recent Raman and IR spectroscopy results [94, 112], where no significant phonon intensity was observed in this range for the Fe^{3+}-case, in contrast to the Fe^{4+}-case. Note however that the calculated DOS represents a semiquantitative picture, since only the BZ-centered frequencies can be used [126].

4.5. Conclusions

(1) The defective $Sr(Fe_xTi_{1-x})O_3$ system was considered at *ab initio* level for several iron impurity concentrations. The existence of the Jahn-Teller distortion around the Fe^{4+} impurity, as well as the increase of the surrounding O atom displacements as iron concentration decreases, was confirmed.

(2) In the reduced $SrTiO_3$, the oxygen vacancy with two electrons leads to the energetically preferable triplet spin state and Jahn-Teller local distortion of the lattice. In particular, we have shown that use of ghost BS at the vacancy site leads to nearly singly ionized oxygen vacancy $V_o^{\bullet}$. The corresponding formation energy at $0°K$ (6.26 eV) is well converged with the respect to the supercell size and consistent with the experiments. A neglect of the ghost BS functions and use of smaller (*e.g.* 40-atom) supercells lead to errors in V_O formation energy of up to 1 eV.

(3) The Jahn-Teller-type lattice distortion around two quite different types of defects – Fe^{4+} and V_O – is shown to result in appearance of Raman- and IR-active phonon frequencies. The defect-induced vibrational modes were deduced from a group-theoretical analysis of the results of the *ab initio* calculations, and used for the interpretation of available experimental data. Such an analysis is of primary importance, because (i) the defect-induced Raman frequencies do not necessarily coincide with those in the phonon spectrum of a perfect crystal, (ii) the defect-induced frequencies do not always involve the motion of the impurity, and (iii) depending on the selection rules, the new local Ti−O and Fe−O vibrational modes (which are absent in the perfect crystal) could be IR- or Raman-active.

(4) The assignment of the experimental IR and Raman frequencies was suggested for oxygen vacancy and iron impurity defects. The Raman frequencies experimentally observed around 700 cm^{-1} for both defects arise due to a *local* O ion stretching vibration nearby Jahn-Teller defect.

(5) The V_O Gibbs formation energy calculated for 6.25% oxygen vacancies taking into account the phonon contribution is in good agreement with experiment and drops considerably (by ~0.8 eV) as temperature increases from 300 to $1000°K$. The phonon contribution to the V_O formation energy increases with temperature, being ~5% above 1000 K.

73

(6) We performed *ab initio* hybrid DFT-LCAO calculations of the lattice relaxation for different $Fe^{3+}-V_O$ complexes in Fe^{3+}-doped $SrTiO_3$ and used them to simulate the Fe K-edge XANES spectra, which are compared to the experimental data for the cathodic region of electrocolored samples. The obtained results suggest that the presence of the oxygen vacancy in the *first* coordination shell of iron is crucial for the qualitative interpretation of the experimental XANES signal, while the *ab initio* lattice relaxation effects are less important. On the other hand, the lattice relaxations obtained for different complexes are in good agreement with the EXAFS experiments.

(7) The $Fe^{3+}-V_O$ complex has a binding energy of ~0.4 eV, in reasonable agreement with the experimental estimate. Its formation is manifested in the calculated phonon spectra by the disappearance of the phonon frequencies near 700 cm^{-1} (typical for isolated Fe^{4+} and V_O defects), in agreement with the recent Raman and IR spectroscopy results.

5. Perfect and defective SrTiO₃ surface

5.1. Literature overview

This Chapter conveys the experience accumulated for three-dimensional systems to one-dimension confined case, comprising information on the $SrTiO_3$ surfaces (slabs), which are either defect-free or contain oxygen vacancies.

Recent experimental studies exploiting the atomic and friction force microscopy approaches have made a considerable progress in surface characterization, being able to identify not only the two different terminations of the (001) $SrTiO_3$ surface (SrO and TiO_2), but also various adspecies [130−132]. Evidently, the properties of surfaces considerably differ from the bulk. The very high static dielectric constant of the bulk crystal decreases significantly in thin films (from several thousands to several hundreds [2, 133]). This correlates with a soft phonon mode hardening near the topmost layer [2]. Moreover, $SrTiO_3$ thin films with different concentrations of oxygen vacancies demonstrate a considerable fall of the dielectric constant, by a factor of 2, *i.e.* from 1000 to 450 at 77°K [134].

Recent *ab initio* calculations on $SrTiO_3$ surfaces complemented these experimental insights concerning the atomic and electronic structure, chemical bonding and covalency effects for defect-free surfaces [135−138]. Namely, it has been shown, that the (001) surfaces are energetically preferable over the polar (011) surfaces [138], whereas the TiO_2-terminated (001) surface is very close in formation energy to the SrO-terminated one [137]. A considerable increase of the Ti–O chemical bond covalency near surfaces is also revealed [137] and obviously should affect the properties of surface defects, as well as adsorption phenomena.

The oxygen vacancies on $SrTiO_3$ surfaces have a considerable influence on the transport, optical and ferroelectric properties of the host material [139]. They play an important role in mixed ionic-electronic conductivity in thin solid films, which is a principal interest of this thesis. Furthermore they are implied to be decisive for the processes of surface reconstruction [140, 141]. Based on ultraviolet photoelectron spectroscopy experiments, it was suggested, that the formation of oxygen vacancies may result in a shallow occupied defect level below the conduction band edge and thus increase the electronic conductivity [142, 143].

Several attempts of computational study of surface properties with oxygen vacancies were made [144−146]. However, in Refs. [144, 145] an important surface relaxation was not taken into account, and in Ref. [146] the usage of expanded surface cells was omitted. It was possible though to

adjudge the larger surface rumples and smaller interlayer distances at the fully relaxed SrTiO₃ (001) oxygen-vacancy surfaces, in contrast to the perfect surfaces [146].

Lastly, in the recent study of our group [147] the oxygen vacancies were examined *ab initio* in the (001) ultrathin films (one-dimensional confinement effect). The vacancy formation energy in the films of perovskite materials of 2–3 nm thickness was shown to be largely invariant and deviate from the bulk value only for the thinnest 3-plane surface.
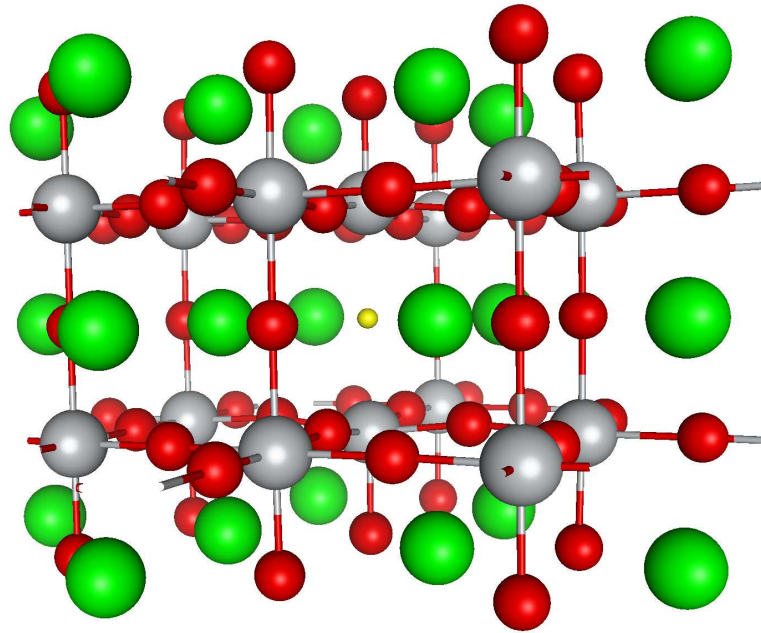

FIG. 21. An example of (001) SrTiO₃ ultrathin film (SrO termination, 5 planes, oxygen vacancy in the central plane). Atomic radii are not taken into account.

In this Chapter the results of the calculations on the vacancy formation energy in ultrathin films (Fig. 21) are presented, and comparison for 0 K level and finite temperatures is made.

5.2. Results

We applied the above-developed computational scheme (Chapters 2−3) to the defect-free (001) ultrathin films of SrTiO$_3$ consisting of odd number of 3−13 crystalline planes (a slab model [21]). An oddity of plane number provides an inversion center retained and therefore a decrease of computational costs. Since the topmost layers are the same, another advantage is the absence of an unphysical polarity. Note, that the stoichiometry is not complied at such the conditions. A similar approach was applied in the majority of perovskite surface computational studies [135, 137−139, 147]. Our emphasis is placed onto the thermodynamic functions at relatively high temperatures (typical for applications). There are two possible slab terminations, SrO- and TiO$_2$-type, which considerably differ in the vibrational properties.

The two soft modes are known in the cubic bulk SrTiO$_3$: AFD (*R*-point) and FE (*Γ*-point), see Chapter 3. Projecting three-dimensional BZ onto two-dimensional space, one can see the same soft modes correspond to the *Γ* and *M* points of two-dimensional BZ zone of the surface (layer group *P4/mmm*), as depicted in Fig. 22. Indeed, our calculations confirm, that there are soft modes exactly in these symmetry points for both terminations. However, they are found to be imaginary for TiO$_2$ termination and real for SrO termination.
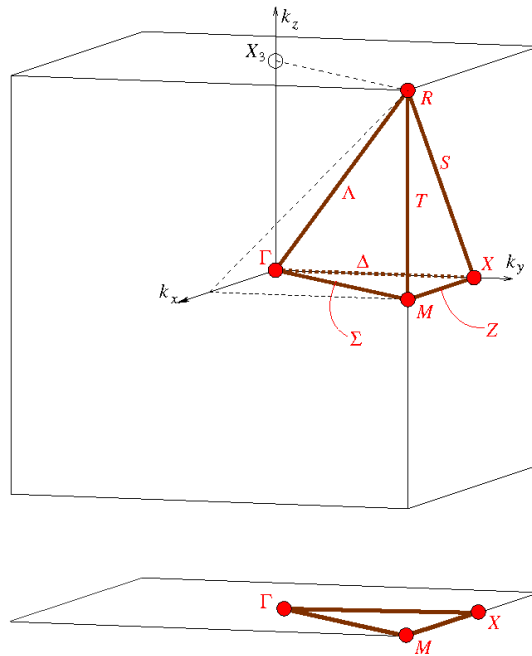

FIG. 22. The BZ for the bulk lattice of cubic SrTiO$_3$ (top) and for two-dimensional lattice of SrTiO$_3$ surface (bottom) [72]

TABLE 15. Surface phase transition at TiO_2-terminated surfaces

Object	TiO_6 rotation angle, °	ΔE (meV) due to phase transition	Resulting symmetry
3-plane surface	—	−48.1	oblique (2D)
5-plane surface	0.8	−7.2	oblique (2D)
7-plane surface	0.5	−2.0	oblique (2D)
Bulk AFD $SrTiO_3$	0.9	−2.9	tetragonal (3D)

Due to this fact, we considered two terminations separately henceforth. A proper estimate of thermodynamic functions was impossible for TiO_2-terminated surfaces, due to the imaginary values of the soft mode frequencies (see Chapter 2.4). We followed therefore the structural deformations driven by the imaginary soft modes in 3-, 5- and 7-plane slabs, which brought us to the oblique-symmetry surfaces, with no imaginary soft modes and the total energy preference over the high-symmetric phase (Table 15, Fig. 23). That is, a surface phase transition (*i.e.* reconstruction including octahedral rotation, similar to the bulk phase transition at 105 K) was observed. Analogously to the bulk case, the imaginary soft modes in the corner of the BZ of two-dimensional lattice correspond to the anti-phase TiO_6 octahedral rotations, in the center of the BZ — to the displacive FE movements of oxygen atoms (in parallel to the plane of slab).
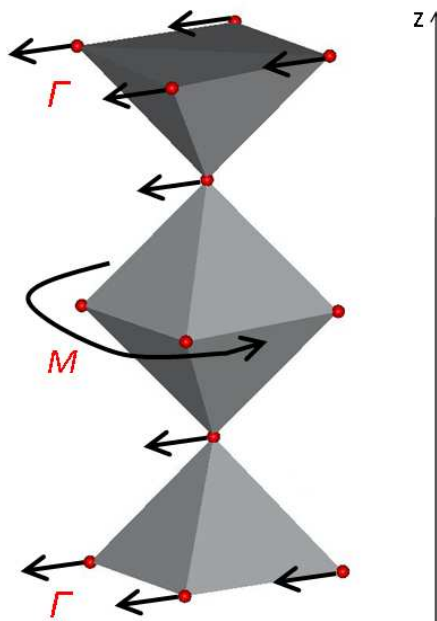

FIG. 23. Surface phase transition at the TiO_2-terminated $SrTiO_3$ 5-plane surface (the respective *Γ*- and *M*-point soft modes at the high-symmetry phase are shown)

Note the saturation of the low-symmetry phase energetic preference with the increase of the number of planes, in comparison with the bulk case. A similar phenomenon can be observed in Fig. 24 for vacancy formation energy in SrO-terminated thin films. Nevertheless, a very low symmetry of the resulted TiO$_2$-terminated slabs prevented us from dealing with the vacancy defect therein so far.

No symmetry-reducing reconstruction occurs for SrO termination, where the atomic relaxation within a high-symmetry tetragonal *P4/mmm* layer group results in real values of the soft modes (slightly less than 100 cm^{-1}). This might be also an artifact; however, checking this hypothesis would require very time-consuming calculations and was therefore omitted.

Spin-polarized calculations were performed for the neutral oxygen vacancy V_O introduced with the ghost BS in the central plane of the highly symmetrical SrO-terminated surfaces (Fig. 21). For example, the FM solution for the 5-plane surface was found to be energetically more preferable by 0.41 eV than the AFM one, and by 0.45 eV than the NM one (the order of solutions and their energetic difference correspond to that for bulk case, see Chapter 4.3), the similar situation was obtained for 3-plane surface. Hence, all other calculations were performed for the FM state.
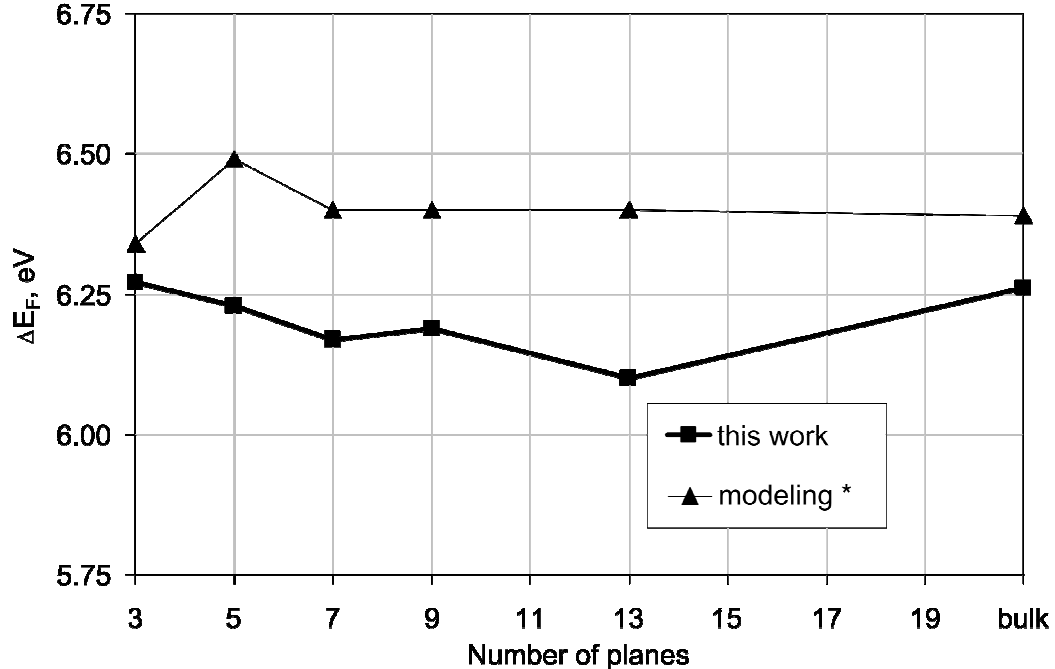

FIG. 24. The calculated oxygen vacancy formation energies in the central plane of SrO-terminated SrTiO$_3$ surfaces at 0 K (those marked by an asterisk are taken from Ref. [147])

In Fig. 24 our results for V_O formation energy are compared with a previous study of our group [147], both at 0 K. The main differences lie in Hamiltonian (B3PW in [147] vs. PBE0 here), PP / BS choice (PPP in [147] vs. SPP here), and spin-polarized state (NM in [147] vs. FM here). The results moderately agree, and the main conclusion remains: no principal difference with the bulk case is observed for SrO-terminated SrTiO$_3$ surfaces, *i.e.* the confinement effect (counter-intuitively) is not revealed for this type of surface termination.

We then take into account the vibrational contribution (Eq. 9, Fig. 25). As compared to three-dimensional bulk case (Chapter 4.3), the phonon contributions to the Gibbs free energy of V_O formation at the high temperatures are at least twice smaller for all three cases of film thickness under consideration (3-, 5-, 7-plane). Thus, at 1000 K the phonon contribution to the Gibbs free energy for the bulk case is 50 meV, whereas for 3-plane surface it is only 12 meV. For 5- and 7-plane slabs it slightly increases towards the bulk case (24 and 17 meV, correspondingly), but still being far from saturation. It this sense, the confinement effect of phonon contribution is long-ranged, saturating slowly with the surface thickness. However, the magnitude of the phonon contribution is very minor, at least 5 times smaller than the difference due to the surface thickness (Fig. 24). This prevents of concluding that the phonon contribution has any significant influence on the Gibbs free energy of V_O formation on SrTiO$_3$ surface. Hence, this case is similar to the bulk case (Chapter 4.3).
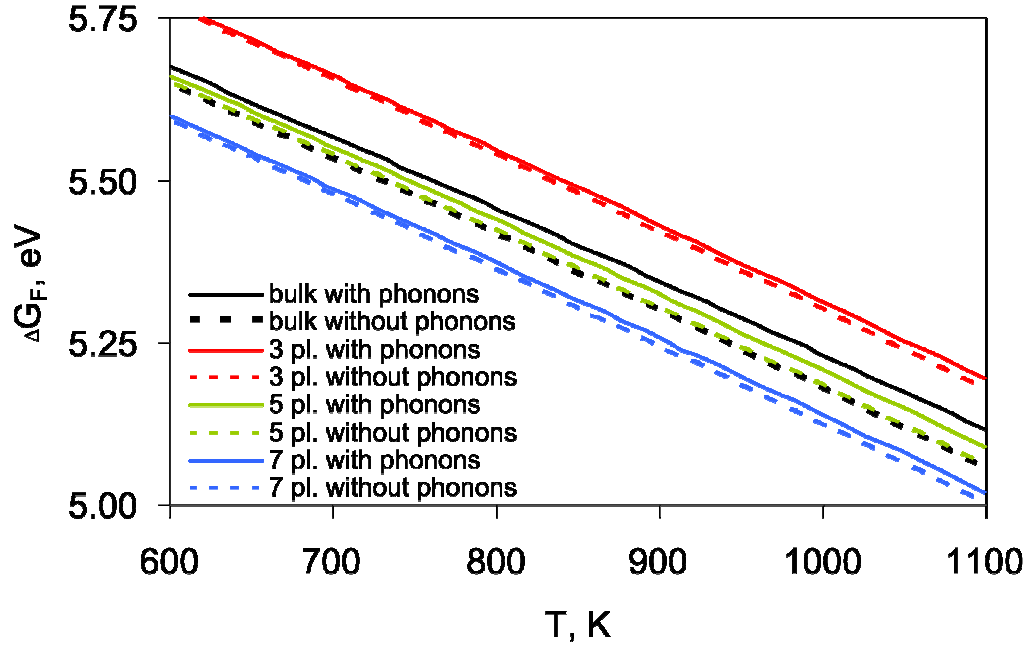

FIG. 25. The calculated oxygen vacancy formation energies in the central plane of SrO-terminated SrTiO$_3$ surfaces as a function of temperature

Note that such a result is obtained using the pre-factors in Eq. 9 which represent the phonon contribution scaling to the primitive unit cell of bulk cubic $SrTiO_3$ crystal (Chapter 2.4). This scaling mainly represents an attempt to suppress anharmonic errors caused by the soft mode impact. Apparently, an extended accounting of anharmonic effects is required, which, however, for defective surfaces is concerned with extremely high computational costs.

A shortcoming of the supercell approach is the necessity to use large supercells to model reasonable defect concentrations. This is essentially valid for surfaces, where the need to represent the distinct defect concentration interferes with a retaining a certain slab thickness. One has to make sure that the defect properties expose no finite-size effects (*i.e.* are saturated). In addition, saturation of the electron properties (*e.g.* low defect level dispersion over the BZ, see Chapter 4.3) does not necessarily guarantee the saturation of phonon properties (*e.g.* vibrational enthalpy convergence) for a given supercell size. Apparently, this is the case for $SrTiO_3$ bulk with 6.25% V_O and SrO-terminated surfaces with the V_O in the central plane. Additionally, the slow phonon properties saturation (~20 meV for surface case vs. 50 meV for bulk case) is unlikely to be caused by a high value of the dielectric constant (which is probably the case for bulk crystal), since it is greatly decreased under one-dimensional confinement (Chapter 5.1).

In this Chapter we made an attempt to shed more light on the finite-temperature aspects of defect formation in ultrathin films of $SrTiO_3$. However, several issues still require an additional investigation: *e.g.* direct comparison of two different terminations (SrO and TiO_2), surface supercell finite-size effects and anharmonicity account. Unfortunately, each of the above-mentioned ones needs extremely time- and resource-consuming computations, revealing the restrictions of the used FP method and, in general, high demand of efficient reciprocal space integration to the high symmetry constrains.

5.3. Conclusions

(1) For the first time the phonon spectra are calculated for the completely relaxed defect-free and defective (001) surfaces of SrTiO$_3$, using a robust hybrid HF-DFT LCAO computational scheme. The defect under consideration was a neutral oxygen vacancy in the central plane of ultrathin SrTiO$_3$ film. The phonon calculations enabled us to estimate, how the finite-temperature defect formation energy changes with the surface thickness comparing to the bulk case (the effect of one-dimensional confinement).

(2) The analysis of calculated phonon spectra for TiO$_2$-terminated defect-free SrTiO$_3$ surfaces reveals large reconstruction effects. A number of imaginary soft modes is observed (in Γ and M points of two-dimensional lattice BZ), being in agreement with group-theoretical analysis, done earlier for three-dimensional case and adopted now for two dimensions. The surface symmetry therefore decreases considerably until triclinic or monoclinic layer groups via the soft-mode driven mechanism, *i.e.* a surface phase transition is predicted for TiO$_2$ termination. Contrary, SrO-terminated SrTiO$_3$ surfaces do not demonstrate any imaginary soft modes in their phonon spectra and remain less-distorted, owing the tetragonal layer group.

(3) Using SrO-terminated SrTiO$_3$ ultrathin films the known insignificance of the confinement effect on oxygen vacancy formation energy at 0 K was reproduced. That is, no considerable change in the formation energy is detected comparing to the bulk case. The phonon contribution to the Gibbs free energy of V_O formation is found to be very minor (~1% at 1000 K). It saturates slowly with the surface thickness though, being two times smaller than for the bulk case even for the thickest considered 7-plane slab. In this connection, an extended accounting of anharmonic effects is required, which, however, for defective surfaces is concerned with extremely high computational costs.

6. Summary

This thesis was focused on *ab initio* calculations of phonon properties of both perfect and defective $SrTiO_3$ perovskite crystal, bulk crystals and surfaces. Phonon properties of $SrTiO_3$ perovskite provide a link to the finite-temperature phenomena, occurring in complex materials, used as cathode materials of solid oxide fuel cells.

Initially, the robust *ab initio* computational scheme was established. Such a scheme was capable to yield the vibrational properties of bulk defect-free $SrTiO_3$ in a qualitative agreement with experimental measurements available. The group-theoretical analysis of the phonon symmetry indicated that in the defect-free $SrTiO_3$ the known antiferrodistortive phase transition is caused by a softening of the R_4^+ phonon mode, which is in agreement with our calculations. Detailed calculations of phonon frequencies in the tetragonal phase have been performed. The splitting of the phonon frequencies due to the phase transition was predicted to be rather small, of order of several cm^{-1}. Experimentally known low temperature Γ- and R-phonon instabilities in the cubic $SrTiO_3$ were reproduced. A comparison of the heat capacity and free energy temperature dependence was performed *ab initio* for the first time for cubic and tetragonal $SrTiO_3$ phases.

The defective $Sr(Fe_xTi_{1-x})O_3$ system was considered at *ab initio* level for several iron impurity concentrations. The presence of the Jahn-Teller distortion around the iron impurity was confirmed. The oxygen vacancy introduction in perfect $SrTiO_3$ similarly led to Jahn-Teller local distortion of the lattice. Such lattice distortion around iron impurity and oxygen vacancy was shown to result in appearance of Raman- and IR-active phonon frequencies. The defect-induced vibrational modes were deduced from a group-theoretical analysis of the results of the *ab initio* calculations, and used for the interpretation of available experimental data. The assignment of the experimental IR and Raman frequencies was suggested for oxygen vacancy and iron impurity defects. The Raman frequencies experimentally observed around 700 cm^{-1} for both defects were shown to arise due to a *local* O ion stretching vibration nearby iron impurity or oxygen vacancy.

The calculated Gibbs formation energy of oxygen vacancies taking into account the phonon contribution was found to be in a good agreement with experiment. The phonon contribution to the V_O formation energy was shown to increase with temperature, being ~5% above 1000 K.

Ab initio lattice relaxation was performed for different complexes of iron impurities and oxygen vacancies in $SrTiO_3$. The obtained structures were used to simulate the Fe K-edge XANES spectra, which were then compared to the experimental data for the cathodic region of electrocolored samples. The results suggested that the presence of the oxygen vacancy in the first coordination shell

of iron impurity is crucial for the qualitative interpretation of the experimental XANES signal, while the *ab initio* lattice relaxation effects are less important. Nevertheless, the lattice relaxations obtained for different complexes were in a good agreement with the data of EXAFS experiments. The complex of oxygen vacancy in the first coordination shell of iron impurity in $SrTiO_3$ was found to have a binding energy of ~0.4 eV, in reasonable agreement with the experimental estimate. In the calculated phonon spectra its formation was proved to manifest by the disappearance of the phonon frequencies near 700 cm^{-1} (typical for isolated defects), in agreement with the recent Raman and IR spectroscopy results.

The phonon spectra were calculated for the completely relaxed defect-free and defective (001) surfaces of $SrTiO_3$. The defect under consideration was a neutral oxygen vacancy in the central plane of ultrathin $SrTiO_3$ film. The phonon calculations enabled an estimation of the effect of one-dimensional confinement, *i.e.* how the finite-temperature defect formation energy changes with the surface thickness, comparing to the bulk case. The analysis of calculated phonon spectra for TiO_2-terminated defect-free $SrTiO_3$ surfaces revealed large reconstruction effects. A number of imaginary soft modes was observed in Γ and M points of the BZ of the surface, being in agreement with group-theoretical analysis, done for three-dimensional case and adopted for two dimensions. A surface reconstruction was predicted for TiO_2 termination. Contrary, SrO-terminated $SrTiO_3$ surfaces did not demonstrate any imaginary soft modes in their phonon spectra and remained less-distorted, than TiO_2-terminated surfaces.

The known insignificance of the confinement effect on oxygen vacancy formation energy at 0 K was reproduced on an example of SrO-terminated $SrTiO_3$ ultrathin films. That is, no considerable change in the formation energy was detected comparing to the bulk case. The phonon contribution to the Gibbs free energy of V_O formation in SrO-terminated $SrTiO_3$ surfaces was found to be very minor (~1% at 1000 K), being at least two times smaller than for the bulk case and saturating very slowly with the number of surface planes.

7. Appendix. Computational details

The BS optimization is confirmed to be of high importance for LCAO calculations. In general, it greatly improves the results, reducing the relative errors for calculated frequencies by a factor of 2–5 with respect to the experimental data. The obtained BS exponents are presented in Table A1.

TABLE A1. Optimization of Gaussian-type outer exponents (bohr^{-2})

Type	Non-optimized	Optimized
Sr (small core) $4s^24p^65s^2$		
6s	0.3344	0.3452
5p	0.7418	0.7296
6p	0.2801	0.2757
Ti (small core) $3s^24p^63d^24s^2$		
5s	0.5128	0.6149
5p	0.3982	0.3426
4d	0.8002	0.7399
5d	0.2620	0.2936
O (all electron) $1s^22s^22p^4$		
3sp	0.9057	0.8785
4sp	0.2556	0.2287
3d	1.2920	0.1480

TABLE A2. The properties of a free O_2 molecule calculated with the hybrid PBE0 and HSE0 exchange-correlation functionals and LCAO BS. Numbers in parentheses corrected for zero-point vibrations.

	PBE0	HSE [129]	Expt. [53]
Equilibrium distance, Å	1.20	1.19	1.21
Binding energy, eV	5.30 (5.19)	5.25 (5.14)	5.12
Rotational temperature, K	2.11	—	2.07
Vibrational temperature, K	2478.60	2475.70	2230

The free energy of a gas-phase O_2 molecule was calculated within an ideal gas model (Eq. 8, Table A2), and an excellent agreement with the experimental estimates is achieved.

The technical parameters of the crystalline simulations are compiled in Table A3. In general, one can see the number of techniques, each of which is required to be properly chosen and checked. Furthermore, it is important to keep track of the restrictions of the chosen scheme, as well as the ways of its extending, providing its applicability beyond the subject of this thesis. To simplify this task and to satisfy the needs of classification, data retrieval and processing, the utility computer tool called *Tilde* was programmed [148]. In the nutshell, the aims of this tool are extraction of the results from the output log files of different computer modeling codes, keeping track of simulation details, automated data classification, and various data manipulations (*e.g.* visualizations and format conversions). Using Tilde, as of spring 2013, the systemized data repository of all the simulations related to this thesis was automatically created. The additional Tilde documentation is provided on internet [148].

TABLE A3. Computational setup.

Property	Value
Code	CRYSTAL09
Basis set	LCAO
Pseudopotential	[74, 75]
Exchange-correlation functional	PBE0
Monkhorst-Pack k-mesh (cub. $SrTiO_3$)	isotropic 8x8x8
Tolerance on E_{tot} on SCF (geom. opt.)	10^{-8}
Tolerance on E_{tot} on SCF (phonons)	10^{-10}
Truncation criteria for biel. integrals	$10^{-8}, 10^{-8}, 10^{-8}, 10^{-8}, 10^{-16}$
DFT density and grid weight tolerances	$10^{-8}, 10^{-16}$
Pseudopotential tolerance	10^{-8}
Damping on Fock-KS matrix mixing	70–80%
Eigenvalue level shifting (perfect $SrTiO_3$)	1 a.u.
DFT integration grid	75 rad., 974 ang. points
Convergence accelerator	Anderson method [149]
Initial Hessian building on geom. opt.	Schlegel's model [150]
Gradient on root mean square (geom. opt.)	0.00015
Displacement on root mean square (geom. opt.)	0.0006
FP method displacement (perfect $SrTiO_3$)	0.003Å
FP method displacement ($SrTi_{1-x}Fe_xO_3$)	0.01Å
FP method displacement ($SrTiO_{3-\delta}$)	0.006Å
FP numerical derivative technique	difference quotient formula [19]
Gaussian exponents truncation	0.1 bohr^{-2}
Phonon DOS norm. dist. smearing width	10–15 cm^{-1}

8. Bibliography

1.   F.A. Kröger and H.J. Vink, Solid State Physics, vol.3, editors: F. Seitz, D. Turnbull, p. 307 (1956)

2.   A. A. Sirenko, C. Bernhard, A. Golnik, A. M. Clark, J. Hao, W. Si, X. X. Xi, *Nature* 404, 373 (2000)

3.   M. S. Wrighton, A. Ellis, P. Wolczanski, D. Morse, H. Abrahamson, D. Ginley, *J. Am. Chem. Soc.* 98, 2774 (1976)

4.   R. Waser and M. Aono, *Nature Materials* 6, 833 (2007)

5.   N.Q. Minh, *J Am. Ceram. Soc.* 76, 563 (1993)

6.   J. W. McPherson and H. C. Mogul, *J. Appl. Phys.* 84, 1513 (1998)

7.   P. E. Bloechl and J. H. Stathis, *Physical Review Letters* 83, 372 (1999)

8.   J. Robertson, *Reports on Progress in Physics* 69, 327 (2006)

9.   R. Merkle and J. Maier, Angewandte Chemie 47, 3874 (2008)

10.   S.J. Skinner, J.A. Kilner, *Mater. Today* 3, 30 (2003)

11.   H. Donnerberg, Atomic Simulation of Electrooptic and Magnetooptic Oxide Materials, Springer Tracts in Modern Physics, Vol. 151, Springer-Verlag, New York (1999)

12.   T. Menke, R. Dittmann, P. Meuffels, K. Szot, and R. Waser, *J. Appl. Phys.* 106, 114507 (2009)

13.   S. Paek, E. Lee, S. Kim, J. Seong, J. Mah, C. Park, J. Choi, J. Jung, *Journal of Materials Science* 33, 1239 (1998)

14.   D. Kotecki, J. Baniecki, H. Shen, R. Laibowitz, K. Saenger, J. Lian, T. Shaw, S. Athavale, C. Cabral, P. Duncombe, M. Gutsche, G. Kunkel, Y. Park, Y. Wang, R. Wise, *IBM J. Res. Dev.* 43, 367 (1999)

15.   F. El-Mellouhi, N. Mousseau, *J. Appl. Phys.* 100, 083521 (2006)

16.   P. G. Sundell, M. E. Björketun, and G. Wahnström, *Phys.Rev. B* 73, 104112 (2006)

17.   S. Curtarolo, G.L.W. Hart, M.B. Nardelli, N.S. Sanvito and O. Levy, *Nature Mat.* 12, 191 (2013)

18.   I.E. Castelli, T. Olsen, S. Datta, D. Landis, S. Dahl, K.S. Thygesena and K.W. Jacobsen, *Energy Environ. Sci.*, 5, 5814 (2012)

19.   R. Dovesi, V. R. Saunders, C. Roetti, R. Orlando, C. M. Zicovich-Wilson, F. Pascale, B. Civalleri, K. Doll, N. M. Harrison, I. J. Bush, Ph. D'Arco, M. Llunell, CRYSTAL User's Manual, University of Turin (2009)

20. G. Kresse, J. Hafner, VASP the Guide, University of Vienna (2007), http://vasp.at;
G. Kresse, J. Furthmüller, *Comp. Mater. Sci.* 6, 15 (1996); G. Kresse and J. Hafner, *Phys. Rev. B* 47, RC558 (1993); G. Kresse and J. Furthmüller, *Phys. Rev. B* 54, 11 169 (1996)

21. R.A. Evarestov: Quantum Chemistry of Solids. The LCAO First Principles Treatment of Crystals. Springer Series in Solid State Sciences, Vol. 153. Heidelberg, Springer (2007)

22. C.C.J. Roothaan, *Rev. Mod. Phys.* 23, 69 (1951)

23. F. Bloch, *Z. Physik* 52, 555 (1928)

24. S.F. Boys, *Proc. R. Soc. London Ser. A* 200, 542 (1950)

25. H.J. Monkhorst, J.D. Pack, *Phys. Rev. B.* 13, 5188 (1976)

26. R. M. Martin, Electronic Structure: Basic Theory and Practical Methods, Cambridge University Press (2004)

27. M. Towler, An introductory guide to Gaussian basis sets in solid state electronic structure calculations, European Summer School "Ab initio modelling in solid-state chemistry", Turin (2000)

28. S. Piskunov, E. Heifets, R.I. Eglitis and G. Borstel, *Comp. Mater. Sci.* 29 165 (2004)

29. R. A. Evarestov, A. I. Panin, A. V. Bandura, M. V. Losev, *J. Phys.: Conf. Ser.* 117, 012015 (2008)

30. P.J. Hay, W.R. Wadt, *J. Chem. Phys.* 82, 270 (1984); P.J. Hay, W.R. Wadt, *J. Chem. Phys.* 82, 284 (1984); P.J. Hay, W.R. Wadt, *J. Chem. Phys.* 82, 299 (1984)

31. D. Andrae, U. Haussermann, M. Dolg, H. Stoll, and H. Preuss, *Theoretica Chimica Acta* 77, 123 (1990)

32. P. Dirac, *Proc. Cambridge Phil. Roy. Soc.* 26, 376 (1930)

33. J. P. Perdew, A. Ruzsinszky, J. Tao, V. N. Staroverov, G. E. Scuseria, G. I. Csonka, *J. Chem. Phys.* 123, 062201 (2005)

34. W. Kohn and L. J. Sham, *Physical Review* 140, 1133 (1965)

35. K. Burke, *J. Chem. Phys.* 136, 150901 (2012); C. J. Cramer, D. G. Truhlar, *Phys. Chem. Chem. Phys.* 11, 10757 (2009)

36. P. J. Stephens, F. J. Devlin, C. F. Chabalowski, and M. J. Frisch, *J. Phys. Chem.* 98, 11623 (1994)

37. A. D. Becke, *J. Chem. Phys.* 98, 5648 (1993)

38. J. P. Perdew, M. Ernzerhof, K. Burke, *J. Chem. Phys.* 105, 9982 (1996)

39. P. E. Bloechl, *Phys. Rev. B* 50, 17953 (1994)

40. D. Vanderbilt, *Phys. Rev. B* 41, 7892 (1990)

41. J. Paier, R. Hirschl, M.Marsman, and G. Kresse, *J. Chem. Phys.* 122, 234102 (2005)

42. M. Alaei, H. Akbarzadeh, H. Gholizadeh, S. de Gironcoli, *Phys. Rev. B* 77, 085414 (2008)

43. R.A. Evarestov, A.V. Bandura, V.E. Alexandrov, and E. A. Kotomin, *Phys. Stat. Sol. (b)* 242, 2, R11 (2005)

44. H. Kroemer, C. Kittel, Thermal Physics, 2nd Ed., W.H.Freeman and Company (1980); A. van de Walle, M. Asta, and G. Ceder, *Calphad* 26, 539 (2002)

45. S. Baroni, P. Giannozzi, A. Testa, *Phys. Rev. Lett.* 58, 1861 (1987)

46. K. Parlinski, Z. Li, Y. Kawazoe, *Phys. Rev. Lett.* 78, 4063 (1997)

47. F. Pascale, C.M. Zicovich-Wilson, F. Lopez Gejo, B. Civalleri, R. Orlando, R. Dovesi, *J. Comp. Chem.* 25, 888 (2004)

48. R.A. Evarestov, M.V. Losev, *J. Comp. Chem.* 30, 2645 (2009)

49. A. Togo, F. Oba, I. Tanaka, *Phys. Rev. B* 78: 134106 (2008)

50. O. Anderson, Equations of state of solids for geophysics and ceramic science, Oxford Press, New York (1995)

51. A.A. Maradudin, Theory of lattice dynamics in the harmonic approximation, Academic, New York (1971)

52. G. Grimvall, Thermophysical Properties of Materials, Elsevier, New York (1999)

53. B. Bokstein, M. I. Mendelev, D. J. Srolovitz, Thermodynamics and Kinetics in Materials Science: A short Course, Oxford Univ. Press, New York (2005)

54. Y.-L. Lee, J. Kleis, J. Rossmeisl, D. Morgan, *Phys. Rev. B* 80, 224101 (2009)

55. B. Dorado, M. Freyss, G. Martin, *Eur. Phys. J. B* 69, 203 (2009)

56. H. Unoki, T. Sakudo, *J. Phys. Soc. Japan* 23, 546 (1967)

57. J.F. Scott, *Rev. Mod. Phys.* 46, 83 (1974)

58. K.A. Müller, W. Berlinger, E. Tosatti, *Z. Phys. B. Cond. Matt.* 84, 277 (1991)

59. N. Sai, D. Vanderbilt, *Phys. Rev. B* 62, 13942 (2000)

60. A.K. Tagantsev, E.Courtens, L.Arzel, *Phys. Rev. B* 64, 224107 (2001)

61. V.V. Lemanov, *Ferroelectrics* 265, 1 (2002)

62. O.E. Kvyatkovskii, *Phys. Solid State* 43, 1345 (2001)

63. R. Wahl, D. Vogtenhuber, G. Kresse, *Phys. Rev. B*, 78, 104116 (2008)

64. C. Lasota, C. Wang, R. Yu, H. Krakauer, *Ferroelectrics* 194, 109 (1997)

65. A. Lebedev, *Physics of the Solid State* 51, 362 (2009)

66. T. Trautmann and C. Falter, *J. Phys.: Cond. Matt.* 16, 5955 (2004)

67. N. Choudhury, E. Walter, A. Kolesnikov, C. Loong. *Phys. Rev. B* 77, 134111 (2008)

68. Y. Xie, H. Yu, G. Zhang, H. Fu, *J. Phys.: Cond. Matt.* 20, 215215 (2008)

69. A. Boudali, M.D. Khodja, B. Amrani, D. Bourbie, K. Amara, A. Abada, *Phys. Lett. A* 373, 879 (2009)

70. E. Heifets, E.A. Kotomin, V. Trepakov, *J. Phys.: Cond. Matt.* 18, 4845 (2006)

71. R. A. Evarestov and V. P. Smirnov, Site Symmetry in Crystals: Theory and Applications, 2nd Ed. Springer Series in Solid State Sciences, Springer, Berlin-Heidelberg (2007)

72. Bilbao Crystallographic Web-Server http://cryst.ehu.es; M. I. Aroyo, J. M. Perez-Mato, D. Orobengoa, E. Tasci, G. de la Flor, A. Kirov, *Bulg. Chem. Commun.* 43, 183 (2011)

73. H. T. Stokes and D. M. Hatch, Isotropy Subgroups of the 230 Crystallographic Space Groups, Singapore: World Scientific (1988)

74. Basis Set Exchange Web-Server http://bse.pnl.gov; K. Schuchardt, B. Didier, T. Elsethagen, L. Sun, V. Gurumoorthi, J. Chase, J. Li, and T. Windus, *J. Chem. Inf. Model.* 47, 1045 (2007)

75. M. M. Hurley, L. F. Pacios, P. A. Christiansen, R. B. Ross, and W. C. Ermler, *J. Chem. Phys.* 84, 6840 (1986); L. A. LaJohn, P. A. Christiansen, R. B. Ross, T. Atashroo, and W. C. Ermler, *J. Chem. Phys.* 87, 2812 (1987)

76. J. Paier, M. Marsman, K. Hummer, G. Kresse, I.C. Gerber, and J.G. Angyan, *J. Chem. Phys.* 124, 154709 (2006)

77. L. Cao and E. Sozontov, and J. Zegenhagen, *Phys. Status Solidi A* 181, 387 (2000)

78. K. Van Benthem, C. Elsaesser, and R. H. French, *J. Appl. Phys.* 90, 6156 (2001)

79. D. Ricci, G. Bano, G. Pacchioni, and F. Illas, *Phys. Rev. B* 68, 224105 (2003)

80. Ferroelectrics and Related Substances, edited by K. H. Hellwege and A. M. Hellwege, Landolt-Bornstein, New Series, Group III, Vol. 3, Springer-Verlag, Berlin (1969)

81. M. E. Lines and A. M. Glass, Principles and Applications of Ferroelectrics and Related Materials, Clarendons, Oxford (1977)

82. J. L. Servoin, Y. Luspin, and F. Gervais, *Phys. Rev. B* 22, 5501 (1980)

83. W. G. Stirling, *J. Phys. C* 5, 2711 (1972)

84. P. A. Fleury, J. F. Scott, and J. M. Worlock, *Phys. Rev. Lett.* 21, 16 (1968)

85. W. Jauch and A. Palmer, *Phys. Rev. B* 60, 2961 (1999)

86. W. Lytle, *J. Appl. Phys.* 35, 2212 (1964)

87. C. J. Howard and H. T. Stokes, *Acta Crystallogr. A* 61, 93 (2005)

88. J. C. Galzerani and R. S. Katiyar, *Solid State Commun.* 41, 515 (1982)

89. M.T. Dove, Introduction to Lattice Dynamics, Cambridge University Press (1993)

90. G.J. Ackland and M.C.Warren, *Phase Transitions* 61, 215 (1997)

91. I. Hatta, Y. Shiroishi, K. A. Mueller, and W. Berlinger, *Phys. Rev. B* 16, 1138 (1977)

92. R.A. Evarestov, S. Piskunov, E.A. Kotomin and G. Borstel, *Phys. Rev. B* 67 064101 (2003)

93. V. Alexandrov, J. Maier and R.A. Evarestov, *Phys. Rev. B* 77 075111 (2008)

94. M. Vracar, A. Kuzmin, R. Merkle, J. Purans, E.A. Kotomin, J. Maier and O. Mathon, *Phys. Rev. B* 76 174107 (2007)

95. N. Minh and D. Phuong, *J. Exp. Nanosci.* 6, 226 (2011)

96. U. Wdowik and K. Parlinski, *J. Phys.: Condens. Matter* 21, 125601 (2009)

97. J. Sunarso, S. Baumann, J.M. Serra, W.A. Meulenberg, S. Liu, Y.S. Lin, J.C. Diniz da Costa, *J. Memb. Sci.* 320, 13 (2008)

98. A. Jannoti, C. G. Van de Walle, *Rep. Prog. Phys.* 72, 126501 (2009)

99. E. S. Jung, H. S. Kim, B. H. Kong, H. K. Cho, N. K. Park, H. S. Lee, *Phys. Stat. Soli. (b)* 244, 1553 (2007)

100. Yu. F. Zhukovskii, E. A. Kotomin, R. A. Evarestov, and D. E. Ellis, *Int. J. Quant. Chem.* 107, 2956 (2007)

101. D. Cuong, B. Lee, K. Choi, H. Ahn, S. Han, and J. Lee, *Phys. Rev. Lett.* 98, 115503 (2007)

102. Z. Hou and K. Terakura, *J. Phys. Soc. Japan* 79, 114704 (2010)

103. V.E. Alexandrov, E.A. Kotomin, J. Maier and R.A. Evarestov, *Eur. Phys. J. B* 72, 53 (2009)

104. M. Choi, F. Oba, and I. Tanaka, *Phys. Rev. B* 83, 214107 (2011)

105. Yu. Zhukovskii, E. A. Kotomin, and D. E. Ellis, *Solid State Commun.* 149, 1359 (2009)

106. E. Blokhin, D. Gryaznov, E. Kotomin, R. Evarestov, and J. Maier, *Int. Ferroelectrics* 123, 18 (2011)

107. R. A. Evarestov, E. Blokhin, D. Gryaznov, E. A. Kotomin, and J. Maier, *Phys Rev. B* 83 134108 (2011)

108. D. A. Tenne, I. E. Gonenli, A. Soukiassian, D. G. Schlom, S. M. Nakhmanson, K. M. Rabe, and X. Xi, *Phys. Rev. B* 76, 024303 (2007)

109. R. Merkle and J. Maier, *Phys Chem Chem Phys* 5, 2297 (2003)

110. K. Szot, W. Speier, G. Bihlmayer, and R.Waser, *Nature Mater.* 5, 312 (2006)

111. R. Waser, R.Dittmann, G. Staikov, and K. Szot, *Adv. Mater.* 21, 2632 (2009)

112. C. Lenser, A. Kalinko, A. Kuzmin, D. Berzins, J. Purans, K. Szot, R. Waser and R. Dittmann, *Phys. Chem. Chem. Phys.* 13, 20779 (2011)

113. C. Lenser, A. Kuzmin, J. Purans, A. Kalinko, R. Waser and R. Dittmann, *J. Appl. Phys.* 111, 076101 (2012)

114. K. A. Blazey, J. A. Cabrera, and K. A. Müller, *Solid State Commun.* 45, 903 (1983)

115. J. Dunitz J and L. Orgel, *J. Phys. Chem. Solids* 3, 20 (1957)

116. I. Bersuker, The Jahn–Teller Effect, Cambridge: Cambridge University Press (2006)

117. R. Moos and K. H. Haerdtl, *J. Am. Cer. Soc.* 80, 2549 (1997)

118. V. V. Laguta, M. D. Glinchuk, R. O. Kuzian, S. N. Nokhrin, I. P. Bykov, J. Rosa, L. Jastrabik, and M. G. Karkut, *J. Phys.: Cond. Matt.* 14, 13813 (2002)

119. E. Blokhin, E. A. Kotomin, and J. Maier, *J. Phys.: Cond. Matt.* 24, 104024 (2012)

120. R. A. Evarestov, E. Blokhin, D. Gryaznov, E. A. Kotomin, R. Merkle, J. Maier, *Phys. Rev. B* 85, 174303 (2012)

121. J. J. Rehr, R. C. Albers, *Rev. Mod. Phys.* 72, 621 (2000)

122. A. Bianconi, A. Di Cicco, N. V. Pavel, M. Benfatto, A. Marcelli, C. R. Natoli, P. Pianetta and J. Woicik, *Phys. Rev. B* 36, 6426 (1987)

123. O. M. Roscioni, P. D'Angelo, G. Chillemi, S. Della Longa, and M. Benfatto, *J. Synchrotron Rad.* 12, 75 (2005)

124. Y. Joly, *Phys. Rev. B* 63, 125120 (2001)

125. O. Bunau, Y. Joly, *J. Phys.: Cond. Matt.* 21, 345501 (2009)

126. E. Blokhin, E.A. Kotomin, A. Kuzmin, J. Purans, R.A. Evarestov and J. Maier, *Appl. Phys. Lett.* 102, 112913 (2013)

127. S.E. Dann, D.B. Currie, M.T. Weller, M.F. Thomas, A.D. Al-Rawwas, *J. Sol. St. Chem.* 109, 134 (1994)

128. M. T. Buscaglia, V. Buscaglia, M. Viviani, and P. Nanni, *J. Am. Cer. Soc.* 84, 376 (2001)

129. J. Heyd, PhD Thesis, Rice University (2004)

130. J. Fompeyrine, R. Berger, H. P. Lang, J. Perret, E. Mächler, Ch. Gerber, and J. Locquet, *Appl. Phys. Lett.* 72, 1697 (1998)

131. K. Iwahori, S. Watanabe, M. Kawai, K. Mizuno, K. Sasaki, and M. Yoshimoto, *J. Appl. Phys.* 88, 7099 (2000)

132. M. Paradinas, L. Garzón, F. Sánchez, R. Bachelet, D. B. Amabilino, J. Fontcuberta, and C. Ocal, *Phys. Chem. Chem. Phys.* 12, 4452 (2010)

133. H.-C. Li, W. Si, A. D. West, X. X. Xi, *Appl. Phys. Lett.* 73 (4), 464 (1998)

134. X. Z. Liu, Y. R. Li, *Appl. Phys. A* 83, 67 (2006)

135. E. Heifets, R.I. Eglitis, E.A. Kotomin, J. Maier, G. Borstel, *Phys. Rev. B* 64, 235417 (2001)

136. D.S. Deak, *Materials Science and Technology* 23, 127 (2007)

137. S. Piskunov, E.A. Kotomin, E. Heifets, J. Maier, R.I. Eglitis, G. Borstel, *Surf. Sci.* 575, 75 (2005)

138. E. Heifets, W.A. Goddard, E.A. Kotomin, R.I. Eglitis, G. Borstel, *Phys. Rev. B* 69, 035408 (2004)

139. R. I. Eglitis, N. E. Christensen, E. A. Kotomin, A. V. Postnikov, and G. Borstel, *Phys. Rev. B* 56, 8599 (2003)

140. M. R. Castell, *Surf. Sci.* 505, 1 (2002)

141. K. Szot, W. Speier, J. Herion, and C. Freiburg, *Applied Physics A: Materials Science & Processing* 64, 55 (1997)

142. R. Courths, B. Cord, and H. Saalfeld, *Solid State Commun.* 70, 1047 (1989)

143. V. E. Henrich, G. Dresselhaus, and H. J. Zeiger, *Phys. Rev. B* 17, 4908 (1978)

144. J. Carrasco, F. Illas, N. Lopez, E.A. Kotomin, Yu. Zhukovskii, R. A. Evarestov, Yu. Mastrikov, S. Piskunov, and J. Maier., *Phys. Rev. B* 73, 064106 (2006)

145. S. Kimura, J. Yamauchi, M. Tsukada, and S. Watanabe, *Phys. Rev. B* 51, 11049 (1995)

146. M. Cai, J. Liu, G. Yang, Y. Cao, X. Tan, X. Chen, Y. Wang, L. Wang, and W. Hu, *Journal of Chemical Physics* 124, 174701 (2006)

147. E. A. Kotomin, V. Alexandrov, D. Gryaznov, R. A. Evarestov, J. Maier, *Phys. Chem. Chem. Phys.* 13, 923 (2011)

148. Tilde: data manager in computational materials science, http://tilde.pro

149. D. G. Anderson, *J. Assoc. Comput. Mach.* 12, 547 (1964)

150. H.B. Schlegel, *Theoret. Chim. Acta* 66, 333 (1984); J.M. Wittbrodt and H.B. Schlegel, *J. Mol. Structure - Theochem* 398, 55 (1997)

List of publications of the thesis results

1. E. Blokhin, R. A. Evarestov, D. Gryaznov, E. A. Kotomin, J. Maier, Theoretical modeling of antiferrodistortive phase transition for $SrTiO_3$ ulthrathin film, *in preparation*, 2013

2. D. Gryaznov, E. Blokhin, A. Sorokin, E. A. Kotomin, R. A. Evarestov, A. Bussmann-Holder and J. Maier, A comparative *ab initio* thermodynamic study of oxygen vacancies in ZnO and $SrTiO_3$: Emphasis on phonon contribution, *J. Phys. Chem. C* 117, 13776 (2013) http://dx.doi.org/10.1021/jp400609e

3. E. Blokhin, E. Kotomin, A. Kuzmin, J. Purans, R. Evarestov, and J. Maier, Theoretical modeling of the complexes of iron impurity and oxygen vacancy in $SrTiO_3$, *Appl. Phys. Lett.* 102, 112913 (2013) http://dx.doi.org/10.1063/1.4796182

4. R. Evarestov, E. Blokhin, D. Gryaznov, E. Kotomin, R.Merkle, J. Maier, Jahn-Teller effect in the phonon properties of defective $SrTiO_3$ from first principles, *Phys. Rev. B* 85, 174303 (2012) http://dx.doi.org/10.1103/PhysRevB.85.174303

5. E. Blokhin, E. A. Kotomin, and J. Maier, First-principles phonon calculations of Fe^{4+} impurity in $SrTiO_3$, *J. Phys.: Cond. Matt.* 24, 104024 (2012) http://dx.doi.org/10.1088/0953-8984/24/10/104024

6. R. Evarestov, E. Blokhin, D. Gryaznov, E. Kotomin, J. Maier, Phonon calculations in cubic and tetragonal phases of $SrTiO_3$: A comparative LCAO and plane-wave study, *Phys. Rev. B* 83, 134108 (2011) http://dx.doi.org/10.1103/PhysRevB.83.134108

7. E. Blokhin, D. Gryaznov, E. Kotomin, R. Evarestov, and J. Maier, A comparative hybrid DFT study of phonons in several $SrTiO_3$ phases, *Int. Ferroelectrics* 123, 18 (2011) http://dx.doi.org/10.1080/10584587.2011.570591

Curriculum vitae

Personal:

Name and surname: Evgeny Blokhin

Birth date and place: 31/08/1985, St. Petersburg, Russia

Gender: male

Education:

09/2009 – 06/2013   Ph.D. in materials science (department of Prof. J. Maier),

Max-Planck Institute for Solid State Research, Stuttgart, Germany;

thesis "*Ab initio* thermodynamic study of defective strontium titanate"

09/2007 – 06/2009   M.Sc. in quantum chemistry (advisor Prof. R.A. Evarestov),

St. Petersburg State University, St. Petersburg, Russia;

thesis "*Ab initio* modeling of strontium zirconate and strontium hafnate perovskite surfaces"

Spoken languages: English (fluent),

German (intermediate),

French (basic),

Russian (native)